Methods for the Analysis of Thermomagnetic Phase Transitions of Magnetocaloric Materials

PhD Thesis

Programa de doctorado en Ciencia y Tecnología de Nuevos Materiales

Luis M. Moreno Ramírez

Supervisors:
Prof. Alejandro Conde Amiano
Prof. Victorino Franco García

Departamento de Física de la Materia Condensada
Universidad de Sevilla

A Carmen, Paqui y Miriam

Acknowledgements

A mis directores Alejandro y Victorino por todo el esfuerzo puesto en mi formación y su trato amable y paciente. Me siento afortunado de haber podido aprender de ellos.

Al grupo de Sólidos no Cristalinos por su ayuda durante estos años. A Javier por ofrecerse a discutir cualquier cuestión. A Clara, Pepa y Jhon por su trato siempre cariñoso. A Jia Yan por todos los buenos ratos en el laboratorio. Al grupo de estudiantes por el buen ambiente: Alejandro, Emanuel, Antonio, Pablo, Álvaro, José Antonio y Antonio. Quisiera extender el agradecimiento a Carlos, David y Miriam por todas las colaboraciones realizadas.

To all the Functional Materials group of the Technical University of Darmstadt for their kind hospitality and fruitful collaboration. To Prof. Gutfleisch for giving me the opportunity to be part of his group. To Dr. Skokov and Dr. Radulov for their scientific guidance. To Fernando for all the support and camaraderie. To Bernd, Leo, Ahmed, Lukas Sch., Lukas Pf. and Juan for all the good moments there.

A mi familia y amigos por su sacrificio, apoyo y cariño. A Carmen y Paqui, sin las cuales no habría llegado a este momento. A Miriam por apoyarme en todo momento.

Al Ministerio de Educación y Formación Profesional del Gobierno de España por financiar esta tesis y las respectivas estancias de investigación a través de las ayudas FPU.

Contents

Abstract

This thesis focuses on the analysis of the relation between thermomagnetic phase transitions and magnetocaloric response of materials. First, various experimental factors that can affect the measurements of the magnetocaloric effect and can potentially cause misleading interpretation or artifacts are studied with the aid of experimental data and numerical calculations. These are sample geometry, compositional inhomogeneities, low temperature limitation in heat capacity measurements and measurement protocols in direct techniques. After that, it is shown that the analysis of the magnetic field dependence of the magnetocaloric effect is useful for obtaining information of thermomagnetic phase transitions, such as Curie temperature, critical exponents (even in biphasic systems), order of the phase transition and critical composition for which first order phase transition becomes second order. These analyses were performed in well know materials such as Gd, $Gd_5Si_2Ge_2$, $La(Fe,Si)_{13}$, Ni-Mn-In Heusler alloys and Fe-, Co-, Ni-amorphous and nanocrystalline alloys. Next, various possible avenues to optimize the magnetocaloric behavior by tapping on the characteristics of first and second order phase transition type systems were investigated. For second order phase transition type, the coefficient of refrigerant performance was optimized as a function of the amount of the various phase fractions in Gd-GdZn composite, while an enhanced magnetic field responsiveness is achived in nanostructured Gd/Ti multilayers. For first order phase transition type, reduction of hysteresis and enhancement of first order character is achieved in Ni- and Cr-doped $La(Fe,Si)_{13}$ compounds, respectively.

Nomenclature

Acronyms

A-N	Arrott-Noakes
B-R	Bean-Rodbell
BSE	Backscattered electrons
EDX	Energy dispersive espectroscopy
EOS	Equation of state
FOPT	First order phase transition
GoF	Goodness of fit
HRTEM	High-resolution transmission electron microscopy
K-F	Kouvel-Fisher
MA	Mechanical alloying
MC	Magnetocaloric
rand	Random number
RQ	Rapid quenching
SOPT	Second order phase transition
XRD	X-ray difracction

Symbols

$\alpha,\ \beta,\ \gamma,\ \delta,\ \Delta$	Critical exponents
χ	Magnetic susceptibility
ΔH	H-field change
ΔH_{hyst}	Magnetic hysteresis of the thermomagnetic phase transition
$\Delta S_M,\ \Delta S_L$	Magnetic and lattice entropy changes
ΔS_T	Isothermal entropy change
Δs_T	Specific isothermal entropy change
Δs_T^{ap}	Approximated Δs_T determined using calorimetric data starting from T_{ini}
$\Delta s_T^{pk},\ \Delta s_T^{ap,pk}$	Peak value of Δs_T and Δs_T^{ap}
ΔT_{FWHM}	Full temperature width at a half maximum

ΔT_{hyst}	Thermal hysteresis of the thermomagnetic phase transition
ΔT_S	Adiabatic temperature change
ΔT_S^{ap}	Approximated ΔT_S determined using calorimetric data starting from T_{ini}
ΔT_S^{pk}, $\Delta T_S^{ap,pk}$	Peak value of ΔT_S and ΔT_S^{ap}
Δv	Relative volume change
ϵ	Relative error
Λ	Difference between MC magnitudes using discontinuous and continuous protocols
λ	Exchange constant
λ_w	X-ray beam wavelenght
$\mathcal{B}$	Brillouin function
μ_0	Magnetic permeability of vacuum
μ_B	Bohr magneton
Ω	Half range of Gaussian distribution
ω	Standard deviation of Gaussian distribution
$\overline{T_C}$	Mean value of the T_C distribution
Φ	Deviation of MC magnitudes determined using calorimetric data starting from T_{ini}
Ψ, η	B-R parameters
σ	Specific magnetization
θ	Half angle between incident and diffracted X-ray beams
Θ_D	Debye temperature
ξ	Difference between s and s^{ap}
a, b	A-N EOS parameters
C	Heat capacity
c	Specific heat capacity
C_M, C_L, C_E	Magnetic, lattice and electronic heat capacities
CRP_{min}	Minimal coefficient of refrigerant performance
d_{hkl}	Spacing of the $\{hkl\}$ planes of the crystal
f_s	Scaling function
G	Gibbs free energy
g	Spectroscopic splitting factor
H	H-field
H_{app}	Applied H-field
H_D	Demagnetizing H-field
H_I, H_F	Initial and final H-fields
J	Total moment quantum number
K	Compressibility

k_B	Bolztmann constant
L	Layer thickness
l	Lattice parameter
M	Magnetization
N	Number of measurements
n	Field dependence exponent of Δs_T
N_D	Demagnetizing factor
N_m	Density of magnetic moments
N_p	Number of particles
p	Pressure
q	Heat flux per unit mass
r	Field dependence exponent of RCP
RCP	Relative cooling power
RCP_{min}	Minimal relative cooling power
RMS	Root mean square
S	Entropy
s	Specific entropy
s^{ap}	Approximated s determined using calorimetric data starting from T_{ini}
S_M, S_L	Magnetic and lattice entropies
T	Temperature
t	Reduced temperature
T_C	Curie temperature
T_{ini}	Initial temperature of calorimetric data
T_{ini}^{opt}	Optimal initial temperature of calorimetric data
$T_{pk}^{\Delta s_T}$, $T_{pk}^{\Delta T_S}$	Peak temperature of Δs_T and ΔT_S
T_r	Reference temperature
t_r	Reduced reference temperature
T_{trans}	Transition temperature
x	Mass fraction
X, Y	K-F axes

1 Introduction

Magnetic refrigeration at room temperature is an emerging green cooling technology that presents several advantages compared to the conventional gas-based technology. This new technology is based on the magnetocaloric effect which exploits the temperature changes of magnetic materials by magnetic field variations. This chapter briefly describes the basic principles of the magnetocaloric effect, magnetocaloric materials and thermomagnetic phase transitions as well as the conventional models and methods to characterize them. Finally, the objectives and structure of the thesis are also presented.

1.1 Magnetocaloric effect

The magnetocaloric (MC) effect [1–7] is defined as the reversible temperature change produced in a magnetic material upon a magnetic field change under adiabatic conditions. Based on this definition, the MC effect can be characterized by the induced temperature change, which is known as the adiabatic temperature change (ΔT_S). This effect was discovered by P. Weiss and A. Picard in 1917 [8], whereby a temperature change of 0.7 K was observed for a nickel sample upon the application of a magnetic field of 1.5 T at temperatures close to its ferro-paramagnetic phase transition (630 K). Some scientific publications attribute the discovery of the MC effect to E. Warburg in 1881 [9] though the temperature change reported is ascribed, in fact, to the energy losses associated to the magnetic hysteresis [10].

In 1921, P. Weiss established a physical description for the MC effect [11] using the different constituent subsystems of a magnetic material, mainly the magnetic and lattice ones. For the magnetic subsystem, the magnetic moments associated to the atoms are considered while for the lattice subsystem, the spacial distribution of those atoms around an equilibrium configuration is considered. These two different subsystems were well studied separately [12]. Based on that, the entropy (S), an extensive magnitude, can be considered as the sum of the entropy contributions of the different subsystems. Considering only the magnetic and lattice subsystems:

$$S = S_M + S_L, \tag{1.1}$$

where S_M and S_L are the entropies of the magnetic and lattice subsystems, respectively. For a more detailed analysis, different contributions such as the electronic or coupling terms could be included for consideration [2].

Considering the magnetic material under adiabatic conditions when varying the magnetic field from an initial to a final value (H_I and H_F, respectively, being $\Delta H = H_F - H_I$), the total entropy remains constant

($\Delta S(\Delta H) = S(H_F) - S(H_I) = 0$). Thus, using Eq. (1.1) becomes:

$$\Delta S_M(\Delta H) + \Delta S_L(\Delta H) = 0. \tag{1.2}$$

From Eq. (1.2), it can be observed that the magnetic entropy change (ΔS_M) and the lattice entropy change (ΔS_L) are compensated. The different entropy changes are not null when the magnetic field modifies the magnetic/structural state of the material. The implication of Eq. (1.2) can be understood by considering a conventional magnetic material (e.g. ferromagnetic or paramagnetic) for which its structure is not modified by magnetic fields. Typically, the magnetic field aligns the magnetic moments along the direction of the applied magnetic field, reducing the magnetic entropy as the number of configurational states is reduced ($\Delta S_M < 0$ when applying a magnetic field). This ΔS_M is compensated by a ΔS_L (according to Eq. (1.2) $\Delta S_L > 0$). Lattice entropy change leads to a temperature (T) change in the system as S_L mainly depends on the temperature (it was mention that magnetic field does not modify the structure of the material). As the lattice entropy increases with increasing temperature, $\Delta T_S > 0$.

When the application of a magnetic field induces $\Delta T_S > 0$, the effect is termed as direct MC effect. For a general case, ΔT_S can be expressed mathematically as:

$$\Delta T_S(S, \Delta H) = [T(S, H_F) - T(S, H_I)]_S \,, \tag{1.3}$$

where the index S denotes that the difference is at a constant entropy value. It can be observed that the MC effect is induced from the coupling between the lattice and magnetic subsystems of a magnetic material. As the entropy of the system is not an easy experimental parameter to work with, ΔT_S is typically expressed as a function of the initial temperature at which the magnetic field is varied.

Alternatively, under isothermal conditions when varying the magnetic field, a variation of the entropy of the system (known as the isothermal

entropy change, ΔS_T) is induced. This entropy change leads to a heat exchange between the material and the thermal reservoir. From Eq. (1.1) it can be derived that:

$$\Delta S_T(T, \Delta H) = \Delta S_M(T, \Delta H) + \Delta S_L(T, \Delta H). \tag{1.4}$$

For a general case, ΔS_T can be expressed mathematically as:

$$\Delta S_T(T, \Delta H) = [S(T, H_F) - S(T, H_I)]_T\,, \tag{1.5}$$

where the index T denotes that the difference is at a constant temperature. Considering the previous case of a conventional magnetic material, as S_L is a function of temperature, ΔS_T coincides with ΔS_M according to Eq. (1.4) since $\Delta S_L(T, \Delta H) = 0$. It has to be noted that this is not the case when structural changes are produced by magnetic field. This will be further discussed under Section 1.3. Fig. 1.1 shows ΔS_T and ΔT_S at a particular temperature T_0 by the application of a magnetic field for a conventional magnetic material using a schematic $S - T$ diagram.

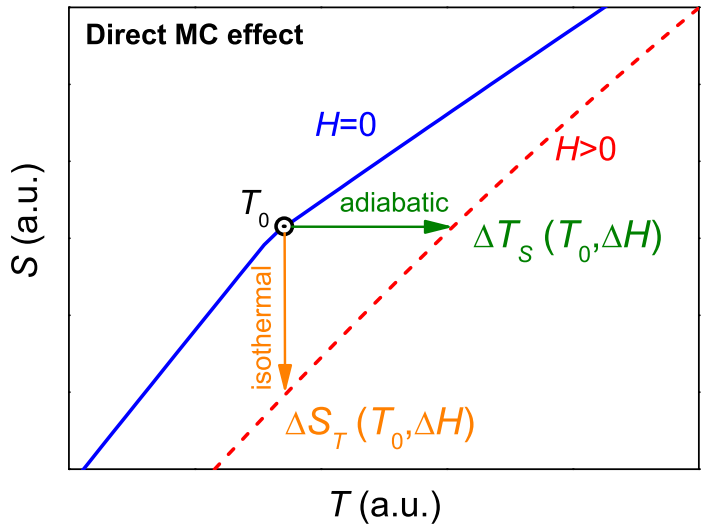

Figure 1.1: Schematic of MC magnitudes, ΔT_S and ΔS_T, from $S_H(T)$ curves upon the application of a magnetic field for a conventional magnetic material, according to Eqs. (1.5) and (1.3), respectively.

ΔS_T and ΔT_S represent the two characteristic magnitudes of the MC effect as function of the initial temperature and the magnetic field change. The reversibility of the MC effect as defined depends on the reversibility of the various processes performed. Moreover, when magnetic field is applied/removed under non-adiabatic or non-isothermal conditions, the system would show an entropy change or temperature change smaller than those under adiabatic or isothermal processes. It has to be noted that ΔS_T is an extensive magnitude (depends on the size of the system) and therefore, it is more useful for the material characterization to use its specific magnitude (Δs_T).

The interest in the MC effect since the 80s has been mainly ascribed to its potential application in solid state magnetic refrigerators at room temperature [13–16]. It is a solid state cooling technology as the working material is a solid, unlike the traditional system based on gas/liquid. The changes in entropy and temperature produced upon application/removal of a magnetic field enable a cycled magnetic refrigeration system [17]. In general, the refrigerator absorbs heat from a certain region (cold load) and rejects heat to exterior (hot reservoir). In the case of a magnetic refrigerator, it consists of a MC material (exhibiting a large MC effect) as the working material, a variable magnetic field generator and a heat transfer fluid system (gas or liquid) between the working material and the different reservoirs. It operates using the combination of various thermodynamic processes, such as adiabatic, isothermal and isofield types. The principal cycles are the Carnot (adiabatic and isothermal processes), Ericsson (isothermal and isofield processes) and Brayton (adiabatic and isofield processes) cycles [18]. Moreover, there is the AMR (Active Magnetic Regenerator) cycle, for which the MC material functions both as a refrigerant and regenerator (it has been shown that it is the most efficient cycle for magnetic refrigeration at room temperature after the Carnot cycle) [19]. Fig. 1.2 schematically shows the basic operation of a magnetic refrigerator using a Brayton cycle. The different steps are illustrated: (a) the MC material is submitted to a magnetic field under adiabatic conditions, leading to an increase of its temperature,

(b) the working material exchanges heat with the hot reservoir reducing its temperature (isofield process), (c) the magnetic field is removed and the material temperature decreases and (d) the resulted cooled material absorbs heat from the cold load until recovers its initial temperature (isofield process). These processes continuously cycle during the operation of the refrigerator.

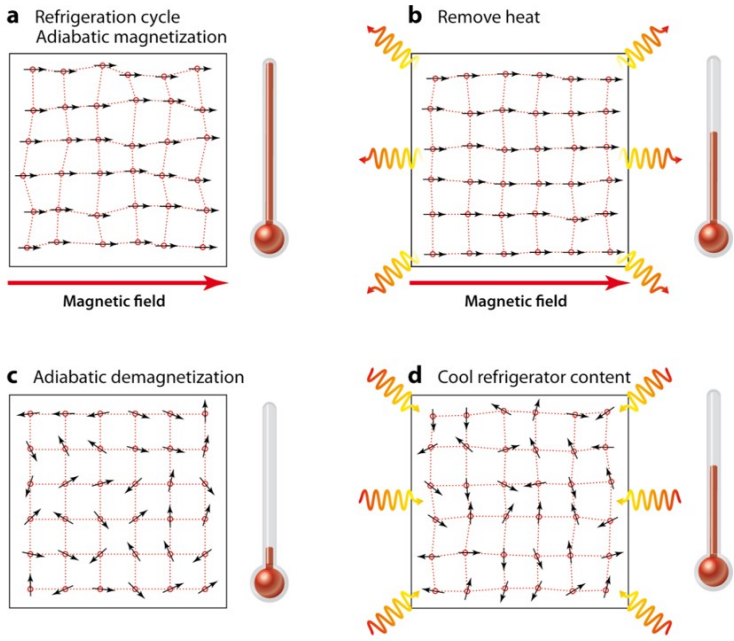

Figure 1.2: Schematic of a magnetic refrigerator operating with a Brayton cycle. Image taken from [20].

Magnetic refrigerators have been shown as more energy efficient than the conventional ones, wherein the best commercial refrigerators reach up to efficiency of 40 % while magnetic refrigerator prototypes can attain up to 60 % (an enhancement of 50 %) [14]. In countries like United States, around 60 % of the energy consumption corresponds to energy losses and, considering that 40 % of the total energy consumption arises from temperature control, an increment in the energy efficiency of refrigerators would lead to great benefits, especially for the economy

and environment [21]. Moreover, the energy consumption rate due to temperature control will notably increase since developing countries mainly coincide with the hottest geographical regions (e.g. Africa, China, India). In addition, this cooling technology, compared to the conventional one, does not require harmful and toxic gases, such as CFCs (ozone depletion), NH_3, HCFCs and HFCs (greenhouse effect) [22]. Nowadays, there are already companies working on the production of commercial magnetic refrigerators. One example would be the commercial wine cooler based on the MC effect, which was presented by HAIER in 2015 (in collaboration with Astronautics of America, BASF and TU Delft) [23]. Besides the interest on magnetic refrigeration, MC materials are also investigated for medical applications [24–26] or energy harvesting devices [17, 27, 28].

1.2 Thermodynamic functions

The MC effect can be related to certain macroscopic variables of the materials, such as magnetization (M) and heat capacity (C) (or their specific magnitudes, σ and c, respectively) through simple thermodynamic relations [2, 29]. By basic thermodynamics, it is well-known that a certain magnitude can be expressed in the equilibrium state, for single component systems, as a function of three independent variables, the so-called state variables. Temperature, magnetic field and pressure (p) are the more favorable state variables as they can be easily controlled experimentally. Therefore, the specific entropy can be expressed as $s = s(T, H, p)$, having a differential form as:

$$\mathrm{d}s = \left(\frac{\partial s}{\partial T}\right)_{H,p} \mathrm{d}T + \left(\frac{\partial s}{\partial(\mu_0 H)}\right)_{T,p} \mathrm{d}(\mu_0 H) + \left(\frac{\partial s}{\partial p}\right)_{H,T} \mathrm{d}p, \qquad (1.6)$$

where the magnetic permeability of vacuum (μ_0) is included. For the study of the MC effect, generally the pressure is kept constant, so $\mathrm{d}p = 0$ (to simplify the notation, the index p is subsequently removed from Eq. (1.6)).

Considering isothermal conditions (i.e. $\mathrm{d}T = 0$) when applying/removing a magnetic field, it can be obtained that:

$$\mathrm{d}s_T = \left(\frac{\partial s}{\partial(\mu_0 H)}\right)_T \mu_0 \mathrm{d}H. \tag{1.7}$$

On the other hand, considering adiabatic conditions (i.e. $\mathrm{d}s = 0$) when applying/removing a magnetic field, Eq. (1.6) becomes:

$$\mathrm{d}T_S = -\left[\left(\frac{\partial s}{\partial T}\right)_H\right]^{-1} \left(\frac{\partial s}{\partial(\mu_0 H)}\right)_T \mu_0 \mathrm{d}H. \tag{1.8}$$

According to Eqs. (1.7) and (1.8), the different derivatives of the entropy (with respect to temperature and magnetic field) have to be expressed as functions of different magnitudes. To do that, c at constant magnetic field is considered:

$$c_H = \left(\frac{đq}{\partial T}\right)_H, \tag{1.9}$$

where đ points that the specific heat flux (q) is not a state function. Assuming quasistatic conditions for the heat flux:

$$đq = T\mathrm{d}s, \tag{1.10}$$

and combining with Eq. (1.9):

$$\left(\frac{\partial s}{\partial T}\right)_H = \frac{c_H}{T}. \tag{1.11}$$

On the other hand, to express the derivative of the entropy with respect to the magnetic field, Maxwell relations have to be considered. These thermodynamic relations arise from the equality of the second derivatives of a certain thermodynamic potential. As T and H are the variables, the most useful thermodynamic potential is the Gibbs free energy (G), taking a differential form as:

$$\mathrm{d}G = -s\mathrm{d}T - \sigma\mathrm{d}(\mu_0 H). \tag{1.12}$$

The Maxwell relation for G leads to:

$$\left(\frac{\partial s}{\partial(\mu_0 H)}\right)_T = \left(\frac{\partial \sigma}{\partial T}\right)_H. \tag{1.13}$$

Using Eqs. (1.11) and (1.13), in Eqs. (1.7) and (1.8):

$$\mathrm{d}s_T = \left(\frac{\partial \sigma}{\partial T}\right)_H \mu_0 \mathrm{d}H, \tag{1.14}$$

$$\mathrm{d}T_S = -\frac{T}{c_H}\left(\frac{\partial \sigma}{\partial T}\right)_H \mu_0 \mathrm{d}H. \tag{1.15}$$

To obtain the entropy and temperature changes produced by a finite magnetic field change, the integration of Eqs. (1.14) and (1.15) have to be performed. For Δs_T, the integration of Eq. (1.14) leads to:

$$\Delta s_T = \mu_0 \int_{H_I}^{H_F} \left(\frac{\partial \sigma}{\partial T}\right)_H \mathrm{d}H. \tag{1.16}$$

In the case of ΔT_S, the integration is not as trivial as for Δs_T. It can be observed that Eq. (1.15) is a transcendental equation (both c_H and σ are functions of T and H) and a separation of variables is not possible. Assuming that in a temperature interval equals to ΔT_S, c_H and σ are temperature-independent:

$$\int_T^{T+\Delta T_S} \frac{\mathrm{d}T}{T} \approx -\mu_0 \int_{H_I}^{H_F} \frac{1}{c_H}\left(\frac{\partial \sigma}{\partial T}\right)_H \mathrm{d}H, \tag{1.17}$$

which it can be expressed as:

$$\Delta T_S \approx T\left[\exp\left(-\mu_0 \int_{H_I}^{H_F} \frac{1}{c_H}\left(\frac{\partial \sigma}{\partial T}\right)_H \mathrm{d}H\right) - 1\right]. \tag{1.18}$$

Assuming that $\Delta T_S/T << 1$, the exponential function can be approximated up to first order, having that:

$$\Delta T_S \approx -\mu_0 \int_{H_I}^{H_F} \frac{T}{c_H}\left(\frac{\partial \sigma}{\partial T}\right)_H \mathrm{d}H. \tag{1.19}$$

Finally, Δs_T and ΔT_S are expressed as functions of measurable magnitudes as σ and c_H (both are functions of temperature and magnetic field).

A relation between Δs_T and ΔT_S magnitudes can be established, though a strong approximation has to be perfomed. Assuming that c_H is field-independent, comparing Eqs. (1.19) and (1.16) it is obtained:

$$\Delta T_S \approx \frac{T \Delta s_T}{c_H}. \tag{1.20}$$

This expression is rather commonly used in the literature though its validity is limited.

On the other hand, it is also possible to obtain the MC magnitudes using heat capacity data. According to the definition of c_H in Eq. (1.9), the entropy at constant magnetic field can be obtained by direct integration, leading to:

$$s_H(T) = s_H(0\ \mathrm{K}) + \int_{0\,\mathrm{K}}^{T} \frac{c_H}{T} \mathrm{d}T. \tag{1.21}$$

In this way, Δs_T and ΔT_S can be obtained from Eqs. (1.5) and (1.3) (illustrated in Fig. 1.1), repectively, where the $s_H(T)$ curves are inverted to $T_H(s)$ to express ΔT_S. In this case, it can be observed that Δs_T and ΔT_S are obtained using only heat capacity data while only Δs_T can be obtained from magnetization measurements (Eq. (1.16)).

There is another important magnitude to characterize the performance of a MC material in a magnetic refrigerator, which is the refrigerant capacity. It is defined as the heat transferred from the cold to the hot reservoir in the refrigeration cycle. To establish a criterion to evaluate the response of the material without its inclusion in a refrigerator, implying that reservoir temperatures are unknown, it is assumed that the temperature span coincides with the full width at half maximum of $\Delta s_T(T)$ curves (ΔT_{FWHM}) and then the refrigerant capacity is approximated to the

relative cooling power (RCP) [30]:

$$RCP = -\Delta s_T^{pk} \Delta T_{FWHM}, \tag{1.22}$$

where Δs_T^{pk} is the peak value of Δs_T. The values obtained for RCP has to be carefully analyzed as low values for Δs_T can lead to high values for ΔT_{FWHM}, which are not accessible under real conditions, giving false high RCP values. When ΔT_S data are known, it is possible to overcome this misinterpretation by using RCP_{min}, which uses ΔT_S^{pk} (peak value of ΔT_S) instead of ΔT_{FWHM}, and considers the minimal area enclosed by the $s_H(T)$ lines during a cycle [31]. The minimal coefficient of refrigerant performance (CRP_{min}) normalizes the RCP_{min} by the energy cost to magnetize/demagnetize the MC material:

$$CRP_{min} = \frac{RCP_{min}}{\mu_0 \int_{H_I}^{H_F} \sigma \, \mathrm{d}H}. \tag{1.23}$$

1.3 Magnetocaloric materials

For both Δs_T and ΔT_S magnitudes (Eqs. (1.16) and (1.19)), it is observed that a large temperature dependence of magnetization leads to large values of these magnitudes. This led to the first application of the MC effect: the adiabatic demagnetization of paramagnetic salts. They exhibit a strong temperature dependence of the magnetization close to 0 K, which leads to high ΔT_S values at low temperatures. In 1933, W.F. Giauque and D.P. MacDougall attained temperatures below 1 K using the adiabatic demagnetization of $Gd_2(SO_4)_{3.8}{\cdot}H_2O$ paramagnetic salts in a liquid He bath [32]. They were awarded the Nobel prize in Chemistry in 1949 for this achievement. Nowadays, molecular magnets are shown as a excellent alternative to the paramagnetics salts at low temperatures [33, 34].

For higher temperatures, it is possible to obtain high values of $\mathrm{d}\sigma/\mathrm{d}T$ in the region close to a thermomagnetic phase transition. This was

observed by P. Weiss and A. Picard at the temperature region close to the ferro-paramagnetic phase transition of Ni. For application of this effect at room temperature in a magnetic refrigerator, the thermomagnetic phase transition is required to occur at temperatures close to 300 K.

Phase transitions are mainly classified as first (FOPT) and second order (SOPT) phase transitions, according to the Ehrenfest's classification [35]. A FOPT is characterized by a discontinuity in the first derivative of the free energy (e.g. magnetization) and a divergence in the second derivative (e.g. heat capacity), which leads to the existence of latent heat, phase coexistence and hysteresis phenomena. On the other hand, a SOPT is characterized by a continuous variation of the first derivative of the free energy while there is a discontinuity in the second derivative of the free energy. A SOPT leads to a continuous phase transformation. With this, MC materials are categorized by the same classification.

Since the application of ultra low temperatures, the magnetic refrigeration was still not a widely studied field until in 1976 G.V. Brown developed a magnetic refrigerator based on Gd as the working material (which exhibits a ferro-paramagnetic SOPT at 293 K) [13]. Magnetic field changes up to 7 T were applied, reaching up to a temperature span of 47 K (from -1 ^{o}C to 46 ^{o}C). The developed magnetic refrigerator had two main drawbacks for commercialization: the high price of Gd (a rare-earth element that is only available in specific regions) and the magnetic field generator based on superconductor magnets (which needs liquid He refrigeration). With this, MC research evolved to the search for potential alternatives to Gd, starting with several SOPT MC materials as the focus. However, this is not easy as Gd exhibits a high value of magnetization. Another approximation to improve the SOPT MC response is through multiphase [36–38] or structured materials [39–41] in which larger values of RCP are obtained in comparison to their single phase counterparts.

In 1997, V.K. Pecharsky and K. Gschneidner discovered a high MC response (thermed as giant MC effect) in $Gd_5Si_2Ge_2$ (with a ΔT_S of 16 K

around 276 K for 5 T, which is a 30 % larger than that of Gd) associated to a FOPT transition (from an orthorhombic Sm_5Ge_4-type phase at low temperatures to a monoclinic $Gd_5Si_2Ge_2$-type at high temperatures) [42]. This compound shows similar values to those previously discovered for FeRh [43] without the drawbacks of costly price and large hysteresis. Fig. 1.3 compares Δs_T (A) and ΔT_S (B) of FOPT and SOPT MC materials using Gd and $Gd_5Si_2Ge_2$ as the examples.

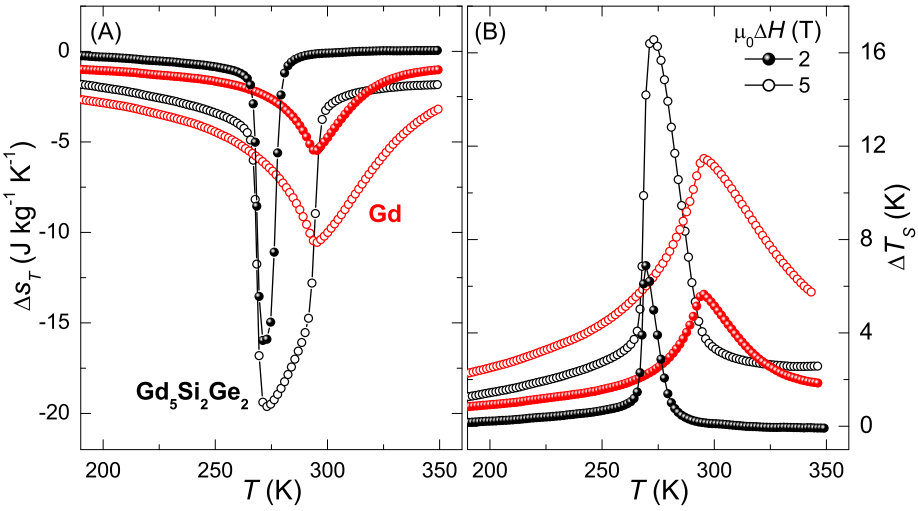

Figure 1.3: Temperature dependence of Δs_T (A) and ΔT_S (B) for Gd and $Gd_5Si_2Ge_2$ for a magnetic field change of 2 and 5 T. Data provided by Prof. Pecharsky, Ames Laboratory [42].

Typically, FOPT MC materials present a higher response than those of SOPT cases despite a narrow temperature span (as seen for Δs_T and ΔT_S). With respect to the field dependence shown in Fig. 1.3, the curves for Gd show that MC magnitudes increase with field (without significant shift of their corresponding temperatures) while for those of $Gd_5Si_2Ge_2$, their responses shift to higher temperatures with field. For that, the field dependence studies demonstrate become a good tool to classify and identify the types of MC materials (Section 4.3).

Since the discovery of $Gd_5Si_2Ge_2$, several FOPT MC materials have been studied for their application in magnetic refrigerators at room temperature, such as the $La(Fe,Si)_{13}$- [44–47], Heusler- [48–55] or MnFeP- [56–58] type compounds among others. Fig. 1.4 shows ΔT_S^{pk} for a magnetic field change of 2 T as a function of the transition temperature (T_{trans}) for some typical MC materials (both SOPT and FOPT). It is observed that a maximum value of ~ 9 K was reached for $Fe_{49}Rh_{51}$ alloy while Gd still displays a significant value among the different materials.

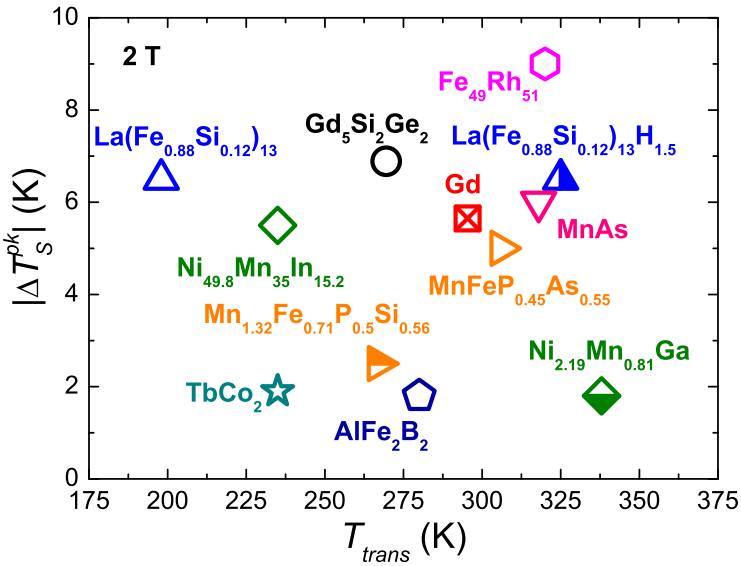

Figure 1.4: ΔT_S^{pk} for a magnetic field change of 2 T as a function of T_{trans} for some typical MC materials. Data taken from [4, 42, 44, 58–64].

The discovery of the MC effect associated to a FOPT led to a new phenomenology compared to the one ascribed to the SOPT [59]. For a FOPT MC material, it is also possible to obtain, besides the direct MC effect (which was always observed up to that moment), the so-called inverse MC effect, for which $\Delta S_T > 0$ and $\Delta T_S < 0$ upon an application of magnetic field [49]. To explain this, it has to be noted that FOPT have associated volume changes that are produced by a lattice expansion/compression (magnetoelastic transition) or by a structural

change (magnetostructural transition) with an associated latent heat (in such cases, $\Delta S_L \neq 0$). If the application of magnetic field leads to an abrupt lattice change to a more stable phase, a remarkable ΔS_L value is attained (with a positive sign). If the associated value is larger than ΔS_M (which is always negative), $\Delta S_T > 0$ when appliying a magnetic field. Fig. 1.5 shows the schematic representation of the direct and inverse MC effects associated to a FOPT using their associated $M - T$ and $S - T$ diagrams.

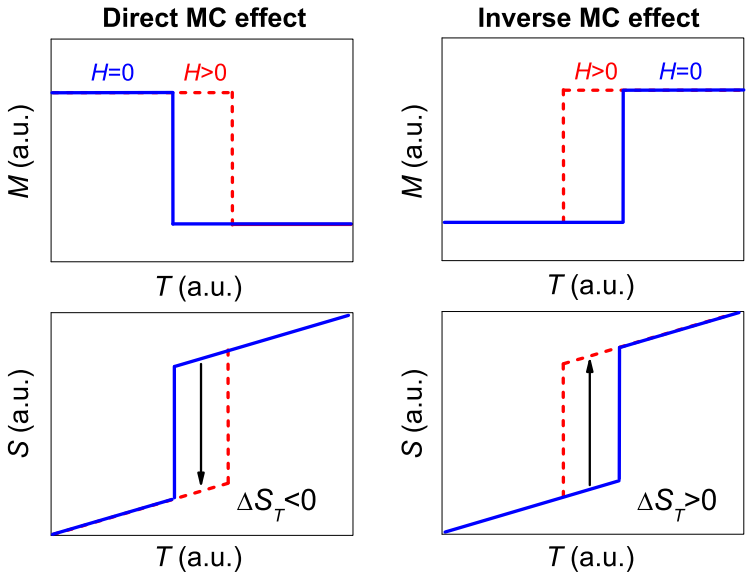

Figure 1.5: Schematic representation of the direct and inverse MC effect associated to a FOPT MC material.

For direct MC effect, the magnetic field stabilizes the low temperature phase (which corresponds to the high magnetization phase) while for the inverse effect, the high temperature phase (which also corresponds to the high magnetization phase) is stabilized by the magnetic field. When the transition occurs, the lattice entropy increases and when the magnetic field stabilizes the low temperature phase, the produced isothermal entropy change is negative. If the high temperature phase is stabilized, the result is a positive isothermal entropy change. There is another way to characterize

the effects, which is by the shift of the transition temperature with magnetic field: for direct MC effect, the transition temperature shifts to higher temperatures while for the inverse, it shifts to lower temperatures.

Although it is shown that FOPT MC materials have a relatively large response (larger than SOPT MC materials), it is accompained by thermal and magnetic hysteresis, which is susceptible to rate dependence and a decreased cyclic performance. On the other hand, SOPT materials do not exhibit any thermal hysteresis. One goal of MC material research is to combine the pros from both types of materials: large response without associated hysteresis [65–68]. With this goal, many have attempted to develop series of alloys and compounds that can bring us to the intermediate point between two different order of phase transitions (also known as the critical SOPT-FOPT point). Some of the most studied families of FOPT MC materials (e.g. $La(Fe,Si)_{13}$ [47, 69] and MnFe(P,Si) [70] compounds) show a gradual change from FOPT to SOPT by means of composition modification or element additions (e.g. for $La(Fe,Si)_{13}$, the critical SOPT-FOPT composition was found for a 12.7 at.% of Si content [71]).

One of the most promising family of MC materials are $La(Fe,Si)_{13}$ compounds. They are based on abundant, non-critical and non-contaminant elements. The $NaZn_{13}$-type structure presented in these compounds (Si incorporation is needed to stabilize the phase) shows a temperature-induced FOPT ferro-paramagnetic transition (as well as field-induced para-ferromagnetic transition) around 200 K (dependent on the Si content). The origin of this magnetic field-dependent transition is ascribed to the itinerant-electron metamagnetism of these compounds [72, 73]. The corresponding FOPT leads to a MC effect with moderate thermal hysteresis (compared to other FOPT MC materials, such as FeRh or Heusler alloys) and with associated volume change of around 1% without structural change (magneto-elastic transition). The transition temperature can be shifted to temperatures closer to room temperature by hydrogenation, whereby the $NaZn_{13}$-type unit cell expands, facilitating the

applications of the material [44]. Still, they exhibit some issues impeding commercialization [74], such as material degradation under cycling [75–77], accompanying hysteresis [78, 79], mechanical stability [80–82], etc.

One of the aims of this thesis is to use the proposed analysis to explore different optimization routes of MC materials that are based on benchmark Gd-(SOPT) and $La(Fe,Si)_{13}$-(FOPT) systems. For the former, it is focused on attaining improved RCP and field responsiveness while the latter is dedicated to increasing the FOPT-character or reducing the accompanying hysteresis.

1.4 Conventional models and methods

It is already shown the close link between MC effect and thermomagnetic phase transitions. Hence, MC studies allow us to obtain information about the nature of the phase transition. The conventional methods and models used in literature for such purposes (also used for the various analyses in this thesis) will be discussed in the following sections.

1.4.1 Arrott-Noakes equation of state

In the critical region of a SOPT (i.e. $T \approx T_C$ and $H \approx 0$, being T_C the Curie temperature), the different magnitudes can be expressed as a power law of certain variables, where the exponents of the power laws are called critical exponents [83, 84]. These critical exponents depend only on the nature of the phase transition. The origin of this critical behavior can be understood by the meanings of the fluctuations of the systems. A relatively simple analysis was performed by using mean field theories (e.g. the Landau theory) giving a satisfactory explanation (in a qualitatively manner). For a detailed analysis (beyond mean field theories), a more sophisticated mathematical formalism is needed (such as the Wilson's

renormalization group theory). These analyses go beyond the scope of this thesis.

In the case of σ, for $T < T_C$ and $H = 0$, it can be expressed in the critical region as:

$$\sigma(H = 0) \propto (T_C - T)^{\beta}, \tag{1.24}$$

while for $T = T_C$:

$$\sigma(T = T_C) \propto H^{1/\delta}, \tag{1.25}$$

where β and δ are critical exponents. In the case of the magnetic susceptibility (χ) for $T > T_C$ and $H = 0$, it can be expressed as:

$$\chi(H = 0) \propto (T - T_C)^{\gamma}, \tag{1.26}$$

being γ the associated critical exponent. These critical exponents are related by:

$$\delta - 1 = \frac{\gamma}{\beta}. \tag{1.27}$$

In a general form, it can be established that the magnetization scales at the critical region as:

$$\frac{H}{\sigma^{\delta}} = f_s\left(\frac{t}{\sigma^{1/\beta}}\right), \tag{1.28}$$

where f_s is a scaling function and $t = (T - T_C)/T_C$.

Combining Eqs. (1.24), (1.25) and (1.26), A. Arrott and J.E. Noakes proposed the followed phenomenological equation of state (EOS) for Ni close its transition temperature [85]:

$$\left(\frac{H}{\sigma}\right)^{1/\gamma} = a\,(T - T_C) + b\sigma^{1/\beta}, \tag{1.29}$$

where a and b are two introduced parameters. It has to be noted that Eqs. (1.24), (1.25) and (1.26) can be recovered from Eq. (1.29).

The Arrott-Noakes (A-N) EOS has been succesfully used to describe the MC response of different SOPT MC materials apart from Ni [86–89]. To

determine the A-N parameters, a 3D-fitting was proposed by V. Franco in [87]. This method proposes the temperature as the fitting variable to avoid multivalued solutions, which could complicate the procedure.

The A-N EOS was used to numerically describe the MC behavior of the SOPT MC materials studied in this thesis.

1.4.2 Kouvel-Fisher method

The Kouvel–Fisher (K-F) method is an iterative procedure to determine the critical exponents of the materials proposed by J.S. Kouvel and M.E. Fisher in 1964 [84]. The proposed method is based on the magnetic behavior close to the critical region (Eqs. (1.24) and (1.25)).

For the first step in the method, $\sigma_T(H)$ data, using an initial set of critical exponents, are represented in a modified Arrott plot (which represents $(H/\sigma)^{1/\gamma}$ vs. $\sigma^{1/\beta}$ at a certain temperature). From this plot, the $\sigma(H=0)$ and the inverse of the magnetic susceptibility at zero field ($\chi^{-1}(H=0)$) are obtained from the intercepts of each axis. After that, the obtained $\sigma(H=0)$ and $\chi^{-1}(H=0)$ values (as a function of the temperature) are used to obtain a new set of β and γ critical exponents from the slope of the Y and X axes vs. temperature plots, respectively, being:

$$Y = \sigma(H=0)\left(\frac{\partial\sigma(H=0)}{\partial T}\right)^{-1} = \frac{1}{\beta}(T - T_C), \tag{1.30}$$

$$X = \chi^{-1}(H=0)\left(\frac{\partial\chi^{-1}(H=0)}{\partial T}\right)^{-1} = \frac{1}{\gamma}(T - T_C). \tag{1.31}$$

With the obtained set of critical exponents, the sequence is repeated (starting from the modified Arrott plot) until the obtained critical exponents converge to constant values (which are the final values for the critical exponents). This method is not straightforward and requires time-consuming and careful data analysis. Apart from β and γ, T_C is also obtained as the average intercept of both curves in the temperature

axis (ideally, they should be the same). These limitations, on top of K-F technique limited to single phase SOPT materials, are overcome by a newly proposed method as described in Chapter 4.

1.4.3 Scaling laws for the magnetocaloric effect

Near to the critical region, it is possible to extend the scaling laws to the MC effect [90–92] due to the strong correlation with thermomagnetic phase transitions. To obtain the MC relations, the different scaling relations for the magnetization can be expressed as (among others):

$$\frac{\sigma}{|t|^{\beta}} = f_{s,\pm}^{(0)}\left(\frac{H}{|t|^{\Delta}}\right), \tag{1.32}$$

where $\Delta = \beta\gamma$ and $f_{s,\pm}^{(0)}$ is a scaling function (where + and − signs correspond to the regions of $t < 0$ and $t > 0$, respectively). Introducing Eq. (1.32) into Eq. (1.16) and assuming a zero initial magnetic field:

$$\Delta s_T = \pm\Delta s_T^{(0)}|t|^{1-\alpha}\int_0^{\Delta H/|t|^{\Delta}}\left(\beta f_{s,\pm}(\varrho) - \Delta\frac{\partial f_{s,\pm}(\varrho)}{\partial\varrho}\varrho\right)\mathrm{d}\varrho, \tag{1.33}$$

where $\Delta s_T^{(0)}$ is a constant, $1-\alpha = \beta + \Delta - 1$ and $\varrho = H/|t|^{\Delta}$. Although $f_{s,\pm}^{(0)}$ is unknown, it can be observed that the integral of Eq. (1.33) is also a function of ϱ, having:

$$\Delta s_T = |t|^{1-\alpha} f_{s,\pm}^{(1)}\left(\frac{\Delta H}{|t|^{\Delta}}\right), \tag{1.34}$$

where $f_{s,\pm}^{(1)}$ is a new defined function. After some algebra, Eq. (1.34) can be converted to:

$$\frac{\Delta s_T}{\Delta H^{(1-\alpha)/\Delta}} = f_{s,\pm}^{(2)}\left(\frac{|t|}{\Delta H^{1/\Delta}}\right), \tag{1.35}$$

where $f_{s,\pm}^{(2)}$ is a new defined function. Eq. (1.35) expresses the scaling law for Δs_T in the critical region, which allows much information of the nature of the MC properties to be obtained from SOPT MC materials. As

an example, scaling laws of typical Δs_T curves of amorphous alloys using A-N EOS with Heisenberg critical exponents are illustrated in Fig. 1.6. It can be observed that Δs_T curves for different magnetic field changes (A) collapse onto a single curve (B).

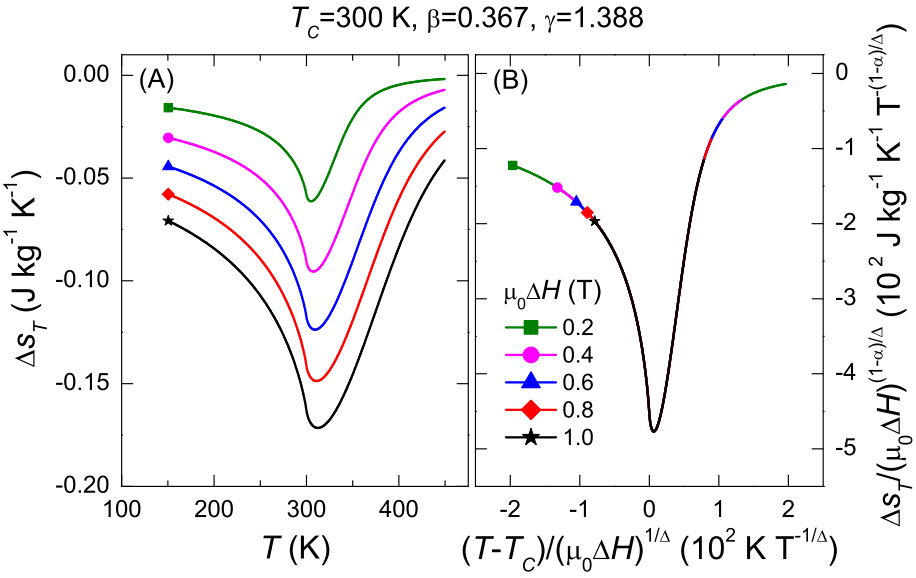

Figure 1.6: Temperature dependence of Δs_T using A-N EOS with Heisenberg critical exponents and typical parameters for amorphous alloys (A) and scaled curve according to Eq. (1.35) (B).

Using Eq. (1.35), it is possible to examine the magnetic field dependence for SOPT MC materials. For $T = T_C$ ($t = 0$), it can be observed that:

$$\Delta s_T(T = T_C) \propto \Delta H^{(1-\alpha)/\Delta}, \tag{1.36}$$

i.e. $\Delta s_T(T = T_C)$ follows a power law with an exponent that is a function of different critical exponents. This leads to the definition of the field dependence exponent, n, as:

$$n(T, \Delta H) = \frac{\partial \ln \Delta s_T(T, \Delta H)}{\partial \ln \Delta H}. \tag{1.37}$$

Combining Eqs. (1.36) and (1.37):

$$n(T = T_C, \Delta H) = (1 - \alpha)/\Delta. \tag{1.38}$$

For non-zero values of t, a certain value of reference temperature (T_r) can be chosen to quantify the width of Δs_T for a certain ΔH, i.e.:

$$\Delta s_T(T_r, \Delta H) = \Delta s_T^{(1)} \cdot \Delta s_T(T = T_C, \Delta H), \tag{1.39}$$

where $\Delta s_T^{(1)}$ is a constant value (normally it is chosen between 0.7 and 0.5 to ensure that T_r is chosen near the critical region). T_r corresponds to the temperature for which Δs_T corresponds to that fraction of the peak. Using Eqs. (1.35) and (1.39), it can be observed that for t_r $\left(\frac{T_r - T_C}{T_C}\right)$:

$$t_r \propto \Delta H^{1/\Delta}, \tag{1.40}$$

i.e. the width of Δs_T follows a power law with an exponent that is the inverse of the critical exponent Δ. It has to be noted that, as the different branches for $t > 0$ or $t < 0$ are specified in Eq. (1.32), one t_r is selected for each branch (following the same notation, t_{r+} and t_{r-}, respectively).

One important feature is that by determining the field dependences of $\Delta s_T(T = T_C)$ and t_r, it is possible to determine the critical exponents of the transitions using Eqs. (1.36) and (1.39) (having a two-equation system with two variables, α and Δ). Once these critical exponents are obtained, other exponents can be determined using different relations. This analysis can be extended to other MC magnitudes, such as Δs_T^{pk}, its corresponding temperature ($T_{pk}^{\Delta s_T}$) or RCP. Table 1.1 shows some of the critical exponents of the power field dependence for different MC magnitudes [92]. Moreover, according to Eqs. (1.36) and (1.39) with the determination of $\Delta s_T(T = T_C)$ (or Δs_T^{pk} due to the same field dependence) and t_r, a phenomenological universal curve can be constructed without previous assumption or calculus to determine the critical exponents. This phenomenological curve has been widely studied and applied for several

SOPT MC materials, finding an excellent agreement between experiments and theory [93–97].

Magnitude	Exponent
Δs_T^{pk}	$(1-\alpha)/\Delta = 1 + 1/\delta(1-1/\beta)$
$\Delta s_T(T = T_C)$	$(1-\alpha)/\Delta = 1 + 1/\delta(1-1/\beta)$
RCP	$1 + 1/\delta$
$t_{r,\pm}$	$1/\Delta$
$T_{pk}^{\Delta s_T} - T_C$	$1/\Delta$ (0 for mean field)

Table 1.1: Exponents of the power field dependence for different MC magnitudes.

Based on these scaling laws, different procedures to determine T_C and the critical exponents for SOPT materials were developed in this thesis, which are further found to be field-independent for T_C as well as applicable for studying the critical exponents of biphasic systems (which are not possible by the conventional methods). These new methods will be shown in Chapter 4. Furthermore, these analyses, previously not used for studying FOPT MC materials (these are not based on critical exponents), will be shown applicable to identify the phase transition order and the critical SOPT-FOPT (Section 4.3).

1.4.4 Bean-Rodbell model

In 1962, C.P. Bean and D.S. Rodbell proposed a model to study the ferro-paramagnetic FOPT with an associated volume change (≈ 2.5 %) in MnAs [98]. From this, they assumed that magnetic interactions are related to the interatomic distances of the material, proposing a phenomenological dependence for the transition temperature as:

$$T_{trans} = T_C \left(1 + \Psi \Delta v\right), \tag{1.41}$$

where Δv is the relative volume change and Ψ is a parameter to express the dependence of the transition temperature with the deformations.

Considering G for a mean field approach:

$$G = -\mu_0 HM - \lambda M^2 + p\Delta v + \frac{1}{2K}\Delta v^2 - Ts, \tag{1.42}$$

where K is the compressibility. The first term arises due to external field, the second to the exchange interaction, the third to the external pressure, the forth to the lattice distortion and the last to the entropy contribution. Both Eqs. (1.41) and (1.42) are related by the exchange constant:

$$\lambda = \frac{3k_B T_{trans}}{J(J+1)N_m(g\mu_B)^2\mu_0}, \tag{1.43}$$

where J is the total moment quantum number, N_m is the density of magnetic moments, g is the spectroscopic splitting factor and k_B is the Boltzmann constant.

According to basic thermodynamics, the equilibrium values of the different magnitudes are those that minimize G. Combining Eqs. (1.42) and (1.43), the relative volume change when G is minimal is expressed as:

$$\Delta v = \frac{3}{2}\frac{J}{J+1}N_m k_B T_C K \Psi M^2. \tag{1.44}$$

From Eq. (1.44), it can be observed that Δv is obtained as a function of M. Introducing Eq. (1.44) into Eq. (1.42), the magnetization when G is minimal is expressed as:

$$M = N_m g\mu_B J\mathcal{B}\left(\frac{\mu_0 g\mu_B J}{k_B T}(H + \lambda^{(1)}M + \lambda^{(3)}M^3)\right), \tag{1.45}$$

where $\mathcal{B}$ is the Brillouin function and:

$$\lambda^{(1)} = \frac{3k_B T_C}{J(J+1)N_m(g\mu_B)^2\mu_0}, \tag{1.46}$$

$$\lambda^{(3)} = \frac{3}{10}\frac{2J^2+2J+1}{J^2(J^2+1)(N_m g\mu_B)^2}\lambda_0\eta, \tag{1.47}$$

being η:

$$\eta = \frac{5J(J+1)}{2J^2+2J+1} N_m k_B T_C K \Psi^2. \tag{1.48}$$

Fig. 1.7 shows the temperature dependence of normalized magnetization calculated using Bean-Rodbell (B-R) model with different η values.

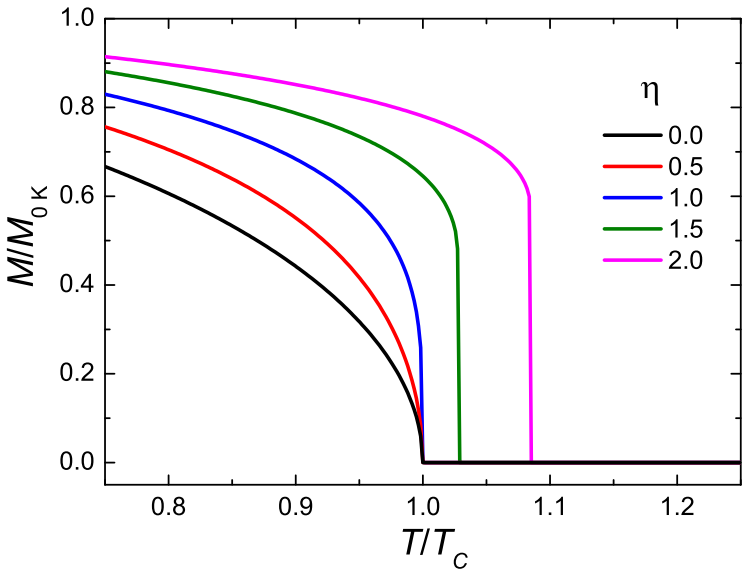

Figure 1.7: Temperature dependence of normalized magnetization calculated using B-R model with different η values (calculated using the corresponding parameters of Gd).

The η parameter controls the order of the transition, being $\eta > 1$ for FOPT (an abrupt M variation with T from the ferro- to para-magnetic state is obtained) and $\eta < 1$ for SOPT (smooth M variation with T is obtained). In the case of $\eta = 1$, it corresponds to the critical SOPT-FOPT point. The B-R model has been successfully applied to describing the MC properties of different materials apart from MnAs as well as $Gd_5Si_2Ge_2$ or $La(Fe,Si)_{13}$ compounds [99–103]. The magnetoelastic FOPT of the MC compounds was numerically modeled using this model and compared to experimental, which are presented in Chapters 4 and 6.

1.4.5 Banerjee's criterion

In 1964, S.K. Banerjee proposed a criterion to distinguish the order of thermomagnetic phase transition [104]. The criterion is based on the analysis of the power expansion of G as a function of M in terms of the B-R model. For the classical mean field approach described by the Landau-Lifshizt theory, the fourth-order term is positive (SOPT), while for the B-R model, the volume-magnetic coupling leads to the possibility of both signs for the fourth-order term. By comparing both models, S.K. Banerjee established that the term should be negative for FOPT while positive for SOPT. According to this, the Arrott plots of FOPT materials show negative slopes according to the negative sign of the fourth-order term of the expansion. For SOPT, only positive values have to be observed.

Banerjee's criterion is widely used though it has to be highlighted that it is based on mean field assumptions, which can lead to discrepancies in comparison to other methods, as reported in literature [94, 105–107]. This is also encountered when applying this criterion to study the MC behavior of $La(Fe,Si)_{13}$-based system studied in this thesis, which is further covered in Chapter 6. These discrepancies are then overcome by new criteria based on the MC effect.

1.5 Objectives and structure of the thesis

The aim of the thesis is two-fold: (i) to study the various methods of analysis based on the MC effect for extracting information on the magnetic behavior and thermomagnetic phase transition nature of magnetic materials as well as (ii) to use them for investigating possible avenues for optimizing the behavior of MC materials. Hence, the first part of the thesis focuses on the development and application of different methods to analyze the MC effect, which includes considering for the various aspects associated to experimental measurements for an

appropriate interpretation of the response. The results are compared to those obtained by conventional methods and further show that the proposed techniques are applicable for studying FOPT and SOPT MC materials. They are also demonstrated to overcome the limitations encountered by the conventional methods, extending their applicabilities. Both experimental and numerical studies were performed to check the validity of the proposed methods, finding excellent agreement. The second part of the thesis is dedicated to MC materials development for investigating various possible avenues to optimize MC behavior by tapping on the characteristics of FOPT and SOPT systems. The previously developed methods of MC analyses were also further applied to studying these developed materials, which yields additional information related to their thermomagnetic phase transitions.

The outline of the thesis structure after the introduction comprises of:

- A brief note on the experimental techniques used for characterizing the microstructures, magnetic and MC properties of the studied materials are described in Chapter 2.
- Studies on the influence of experimental factors, such as sample geometry or compositional inhomogeneities on the MC results are presented in Chapter 3. They also include the role of low-temperature limitation of heat capacity data and the type of measurement protocols in direct ΔT_S measurements for the determination of the MC effect.
- Various analysis methods based on the MC effect were developed to study the magnetic properties and thermomagnetic phase transitions of the materials, both experimentally and numerically verified, are described in Chapter 4. They enabled the determination of T_C, critical exponents in biphasic systems, order of the phase transition as well as the critical SOPT-FOPT composition.

- Optimization of the response of SOPT MC materials based on Gd-GdZn composites and Gd/Ti multilayers, is presented in Chapter 5. Unlike the typical alloying additions for the search and development of MC materials, their RCP and field responsiveness of MC effect are optimized via careful selection of T_C and phases as well as appropriate multilayers material with varying thickness.

- Optimization of FOPT MC materials is illustrated via the reduction of hysteresis and enhancement of FOPT character in $La(Fe,Si)_{13}$-based series and presented in Chapter 6. This is attained by Ni and Cr additions, which are previously not systematically studied for the hysteresis, determination of FOPT-character as well as the critical SOPT-FOPT composition. Their MC responses were analyzed by the earlier proposed MC analysis methods, showing to overcome the discrepancies when studied by Banerjee's criterion.

2 Experimental techniques

In this chapter, the techniques used for the synthesis and for microstructural, magnetic and MC characterization of the studied materials are briefly described.

2.1 Induction melting

Induction melting allows to produce melted ingots by hysteresis and eddy-current losses caused when the materials (electrically conducting) are placed in a varying magnetic field. Magnetic field is generated by induction coils in which high frequency electrical current passes trough. To prevent oxidation during the melting, the material is in high vacuum. The resulting ingot is remelted 3-4 times to ensure a good homogeneity.

2.2 Arc melting/Suction casting

Arc melting allows to produce metal ingots by the melting of different metals by passing through them an electrical current. The device consists in a electrode and a crucible (made of cooper) that is surrounded by a water jacket used to cool down the device and control the solidification rate. Several grams (~ 5 g) of the materials, located on top of the crucible, are melted by the action of the electrical current (with an intensity of several kA). The chamber, where the material is located, is under high vacuum or Ar atmosphere to avoid oxidation. The resulting ingot is remelted 3-4 times to ensure a good homogeneity.

Additionally, a suction casting option can be implemented in the arc melter. This technique allows to cast the melted material by arc melting into a mold cavity (of different geometries) by using vacuum. Cooling rates around 10^3 K s^{-1} are achievable, facilitating the attainment of meta-stable phases.

2.3 X-ray diffraction

X-ray diffraction (XRD) experiments obtain information of the atomic structure of a material by the incidence of a X-ray beam, with

wavelength (λ_w) close to the interatomic distances ($\sim$ Å). This technique is based on the interference of the elastic dispersed X-rays by the electronic clouds of the atoms, which presents a diffraction pattern. For crystalline materials, the diffracted directions are related to the crystal periodicity through the Laue condition. This condition can be expressed in an scalar way (Bragg's condition) as:

$$\lambda_w = 2d_{hkl}sin\theta, \tag{2.1}$$

being 2θ the angle between the incident and diffracted beams and d_{hkl} is the spacing of the $\{hkl\}$ planes of the crystal. The Bragg's condition refers to the direction of the diffracted beams, related with the crystal periodicity, while the relative intensity of the different beams is determined by the structural base of the crystal.

XRD diagrams of pulverized samples were collected at room temperature using a Bruker D8I, in reflection mode with geomety $\theta/2\theta$, with selected Cu $K_{\alpha 1}$ radiation (λ_w = 1.54184 Å) and a Stoe Stadi P instrument in transmission mode with Molybdenum $K_{\alpha 1}$ source radiation ($\lambda_w = 0.70930$ Å). For phase quantification, Rietveld refinements were performed using the TOPAS Version 6.0 software.

2.4 Scanning electron microscopy

Scanning electron microscopy technique obtains images (among other information such as texture, chemical composition, crystalline structure...) from a sample using an incident electron beam. This technique arises from the necessity of improving the resolution of the optical microscopes, which is achieved by the use of electrons that exhibit much smaller wavelengths than that of visible light. The electrons are generated in a cathode by thermoionic effect or by field emission and accelerated by an electrical field. A set of electromagnetic lenses focuses the beam and other set of coils (deflectors) moves the beam to scan the surface of the sample. To avoid

that the electron beam is degraded, the chamber has to be in high vacuum. Electrons are strongly attenuated inside the sample via elastic or inelastic collisions (the attenuation coefficient depends on the material) and are able to penetrate distances of around μm within the sample (depending on the accelerating voltage). The different products of the interactions between the beam-sample from which information is obtained are: secondary electrons, backscattered electrons (BSE) and characteristic X-rays. BSE are those that collide elastically with the sample, strongly changing the direction of movement (more probable as the atomic number increases). Secondary electrons are those electrons which are knocked out from the atoms and emitted due to inelastic collisions. These electrons have low energy and only escape from the sample if the process has taken place very close to the surface, being strongly dependent on the topography of the sample. With this, X-ray emission is also produced, which is characteristic of the atoms of the sample. From this X-ray emission, by using the energy dispersive espectroscopy (EDX) technique, it is possible to obtain information of the different atoms (and their proportion) on the surface sample.

A Philips XL30 FEG scanning electron microscope equipped with energy-dispersive X ray system (SEM/EDX) was used.

2.5 Vibrating sample magnetometry

A vibrating sample magnetometer is an instrument that measures the magnetic moment of a sample under an uniform applied magnetic field. The operating principle is based on the Faraday's law. The magnetic sample is made to oscillate at a fixed frequency which leads to a change in the magnetic flux through a set of detection coils in the surroundings. This flux variation induces an AC electromotive force in the coil that is directly proportional to the magnetic moment of the sample. The signal is amplified by a lock-in amplifier, which rejects all the signals with

different frequencies to the sample oscillation, increasing the sensitivity in the measurement.

Magnetic moment measurements were performed using a LakeShore 7407 (with oven and cryostat options, in which magnetic measurements were performed from liquid nitrogen temperature up to 1273 K) and in a Quantum Design Physical Properties Measurement System with vibrating sample magnetometer option.

Δs_T is determined experimentally from specific moment measurements (as a function of temperature and magnetic field, $\sigma(T, H)$) following the discrete form of equation Eq. (1.16):

$$\Delta s_T\left(\frac{T_{i+1}+T_i}{2}, H_N - H_1\right) = \frac{\mu_0}{2}\times \sum_{j=1}^{N-1}\left(\frac{\sigma(T_{i+1}, H_{j+1}) - \sigma(T_i, H_{j+1})}{T_{i+1}-T_i} + \frac{\sigma(T_{i+1}, H_j) - \sigma(T_i, H_j)}{T_{i+1}-T_i}\right)\times (H_{j+1} - H_j), \quad (2.2)$$

where the indexes i and j represent different values of T and H, respectively, N is the number of measurements and H_N and H_1 are equal to H_F and H_I, respectively.

Eq. (2.2) can be used with either isothermal magnetization curves measured at different temperatures or temperature dependent magnetization curves measured at different applied fields, though the latter is less time-consuming than the former (it is faster to stabilize the magnetic field than the temperature). For SOPT MC materials, both ways can be applied without main drawbacks while for FOPT cases, their measurements should be more tedious as spikes are found when applying Eq. (2.2) to isothermal magnetization curves. This is ascribed to the coexistence of phases during the transition [108, 109]. Hence, it is relevant to account for the effects of partial transformations during each measurement by erasing the thermal and field histories to obtain

experimental data with physical meaning [110]. In this thesis, this was performed by cooling/heating the sample well below/above its transition with a simultaneous application of an appropriate value of the magnetic field (depending on the particular phase to be stabilized) prior to the measurements at each desired temperature (denoted as discontinuous protocols). Table 2.1 shows a summary of the different existing discontinuous measurements protocols accounting for heating and cooling processes for samples with transition temperatures increasing/decreasing with field ($T_{trans}/\Delta H > 0$ and $T_{trans}/\Delta H < 0$, respectively).

$T_{trans}/\Delta H > 0$ (e.g. $La(Fe,Si)_{13}$)

Cooling	Heating
Set $T >> T_{trans}$ at H_I	Set $T << T_{trans}$ at H_F
Set desired T	Set desired T
Measure $M_T(H_I \rightarrow H_F)$	Measure $M_T(H_F \rightarrow H_I)$
Repeat for other T	Repeat for other T

$T_{trans}/\Delta H < 0$ (e.g. Ni-Mn-In Heusler alloys)

Cooling	Heating
Set $T >> T_{trans}$ at H_F	Set $T << T_{trans}$ at H_I
Set desired T	Set desired T
Measure $M_T(H_F \rightarrow H_I)$	Measure $M_T(H_I \rightarrow H_F)$
Repeat for other T	Repeat for other T

Table 2.1: Summary of the different discontinuous measurement protocols assuming that $H_F > H_I$.

2.6 Relaxation calorimetry

A relaxation calorimeter measures the heat capacity of a sample by controlling the heat while monitoring the resulting change in temperature. The used system consists of a sample platform, in which a heater and a thermometer are attached to its bottom part. Both are electrically connected by four small wires, which also provide the thermal connection and structural support for the platform. Typically, the sample (mass

around 1-100 mg) is mounted to the platform using a thin layer of grease (Apiezon N) to ensure a good thermal contact between the sample and the platform. A thermodynamic analysis for the setup leads to a system of two equations with many variables apart from the heat capacity of the sample, for example the heat capacity of the platform and the thermal conductivities of the wires and grease. Some of the parameters can be determined from the addenda measurements such as the heat capacity of the platform. If it is assumed that the heat capacity is kept constant during the heat pulse, it can be obtained (among the rest of parameters as e.g. thermal conductivity of the wires) from the fitting of the temperature evolution to the solution of the two-tau model [111]. For SOPT, the approximation can be applied with good results. In the case of a FOPT, that assumption is not true in the region close to the transition temperature, as a divergence in the heat capacity appears. For this case, fitting procedures cannot be applied, the equation system has to be solved point by point, and in this case, the parameters have to be previously determined. The different assumptions used for determining the different parameters can drastically affect the measurements [112, 113].

Heat capacity measurements by the relaxation method were performed using the heat capacity option of a commercial Quantum Design Physical Property Measurement System.

2.7 Direct adiabatic temperature change measurement

Direct ΔT_S measurements were performed using a modified MagEq MMS 902 manufactured by AMT&C Corporation. The sample holder was maintained in vacuum during measurements and samples were thermally isolated to ensure good adiabatic conditions. The magnetic field generator is composed of two concentric Hallbach cylinders, which produce a maximum magnetic field of 1.76 T. The temperature change of the sample

produced by the application/removal of a magnetic field was registered by a Type T thermocouple (with its reference located in the sample holder), while the temperature of the sample holder was controlled by a LakeShore temperature controller. The various measurement protocols on erasing the sample's prior history were automated using our in-house implemented software with appropriate PID parameters for the temperature controller (to avoid thermal oscillations around a certain temperature). Fig. 2.1 illustrates both continuous (without accounting for the sample's history) and discontinuous measurement protocols.

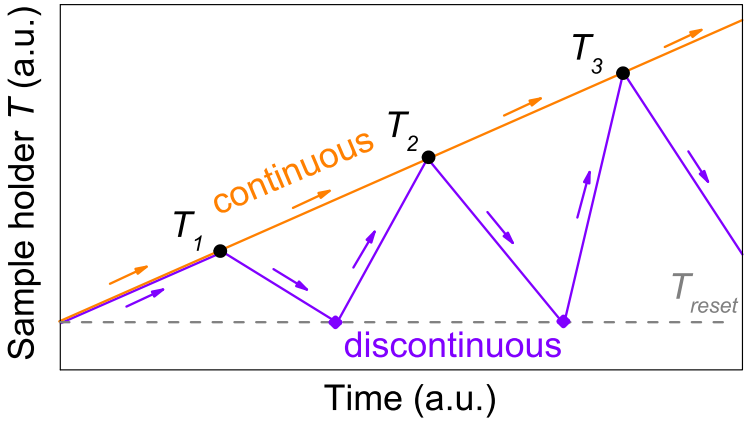

Figure 2.1: Time dependence of the sample holder temperature illustrating continuous and discontinuous measurement protocols.

3 Influence of experimental factors on the magnetocaloric effect

The influence of different experimental factors on the MC response will be covered in this chapter. Both experimental measurements and numerical calculations were used. For macroscopic and microscopic characteristics, the effects of sample geometry and compositional inhomogeneities on Δs_T and its field dependence exponent were analyzed. For calculating the MC magnitudes from heat capacity measurements, the influence of the low temperature limitation on the MC responses was studied. Finally, the influence of continuous and discontinuous protocols on direct ΔT_S measurements was discussed.

3.1 Sample geometry

When performing magnetic measurements of a magnetic material, the sample geometry has to be considered to determine the internal magnetic field [114]. This is because the magnetized sample generates magnetic poles at its edges which then create a magnetic field (called demagnetizing field (H_D)) that opposes magnetization. Hence, the magnetic field within the material under an applied magnetic field (H_{app}) is expressed as:

$$H = H_{app} + H_D. \tag{3.1}$$

For ellipsoidal geometries where M is uniform, H_D and M are related through the demagnetizing factor (N_D) as:

$$H_D = -N_D M, \tag{3.2}$$

where the negative sign indicates that H_D has an opposite direction to M (N_D is defined with positive sign). This implies that the internal field is smaller than the one applied. Table 3.1 shows different demagnetizing factors of some typical geometries for certain directions (which can be approximated to the sample geometries studied in this thesis). Generally, the demagnetizing factor is a tensor magnitude (as it relates two vector magnitudes) with unit trace. To obtain the approximate values of the internal field, even for non-ellipsoidal geometries (cylinders, squares...), an effective demagnetizing factor can be used.

Sample geometry	Direction	N_D
Needle	Along the long axis	0
	Perpendicular to the long axis	1/2
Sphere	Any direction	1/3
Thin film	In plane	0
	Perpendicular to the plane	1

Table 3.1: N_D of typical ideal sample geometries magnetized along certain directions.

For the isothermal magnetic entropy change from magnetization measurements, the demagnetizing factor has to be considered in order to properly calculate Eq. (1.16) [115–117]. For experimental validation, an example of SOPT MC material was selected, whose analysis will be more straightforward than those for FOPT cases. Besides typical SOPT MC material, Gd, amorphous magnetic alloys are well-studied for MC effect. In addition, their negligible magnetocrystalline anisotropy make them an ideal candidate to study the shape anisotropy. For that, amorphous $Co_{62}Nb_6Zr_2B_{30}$ materials (known for their excellent soft magnetic behavior [118,119]) were used for investigating the effects of N_D on their MC responses [120]. They were synthetized using two alternatives techniques: rapid quenching (RQ) and mechanical alloying (MA) [121]. More information on their preparation can be found in Refs. [122,123].

These two ways of amorphizing the same composition had been reported with differences in their macroscopic and microscopic structures [121]. Macroscopically, MA leads to powder samples while RQ techniques produce micron-thick ribbons or wires. To perform magnetic measurements, the ribbon can be mounted with the applied field contained in its plane, to present a negligible demagnetizing factor ($N_D \approx 0$) while this is not possible for powder samples, for which the effect of demagnetizing field is unavoidable. For preparing the samples for magnetic characterization, the MA powders (whose geometries are close to spheres) were encapsulated in an Ag capsule, while the ribbons were cut into disks.

Fig. 3.1 shows, as solid symbols, the temperature dependence of Δs_T (A) and exponent n (B) for RQ and MA $Co_{62}Nb_6Zr_2B_{30}$ considering the applied magnetic field change for 1 T. Δs_T magnitude was indirectly determined from magnetization curves according to Eq. (1.16) while the field dependence exponent n was obtained from the calculated Δs_T data according to Eq. (1.37). Despite that the samples have the same nominal composition, a clear difference in T_C for RQ and MA $Co_{62}Nb_6Zr_2B_{30}$ can be observed (RQ alloy exhibits lower T_C than that of MA). This is ascribed to a better homogenization of boron in RQ $Co_{62}Nb_6Zr_2B_{30}$ [122].

Apart from this, exponent n of the MA $Co_{62}Nb_6Zr_2B_{30}$ determined when considering the applied magnetic field (solid symbols) shows values deviating from $n = 1$ for $T << T_C$ in the ferromagnetic region, which is in contrast with the theoretical predictions (for a pure ferromagnetic material, independent of the composition and magnetic field, n should be 1 for $T << T_C$ and not exceed it) [92].

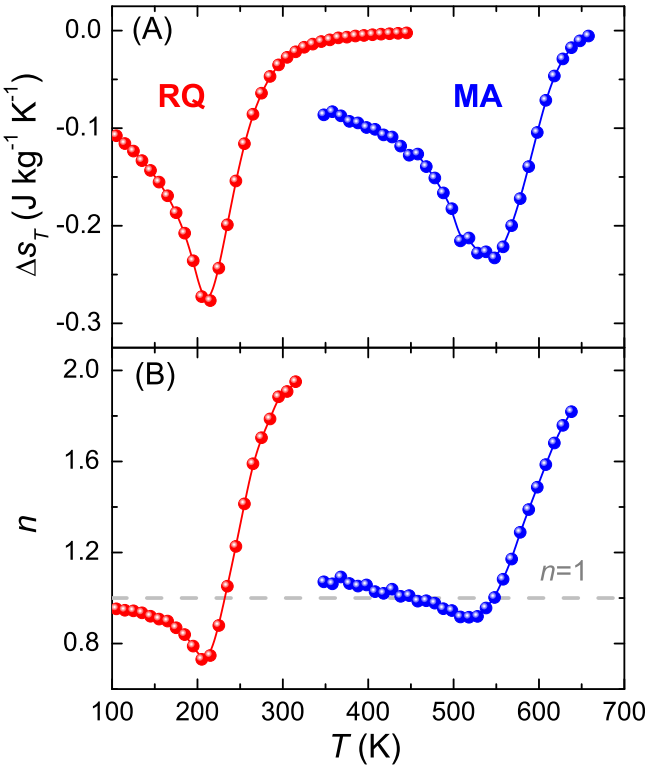

Figure 3.1: Temperature dependence of Δs_T (A) and exponent n (B) for both RQ and MA $Co_{62}Nb_6Zr_2B_{30}$ considering the applied magnetic field change for 1 T.

From the way of preparing the samples for characterization, N_D for RQ ribbon can be assumed to be $N_D \approx 0$, while $N_D \approx 1/3$ for MA powder. Using these N_D values, the internal field can be determined and was used for calculating Δs_T. These results are presented in Fig. 3.2.

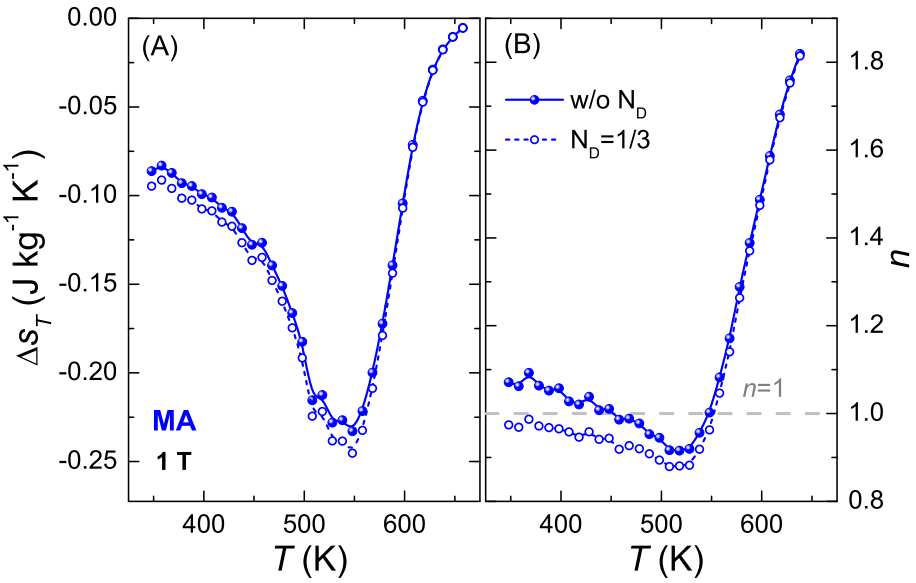

Figure 3.2: Temperature dependence of Δs_T (A) and exponent n (B) for MA $Co_{62}Nb_6Zr_2B_{30}$ considering the applied (solids symbols) or internal magnetic field change (using $N_D = 1/3$, hollow symbols) for 1 T.

It can be observed that there is no significant effect on the $\Delta s_T(T)$ curves ($\sim$ 5% reduction in magnitude when determined using the internal field) but it eliminates the earlier observed deviations of n at $T << T_C$, showing the typical field independent behavior predicted by the theory. It has to be noted that in the paramagnetic range, the influence of the demagnetizing factor is negligible (magnetization values are smaller). The corresponding values of $n = 2$ (as predicted by the theory) are achieved, either using the internal or the applied field (though Fig. 3.1 does not further show the temperature range to observe that n saturates at 2). For expressing the magnetic field dependence, one should note that the magnetic field corresponds to internal field when N_D is being used, while it is the applied field if N_D is not considered.

Fig. 3.3 shows the field dependence of the exponent n at temperatures well below the transition (ferromagnetic region) using the internal (i.e. considering the effect of N_D) and the applied fields.

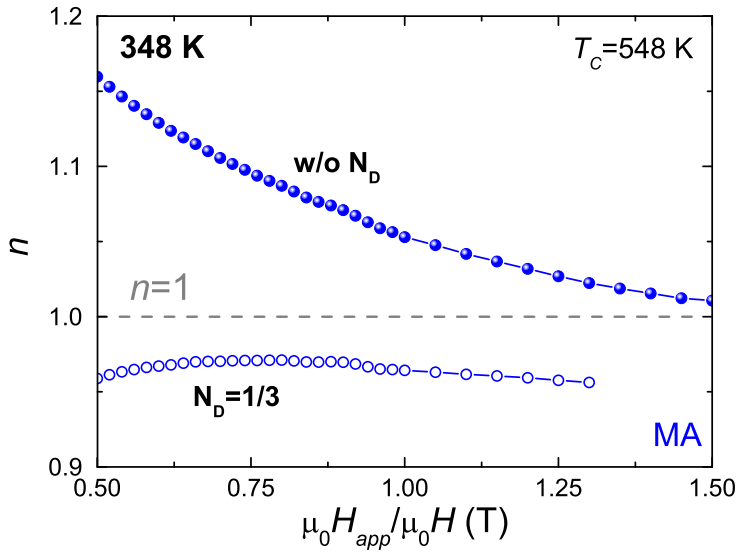

Figure 3.3: Ferromagnetic region of field dependence of the exponent n for MA $Co_{62}Nb_6Zr_2B_{30}$ using applied (solid symbols) and internal fields ($N_D = 1/3$, hollow symbols).

The influence of demagnetizing factor on the field dependence exponent n is more evident with decreasing fields within the ferromagnetic region. Represented by the solid symbols, exponent n determined without using N_D deviates from theoretical predictions $n = 1$, which has been experimentally well-validated in literature [90, 124]. On the other hand, when recalculating the data with N_D, these deviations are not observed (hollow symbols). Moreover, it can be observed that the n values of applied field tend to wards those of the internal field. This is due to the fact that the effect of the demagnetizing field is smaller as we approach saturation (as the applied field increases).

According to the scaling laws, it has been demonstrated that RCP can be expressed as a power law in the form $RCP \propto \Delta H^r$, being r as a function of different critical exponents (Table 1.1). Fig. 3.4 shows the field dependence of the exponent r calculated for RQ and MA $Co_{62}Nb_6Zr_2B_{30}$, whereby the latter was further used to studying the role of N_D.

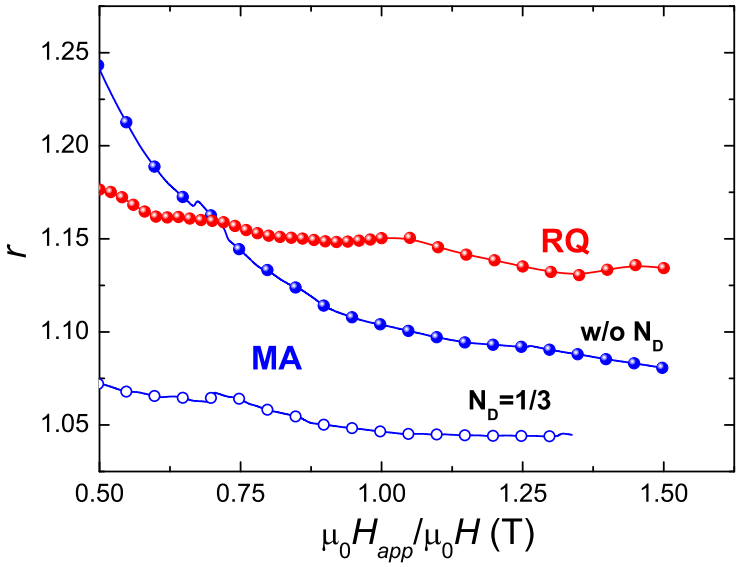

Figure 3.4: Field dependence of the exponent r for RQ and MA $Co_{62}Nb_6Zr_2B_{30}$ using applied (solid symbols) and internal fields (N_D=1/3, hollow symbols).

A strong deviation of the field dependence of the exponent r can be observed for MA $Co_{62}Nb_6Zr_2B_{30}$, especially at small fields, when not considering the internal field (solid blue symbols), which deviates from the theoretical predictions (r should be field independent, since it depends on the critical exponents of the transition). However, this artificial field dependence is also corrected (as it occurs for the exponent n) if the demagnetizing factor is considered, recovering the field independence of exponent r (blue hollow symbols). This field independent behavior can be also observed for RQ $Co_{62}Nb_6Zr_2B_{30}$, for which $N_D \sim 0$ is assumed. Deviations ($< 5\%$) from the field independence can be due to slight deviations from the assumed N_D values.

Numerical calculations were further investigated to analyze the influence of N_D on MC calculations. The A-N EOS has been used for obtaining σ as a function of H and T. Typical parameters for amorphous alloys were used ($a = 1$ $(10^{-4}$ T$)^{1/\gamma}$ (A m^2 kg$^{-1})^{-1/\gamma}$ K^{-1}, $b = 0.01$ $(10^{-4}$ T$)^{1/\gamma}$

(A m^2 kg^{-1})$^{-(1/\beta+1/\gamma)}$). After the $\sigma(H,T)$ simulated data were generated, the applied field was calculated using Eqs. (3.1) and (3.2), and $\sigma(H_{app},T)$ were then obtained. Using both sets of simulated magnetization data, numerically calculated Δs_T from Eq. (1.16) and exponent n according to Eq. (1.37) were obtained. Fig. 3.5 shows the calculated temperature dependence for Δs_T and exponent n for different magnetic fields (either applied or internal). It can be observed that Fig. 3.5 reproduces the main features observed from experimental results [125].

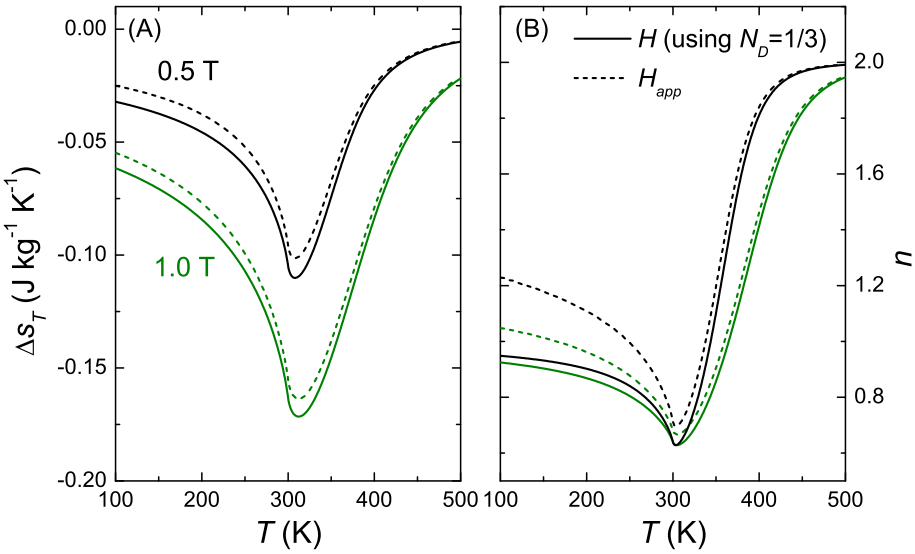

Figure 3.5: Numerical simulated temperature dependence of Δs_T (A) and exponent n (B) for 0.5 and 1.0 T of applied (dashed line) or internal field (using $N_D = 1/3$, solid line).

Numerical Δs_T calculated using the internal field shows an underestimation of approximately 5-10 % at the peak values (differences in the paramagnetic region are negligible, while those for the ferromagnetic range are considerable). For exponent n, it can be observed that unreal field dependences for temperatures well below T_C and at T_C are observed when neglecting the demagnetizing field (while these dependences are not observed in the case of considering the internal field). As previously

mentioned, these unreal field dependences can lead to erroneous values of the critical exponents when determined from the MC data (as well as when any other method is used). In addition, the effect of the demagnetizing field decreases with increasing applied magnetic field.

According to these results, the determination of the MC response in the later chapters of the thesis was done using a Matlab software that was programmed to account for the effect of N_D.

3.2 Compositional inhomogeneities

It can be quite common to find trace amounts of compositional inhomogeneities in alloys which affect the MC response [126, 127]. They can result in a T_C distribution [128, 129] or distributed phase difference [130]. Using experimental SOPT MC materials as the case study, this section describes the influence of a T_C distribution on Δs_T and its field dependence exponent n [120].

$Co_{62}Nb_6Zr_2B_{30}$ amorphous alloy, the previous case study, was found to exhibit distributed T_C when they were amorphized by MA. The alloying process began from elemental precursors and boron is not well incorporated into the amorphous matrix of the MA $Co_{62}Nb_6Zr_2B_{30}$, resulting in a T_C distribution of the amorphous phase. On the other hand, RQ ribbons prepared with the proper quenching rate are amorphous with relatively uniform composition throughout. Furthermore, it is known that higher contents of compositional inhomogenities and structural defects are found in amorphous alloys when prepared by MA than those by RQ [131]. The differences of MA and RQ $Co_{62}Nb_6Zr_2B_{30}$ can be observed from their MC results as shown in the upper panel of Fig. 3.1. The temperature dependence of Δs_T of MA $Co_{62}Nb_6Zr_2B_{30}$ amorphous alloy shows a smaller peak magnitude and larger temperature width compared to those of RQ alloys (all determinations were upon N_D consideration).

For the exponent n values at the peak temperatures, those values of MA $Co_{62}Nb_6Zr_2B_{30}$ are clearly larger than those found for RQ counterpart (after taking into account the demagnetizing factor, as observed in Fig. 3.1). This arises, despite both samples are of the same nominal composition, due to the limited incorporation of boron into the amorphous matrix of the MA alloy, leading to a distribution of T_C in the amorphous phase. On the other hand, the RQ ribbons are homogeneous in composition distributed throughout. Particularly, for CoB amorphous alloys, T_C is very sensitive to changes in B content, decreasing at ≈ 30 K (at.% B)$^{-1}$ [132].

To study numerically the effect of a distribution of Curie temperatures on the MC response, a sum of individual Δs_T curves (with a certain Curie temperature) following a Gaussian distribution was considered as a first approximation. Therefore, the total contribution can be expressed as:

$$\Delta s_T(T, \Delta H, \overline{T_C}, \omega) = \kappa \sum_{\overline{T_C}-\Omega}^{\overline{T_C}+\Omega} \Delta s_T(T, \Delta H, T_C) \exp\left(-(T_C - \overline{T_C})^2/2\omega^2\right), \tag{3.3}$$

where ω is the standard deviation of the distribution, 2Ω is the range of the distribution, $\overline{T_C}$ is the mean Curie temperature and κ is a normalization constant obeying:

$$\kappa \sum_{\overline{T_C}-\Omega}^{\overline{T_C}+\Omega} \exp\left(-(T_C - \overline{T_C})^2/2\omega^2\right) = 1. \tag{3.4}$$

For the simulated MC studies of MA $Co_{62}Nb_6Zr_2B_{30}$ with a Gaussian distribution of T_C, their critical exponents were adopted from those determined for RQ ribbons ($\beta = 0.415(1)$ and $\gamma = 1.50(1)$) using the K-F method, as depicted in Fig. 3.6. The values of $a = 2.32(1)$ $(10^{-4}$ T$)^{1/\gamma}$ (A m^2 kg^{-1})$^{-1/\gamma}$ K^{-1} and $b = 0.0635(3)$ $(10^{-4}$ T$)^{1/\gamma}$(A m^2 kg^{-1})$^{-(1/\beta+1/\gamma)}$ were obtained following the 3D-fitting proposed in [87]. For RQ ribbons, T_C distribution is assumed negligible, which is further

supported by the good fitting of the experimental data using the A-N EOS, as observed in the inset of Fig. 3.6.

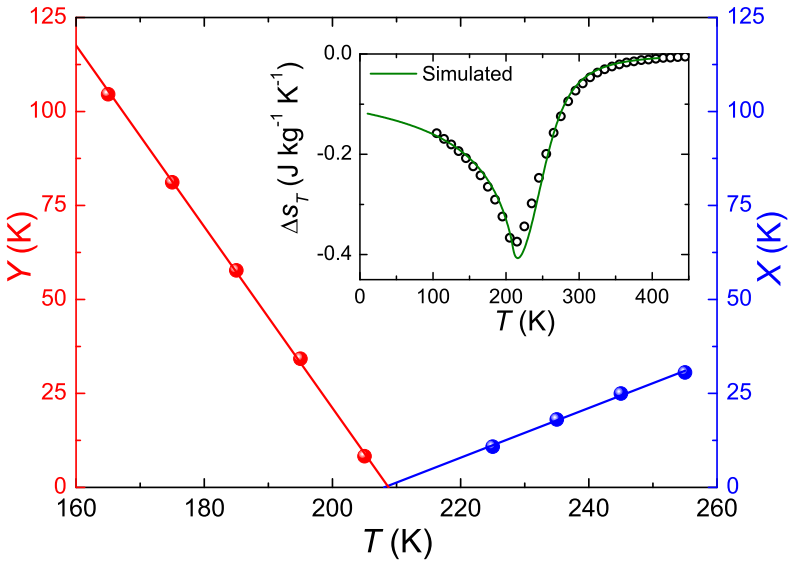

Figure 3.6: K-F plot to obtain the critical exponents of RQ $Co_{62}Nb_6Zr_2B_{30}$. Inset: experimental and simulated Δs_T (for 1.5 T) using the A-N EOS with the fitted parameters.

The Δs_T curve was generated following a Gaussian weight according to the separation of T_C with respect to the mean value $\overline{T_C}$. To illustrate the procedure, the Gaussian distribution of T_C proposed in Eq. (3.3), using single-T_C curves, is presented in Fig. 3.7, where various simulated curves are presented for comparing the differences among the curves. Additionally, to simulate Eq. (3.3), a small T_C step of sufficient resolution was selected to obtain results that are independent of this parameter.

In addition, various standard deviation values of T_C distribution were considered for the simulation of Δs_T curves and are presented in Fig. 3.8. On top of the expected increase in the temperature width and the reduction of the Δs_T^{pk} magnitude, a slight decrease of $T_{pk}^{\Delta s_T}$ is observed. This is due to the asymmetric shapes of Δs_T curves (presenting higher values in the ferromagnetic range than in the paramagnetic one).

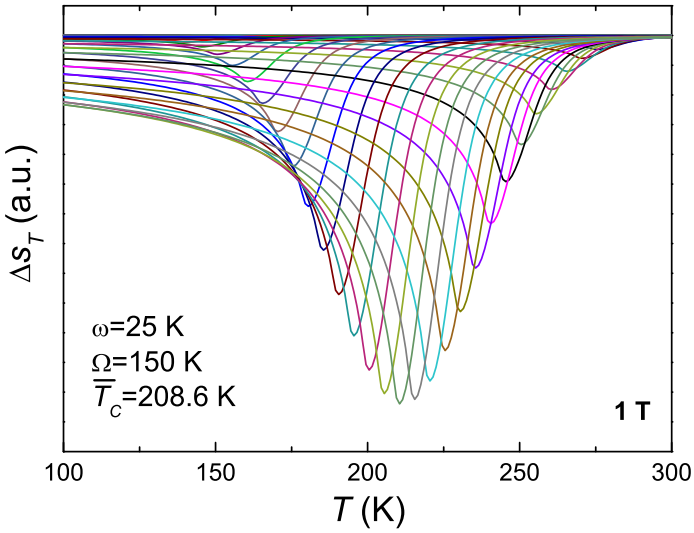

Figure 3.7: Simulated ΔS_T curves weighted according to a Gaussian distribution for different T_C values.

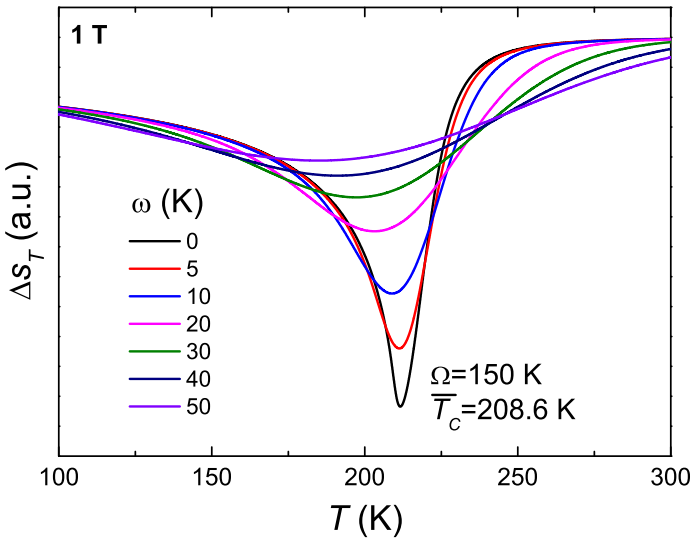

Figure 3.8: Δs_T generated for different standard deviation values of a Gaussian distribution of T_C.

Using A-N EOS, the MC behavior of MA alloys with distributed T_C was simulated. This EOS allows to accurate fit experimental data in a

temperature range of 100 K near T_C for amorphous alloys with T_C close to room temperature [87]. Thus, for our studies, the Gaussian range was limited to $\Omega = 150$ K, accounting for the previous-mentioned limitation. Contributions near the limit of the range must be assumed negligible to minimize the effect of a finite Gaussian range, which limits the ω range for exploration. For that, simulated ω dependence of $n(T_{pk}^{\Delta s_T})$ for different Ω values shows a saturated deviation of $n(T_{pk}^{\Delta s_T})$ for $\omega > \Omega/2.5$ (compared to the typical $n(T_{pk}^{\Delta s_T})$ vs. ω curve). Therefore, the reliable simulated values of $n(T_{pk}^{\Delta s_T})$ were limited to $\omega \leq 60$ K for our studies.

In addition, field dependence exponent n was determined from the MC simulations for different standard deviations of the Gaussian T_C distribution. Fig. 3.9 shows the experimental and simulated $n(T)$ for both MA and RQ alloys in its main panel.

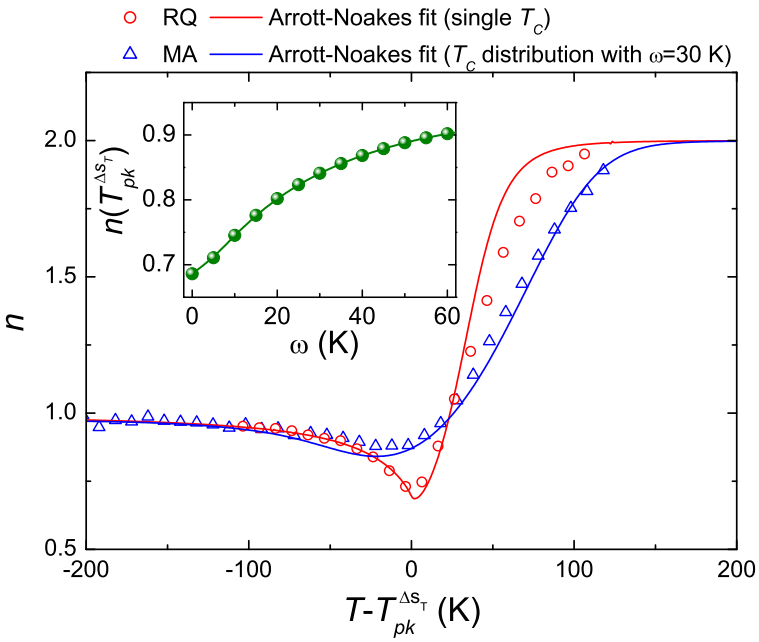

Figure 3.9: Experimental and simulated $n(T)$ curves for MA and RQ $Co_{62}Nb_6Zr_2B_{30}$. Inset: ω-dependence of $n(T_{pk}^{\Delta s_T})$ for the simulated Gaussian distribution of T_C.

As a T_C shift with respect to RQ ribbons results from poor B incorporation in the amorphous phase, a rescaled temperature axis was used for comparing the behaviors of MA and RQ samples. The ω-dependence of $n(T_{pk}^{\Delta s_T})$ is plotted in the inset of Fig. 3.9, wherein $n(T_{pk}^{\Delta s_T})$ increases with the standard deviations. A maximum ω value of approximately 60 K is used. Hence, the simulated $n(T)$ of MA $Co_{62}Nb_6Zr_2B_{30}$ was based on the assumption of a Gaussian Curie temperature distribution with $\omega = 30$ K, which exhibits the best agreement among our analysis. This value of ω can be related with an approximate 1 at.% B variation. Moreover, the simulated curves reproduce the main features of the experimental data with fairly good agreement: a larger $n(T_{pk}^{\Delta s_T})$ value and sharper bend towards the paramagnetic region were observed for RQ ribbons than those for MA powder (due to the distributed T_C). Additionally, it is also reproduced that the minimum of $n(T)$ shifts to temperatures below the mean value of T_C in the presence of a distribution of T_C.

3.3 Low-temperature limitation of calorimetric measurements

For the MC determination using heat capacity measurements, first of all, the total entropy of the system has to be calculated according to Eq. (1.21). This requires the knowledge of the zero entropy term and the heat capacity measurements to be extended down to 0 K (to perform the integration). On the one hand, the zero entropy term can be assumed small in a condensed system and field independent [133], having a negligible influence on the total entropy. On the other hand, as temperatures close to 0 K cannot be reached, the calculus of the integral can be considerably affected. This can be ascribed to the limitations of the experimental setup (e.g. liquid N_2 is used as the coolant) or to the difficulties in measuring the specific heat for a large temperature range (e.g. limited stability in the grease that is typically used for sample mounting to the calorimetric chip). For such cases, some assumptions must be made for the missing

data range. The most commonly used approximation is to assume a linear behavior of c_H/T down to 0 K and, therefore, an approximate expression for the entropy is proposed [29]:

$$s_H^{ap}(T) = \frac{1}{2}c_H(T_{ini}) + \int_{T_{ini}}^{T} \frac{c_H}{T}\mathrm{d}T, \tag{3.5}$$

where T_{ini} is the lowest achievable temperature in c_H measurements. According to this, the approximated values for both MC magnitudes (Δs_T^{ap} and ΔT_S^{ap}) can be calculated from Eq. (3.5) using Eqs. (1.5) and (1.3).

In this section, the influence of this linear c_H/T assumption (from T_{ini} down to 0 K) on the MC response is discussed [134–136]. For that, numerical calculations for single phase and multiphasic MC materials were performed. Their results were also further corroborated by experimental work using paradigmatic SOPT and FOPT MC materials: Gd and $Gd_5Si_2Ge_2$, respectively [134].

To numerically reproduce a single phase MC material, firstly the total heat capacity of the system is considered as the sum of the magnetic, lattice and electronic contributions:

$$C = C_L + C_E + C_M, \tag{3.6}$$

where C_L, C_E and C_M are the heat capacity contributions of the lattice, electronic and magnetic subsystems, respectively. For the lattice and electronic contributions, the Debye and Fermi models have been used, respectively [137]. For the magnetic contribution, the B-R model was used to describe both FOPT and SOPT MC materials [98]. The different heat capacity contributions are calculated as:

$$C_L = 9N_p k_B \left(\frac{T}{\Theta_D}\right) \int_0^{\Theta_D/T} \frac{z^4 e^z}{(e^z-1)^2}\mathrm{d}z, \tag{3.7}$$

$$C_E \approx \tau T, \tag{3.8}$$

$$C_M = N_m K_B T \left(\partial \left(\ln \frac{\sinh\left(\frac{2J+1}{2J}\varpi\right)}{\sinh\left(\frac{1}{2J}\varpi\right)} - \varpi \mathcal{B}(\varpi) \right) / \partial T \right)_H , \tag{3.9}$$

where N_p is the number of particles, Θ_D is the Debye temperature, τ is a constant and ϖ was defined as (Section 1.4.4):

$$\varpi = \frac{\mu_0 g \mu_B J}{k_B T} \left(H + \lambda^{(1)} M + \lambda^{(3)} M^3 \right). \tag{3.10}$$

Gd parameters were used for the simulations ($T_C = 293$ K, $g = 2$, $J = 7/2$, $\Theta_D = 163$ K, $\tau = 6.4$ mJ mol^{-1} K^{-2}).

The simulated specific heat for different magnetic fields for both SOPT ($\eta = 0$) and FOPT ($\eta = 1.5$) MC materials are shown in Fig. 3.10.

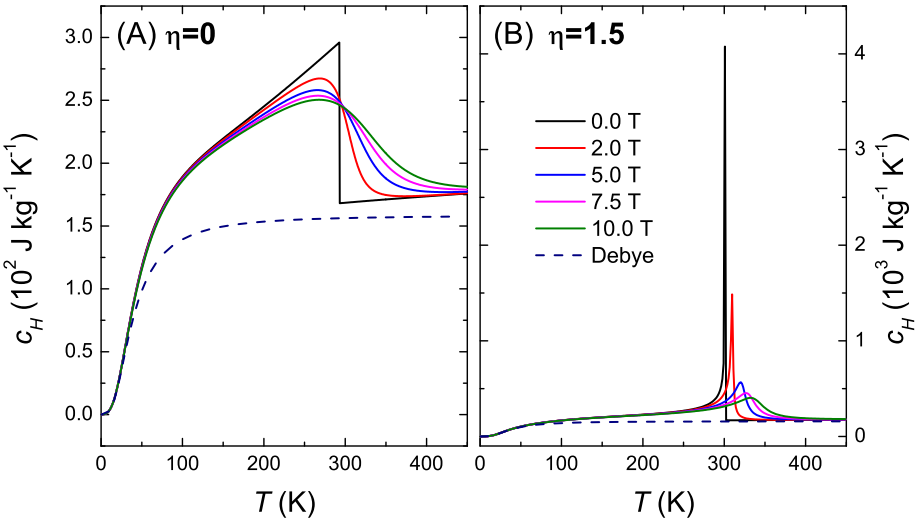

Figure 3.10: Temperature dependence of calculated specific heat for different magnetic fields for $\eta = 0$ (SOPT) (A) and 1.5 (FOPT) (B). Lattice contributions are plotted as dashed lines.

Only the lattice contribution is plotted separately (dashed line) as the electronic contribution is of too low values to be plotted. It can be observed that the main features of the specific heat for both SOPT and FOPT MC materials are reproduced using the described models: a divergence and a

discontinuity close to T_{trans} are obtained for FOPT and SOPT, respetively. Using these data, the total entropy was calculated according to Eq. 3.5, where the data were truncated from different initial temperatures. With the obtained approximated entropy curves, the MC magnitudes were calculated using Eqs. (1.3) and (1.5).

For SOPT MC material, its simulated temperature dependence of Δs_T^{ap} for 2 T for various initial temperatures using $\eta = 0$ is plotted in Fig. 3.11. It is observed that each curve differs from that integrated from 0 K (this is used as the reference) although the shape is preserved. The deviations follow a non-monotonous trend with increasing T_{ini} (e.g. the curve starting from 125 K has a larger deviation than those starting at 75 and 200 K). To quantify this, the differences of the peak values between each Δs_T^{ap} curve ($\Delta s_T^{ap,pk}$) and that of the reference as a function of T_{ini} are plotted in the inset of Fig. 3.11. For simplicity, these differences (used either for Δs_T or ΔT_S) are denoted as Φ from now.

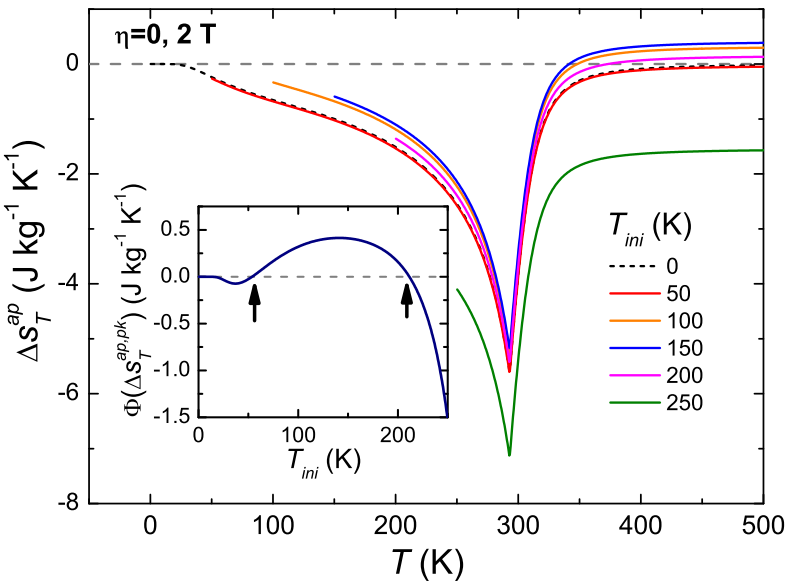

Figure 3.11: Numerical temperature dependence of Δs_T^{ap} for 2 T and different T_{ini} using $\eta = 0$. Inset: Φ differences of $\Delta s_T^{ap,pk}$ as a function of T_{ini}. T_{ini}^{opt} values are marked with arrows.

There are three cases showing zero Φ difference. Besides a flat region close to 0 K, there are two values of the initial temperature for which the Δs_T^{ap} values coincide with those of the complete curve (marked with arrows in the inset of Fig. 3.11). These marked T_{ini} values are denoted as optimal initial temperatures (T_{ini}^{opt}). For practical purposes, the most useful T_{ini}^{opt} would be the highest, to have an experimental temperature range as narrow as possible. Hence, the largest T_{ini}^{opt} was further used for the remaining studies.

Considering the expression in Eq. (3.5), the approximated entropy can be related with the entropy starting from 0 K as:

$$s_H = \int_0^T \frac{s_H}{T}\mathrm{d}T = s_H^{ap} - \frac{1}{2}c_H(T_{ini}) + \int_0^{T_{ini}} \frac{c_H}{T}\mathrm{d}T = s_H^{ap} + \xi_H(T_{ini}), \quad (3.11)$$

where $\xi = -\frac{1}{2}c_H(T_{ini}) + \int_0^{T_{ini}} \frac{c_H}{T}\mathrm{d}T$ depends on T_{ini} and H. With this relation, the deviations of Δs_T^{ap} from Δs_T can be discussed. For a zero initial magnetic field, Δs_T becomes:

$$\begin{aligned} \Delta s_T(T,H) &= s_H(T) - s_0(T) \\ &= s_H^{ap}(T) + \xi_H(T_{ini}) - (s_0^{ap}(T) + \xi_0(T_{ini})) \\ &= \Delta s_T^{ap}(T,H) + (\xi_H(T_{ini}) - \xi_0(T_{ini})), \end{aligned} \quad (3.12)$$

where it can be observed that $\Phi(\Delta s_T^{ap})$ is:

$$\xi_H(T_{ini}) - \xi_0(T_{ini}). \quad (3.13)$$

It should be noted that this term is temperature independent. T_{ini}^{opt} corresponds to the temperatures that fulfill $\xi_H(T_{ini}) = \xi_0(T_{ini})$. Fig. 3.12 shows the temperature dependence of $\Phi(\Delta s_T^{ap})$ for different T_{ini}. It can be observed that the differences are 0 for T_{ini}^{opt}.

A similar analysis was performed for ΔT_S. Fig. 3.13 shows the simulated temperature dependence of ΔT_S^{ap} for different values of T_{ini} in the main panel and $\Phi(\Delta T_S^{ap,pk})$ as a function of T_{ini} in the inset.

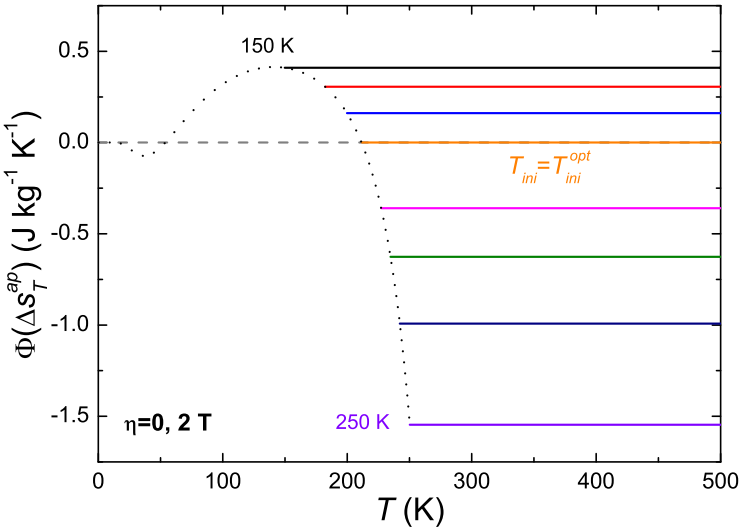

Figure 3.12: Temperature dependence of $\Phi(\Delta s_T^{ap})$ for different initial temperatures. The dashed line represents this difference as a function of T_{ini} in a continuous curve.

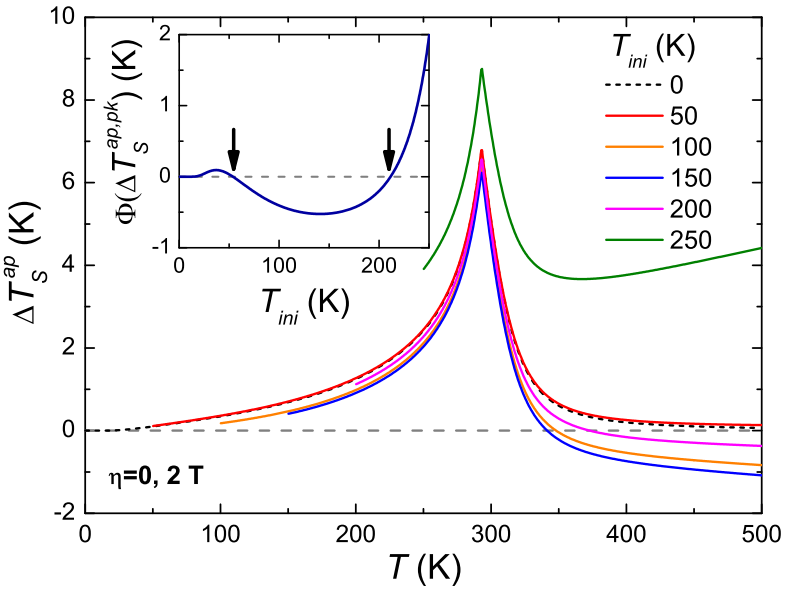

Figure 3.13: Numerical temperature dependence of ΔT_S^{ap} for 2 T and different T_{ini} using $\eta = 0$. Inset: Φ differences of $\Delta T_S^{ap,pk}$ as a function of T_{ini}. T_{ini}^{opt} values are marked with arrows.

It is observed that the different T_{ini} values give ΔT_S^{ap} curves of different peak values and shapes (specially in the high temperature region). As for the difference of each curve to the reference (integrated from 0 K), two T_{ini} with zero difference are observed and marked by the arrows. These observations are similar to those found for delta Δs_T^{ap}. Furthermore, the values obtained for the optimal T_{ini}^{opt} are the same as those found for Δs_T^{ap}.

For ΔT_S, the observed deviations were further analyzed. Assuming a certain temperature T^* and defining $s^* = s_0(T^*)$ and $s^{ap,*} = s_0^{ap}(T^*)$, the expressions for ΔT_S and ΔT_S^{ap} are:

$$\Delta T_S(T^*, H) = T_H(s^*) - T_0(s^*) \tag{3.14}$$

and

$$\Delta T_S^{ap}(T^*, H) = T_H^{ap}(s^{ap,*}) - T_0^{ap}(s^{ap,*}), \tag{3.15}$$

respectively. The relation between s^* and $s^{ap,*}$, according to Eq. (3.11), is:

$$s^{ap,*} = s^* - \xi_0. \tag{3.16}$$

According to Eq. (3.5), the approximated and integrated from 0 K temperature functions for any magnetic field are related by:

$$T_H^{ap}(s^{ap} = s_H - \xi_H) = T_H(s_H). \tag{3.17}$$

Incorporating Eq. (3.16) into Eq. (3.14):

$$\Delta T_S(T^*) = T_H(s^{ap,*} + \xi_0) - T_0(s^{ap,*} + \xi_0), \tag{3.18}$$

that when introducing Eq. (3.17) it gives:

$$\Delta T_S(T^*) = T_H^{ap}(s^{ap,*} + \xi_0 - \xi_H) - T_0(s^{ap,*}). \tag{3.19}$$

Therefore, when ξ_H=ξ_0 (i.e. when $T_{ini} = T_{ini}^{opt}$), Eq. (3.19) becomes:

$$\Delta T_S(T^*) = \Delta T_S^{ap}(T^*). \tag{3.20}$$

The same condition is also obtained for Δs_T, demonstrating that the optimal initial temperatures are the same for both MC magnitudes. It should be noted that Δs_T^{ap} and ΔT_S^{ap} deviations show different signs, i.e. when Δs_T^{ap} is underestimated, ΔT_S^{ap} is overestimated and vice versa. Unlike for Δs_T^{ap} data, the deviations of ΔT_S^{ap} are temperature dependent. For the case of $T_{ini} \neq T_{ini}^{opt}$, T_H^{ap} can be expanded around $s^{ap,*}$ up to first order term as:

$$\Delta T_S(T^*) = T_H^{ap}(s^{ap,*}) + \left(\frac{\partial T_H^{ap}}{\partial s^{ap}}\right)_{s^{ap,*}} (\xi_0 - \xi_H) - T_0(s^{ap,*}) \cong \Delta T_S^{ap}(T^*) - \frac{T^*}{c_H(T^*)}(\xi_0 - \xi_H), \quad (3.21)$$

where it was used that for small $(\xi_0 - \xi_H)$ values:

$$\left(\frac{\partial T_H^{ap}}{\partial s^{ap}}\right)_{s^{ap,*}} = \left(\frac{\partial T_H}{\partial s}\right)_{s^{ap,*}+\xi_H} = \left(\frac{\partial T_H}{\partial s}\right)_{s^*+\xi_H-\xi_0} \cong \left(\frac{\partial T_H}{\partial s}\right)_{s^*} = \frac{T^*}{c_H(T^*)}. \quad (3.22)$$

According to this, when $T_{ini} \neq T_{ini}^{opt}$, ΔT_S^{ap} deviates with a $T/c_H(\xi_0 - \xi_H)$ trend. Fig. 3.14 shows the temperature dependence of $\Phi(\Delta T_S^{ap})$ as a function of T_{ini} which illustrates the previously discussed behavior.

The field dependence of the deviations $(\Phi(\Delta s_T^{ap,pk})/\Delta s_T^{ap,pk})$ is presented in Fig. 3.15 (the earlier discussed studies were performed for a fixed magnetic field change). It is observed that the deviation is field dependent, though T_{ini}^{opt} only shifts slightly to higher temperatures with increasing field, at a rate of 2.1 K T^{-1} for the parameters used. Selecting a single magnetic field of 1 T, the error using its T_{ini}^{opt} for other magnetic fields is relatively small, which is within the error margin of the experimental measurements (e.g. at 2 T is around 1 %). Using T_{ini} values different from T_{ini}^{opt}, larger errors can be obtained (around 8 % at the peak) and anomalous behaviors in the temperature dependencies of Δs_T^{ap} and ΔT_S^{ap} are found (especially evident in the paramagnetic range).

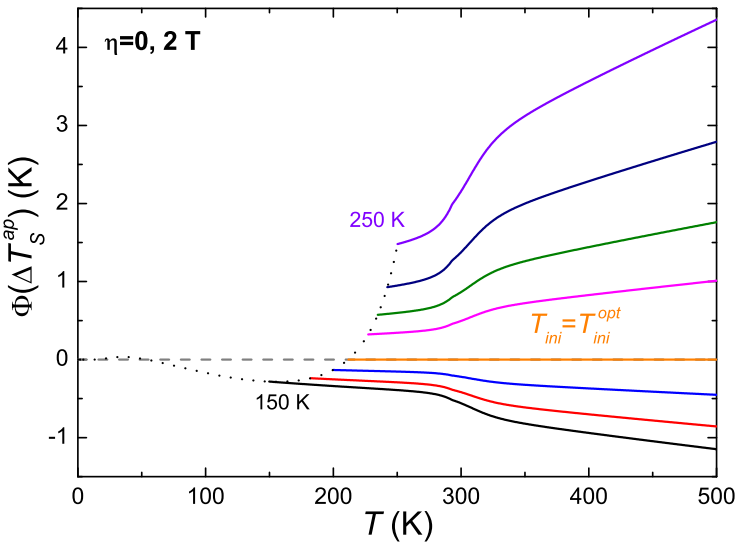

Figure 3.14: Temperature dependence of $\Phi(\Delta T_S^{ap})$ for different T_{ini}. The dashed line represents these differences as a function of T_{ini} in a continuous curve.

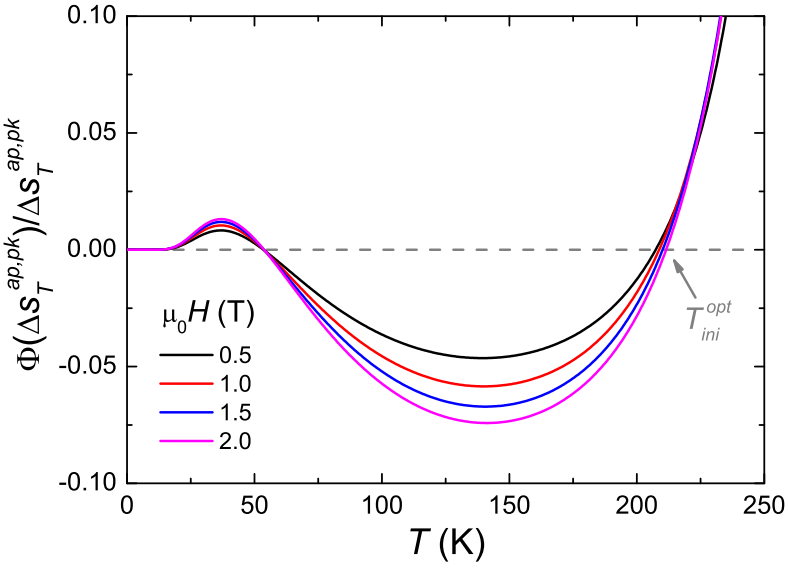

Figure 3.15: Field and temperature dependences of $\Phi(\Delta s_T^{ap,pk})/\Delta s_T^{ap,pk}$.

When different parameters of the simulations were used, it was found that T_{ini}^{opt} mainly depend on the magnetic parameters (J and T_C). Fig. 3.16 shows $\Phi(\Delta s_T^{ap,pk})$ as a function of T_{ini} for different values of J. It is worth noting that, with fixed T_C (293 K in this case) and small J values of 0.5 and 1, their Φ curves do not intercept at $\Phi(\Delta s_T^{ap,pk}) = 0$, while for higher values of J, their curves do it. However, when T_C becomes a variable while J is fixed larger than 1, T_{ini}^{opt} varies linearly with T_C as depicted in the inset of Fig. 3.16.

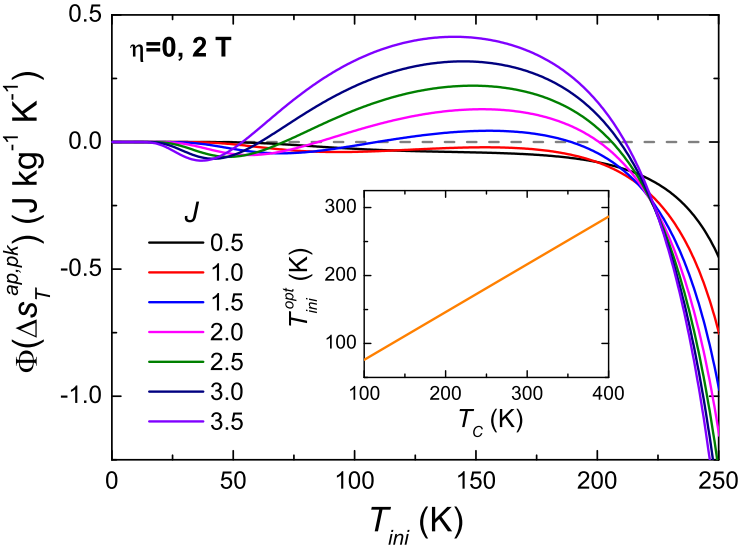

Figure 3.16: $\Phi(\Delta s_T^{ap,pk})$ differences as a function of T_{ini} for different J values ($T_C = 293$ K). Inset: T_{ini}^{opt} as a function of T_C for $J = 3.5$.

For FOPT MC materials, the η parameter should be selected above 1. Hence, Δs_T^{ap} and ΔT_S^{ap} were simulated using $\eta = 1.5$ for different T_{ini} and using $\mu_0 H = 5$ T and presented in Fig. 3.17. The insets of Fig. 3.17 show the Φ differences: for Δs_T^{ap} (A) the differences are temperature independent while for ΔT_S^{ap} (B) they are temperature dependent. It is observed that the peak of Δs_T^{ap} and ΔT_S^{ap} and the high-temperature tails of the curves deviate from those for $T_{ini} = 0$, similar to the results for the SOPT case. A sharp peak in the region close to the transition temperature

is observed for ΔT_S^{ap} as a function of T_{ini}, which is not observed for SOPT case.

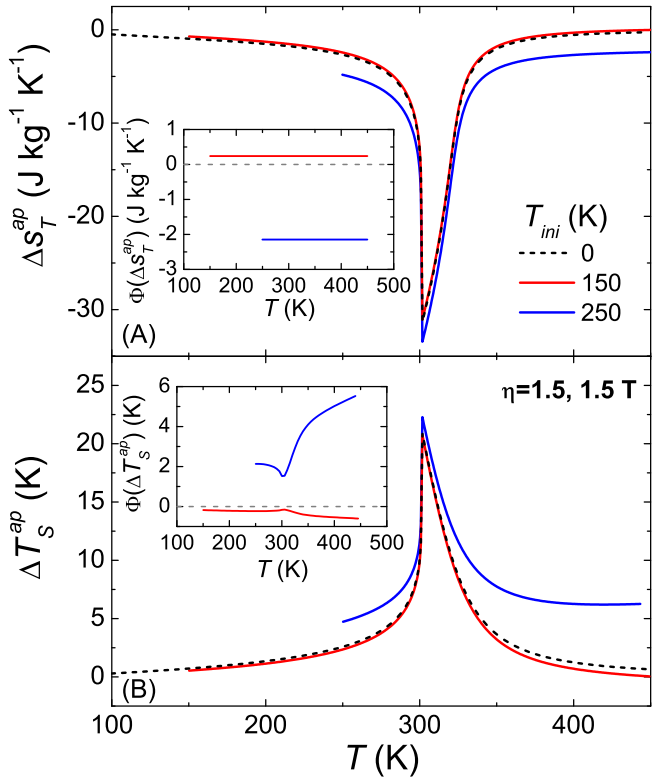

Figure 3.17: Temperature dependence of Δs_T^{ap} (A) and ΔT_S^{ap} (B) simulated using $\eta = 1.5$ for 5 T. Insets show the Φ differences of each approximated curve.

Fig. 3.18 shows the Φ differences at the peak as a function of T_{ini} for different η values. All curves exhibit similar behavior for all η values (for both SOPT and FOPT MC materials). A observed feature is that as η increases, the maximum values of Φ decrease, which implies that the approximation is less harmful for FOPT compared to SOPT. This can be attributed to their different c_H values, making the low temperature tails less important for FOPT MC materials as the values at the transition are much larger in comparison to SOPT.

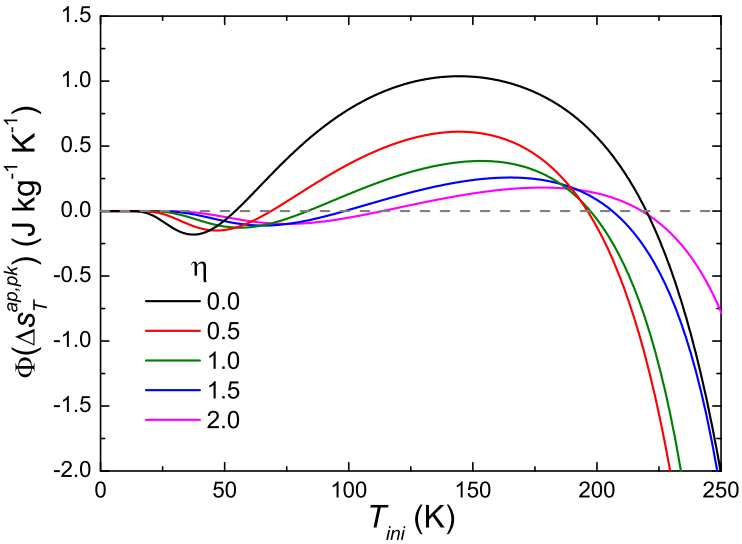

Figure 3.18: $\Phi(\Delta s_T^{ap,pk})$ as a function of T_{ini} for different η values.

Considering the temperature range well above the transition temperature (for which Δs_T and ΔT_S must be practically zero), both Δs_T^{ap} and ΔT_S^{ap} deviate from zero (either positive or negative) except for $T_{ini} = T_{ini}^{opt}$. Hence, the T_{ini}^{opt} can be experimentally identified as the temperature for which Δs_T and ΔT_S are zero at high temperatures (when $T >> T_{trans}$). Overall, the procedure proposed for evaluating Δs_T and ΔT_S when $T_{ini} \approx 0$ K cannot be attained is summarized by two simple steps: 1) First, determine the temperature dependences of Δs_T^{ap} and ΔT_S^{ap} curves for different initial temperatures of integration. 2) Next, the T_{ini}^{opt} is determined as the T_{ini} that makes $\Delta s_T^{ap} = 0$ and $\Delta T_S^{ap} = 0$ when it is well above the transition temperatures (the same optimal initial temperature for both). With T_{ini}^{opt}, the determination of Δs_T^{ap} and ΔT_S^{ap} can be considered as the best approximation (in the range $T > T_{ini}^{opt}$) for Δs_T and ΔT_S when integrated from 0 K.

Gd and $Gd_5Si_2Ge_2$ samples were selected as the experimental case studies for analyzing the applicability of the earlier theoretical discussions since they are paradigmatic MC materials of SOPT and FOPT, respectively.

Fig. 3.19 shows the temperature dependences of the specific heat for Gd and $Gd_5Si_2Ge_2$ for magnetic fields of 0, 2, 5, 7.5 and 10 T.

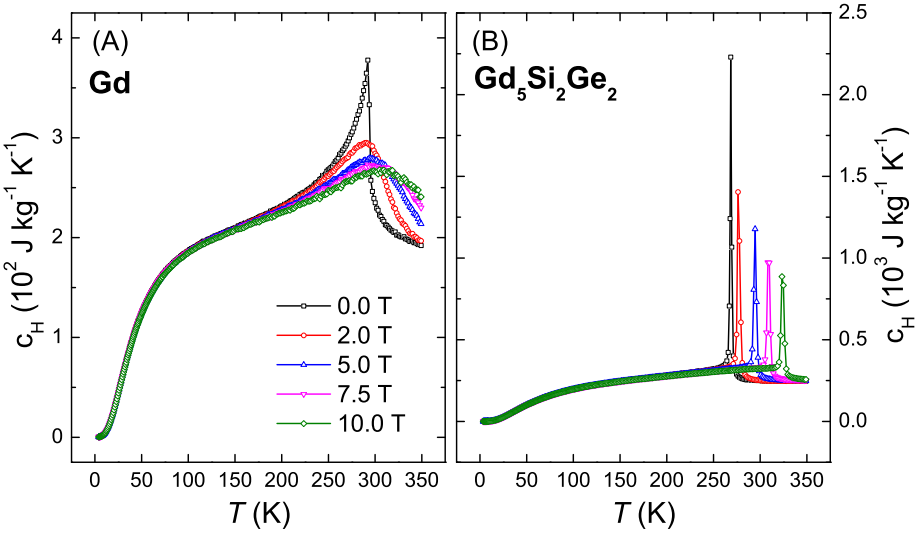

Figure 3.19: Temperature dependence of the specific heat capacity for different magnetic fields for Gd (A) and $Gd_5Si_2Ge_2$ (B).

These sets of data were provided by Prof. Pecharsky (Ames Laboratory) and more details about the samples and the calorimetric measurements can be found in [138]. The total entropy was calculated according to Eq. 3.5, wherein the original heat capacity data were truncated for different selected initial temperatures (the lowest temperature that was experimentally obtained is 4 K).

The temperature dependence of Δs_T^{ap} (A) and ΔT_S^{ap} (B) together with their corresponding Φ differences (insets) using different T_{ini} for Gd for 7.5 T are presented in Fig. 3.20. Using the curves integrated from 4 K as the reference (it gives the closest approximation to that integrated from 0 K), the Φ differences are temperature independent in the case of Δs_T^{ap} while those for the ΔT_S^{ap} curves are temperature dependent.

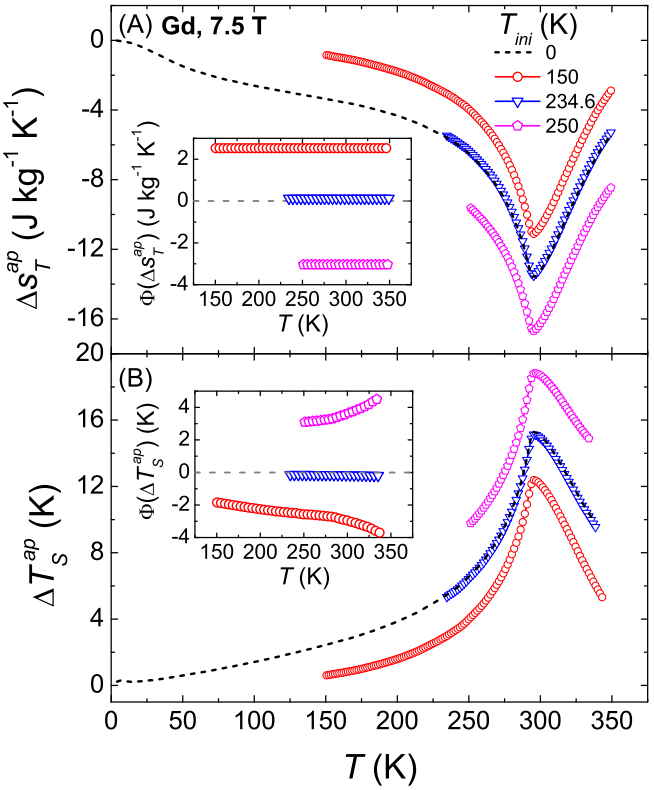

Figure 3.20: Temperature dependence of Δs_T^{ap} (A) and ΔT_S^{ap} (B) at 7.5 T for different initial temperatures for Gd. The insets show the temperature dependence of the Φ difference of each approximated curve with respect to the curve integrated from 4 K.

For $Gd_5Si_2Ge_2$, the temperature dependences of Δs_T^{ap} (A) and ΔT_S^{ap} (B) together with their corresponding Φ differences (insets) calculated using different T_{ini} for 7.5 T are shown in Fig. 3.21. It is observed that the $\Phi(\Delta s_T^{ap})$ is temperature-independent while it is temperature-dependent for $\Phi(\Delta T_S^{ap})$, showing a peak in the region close to the transition temperature. It was shown that our model predicted that the temperature dependence of $\Phi(\Delta T_S^{ap})$ follows a T/c_H trend. T/c_H shows a peak near the transition temperature for $Gd_5Si_2Ge_2$ while a bend near the T_C for Gd, both illustrating the agreement between numerical results and experimental.

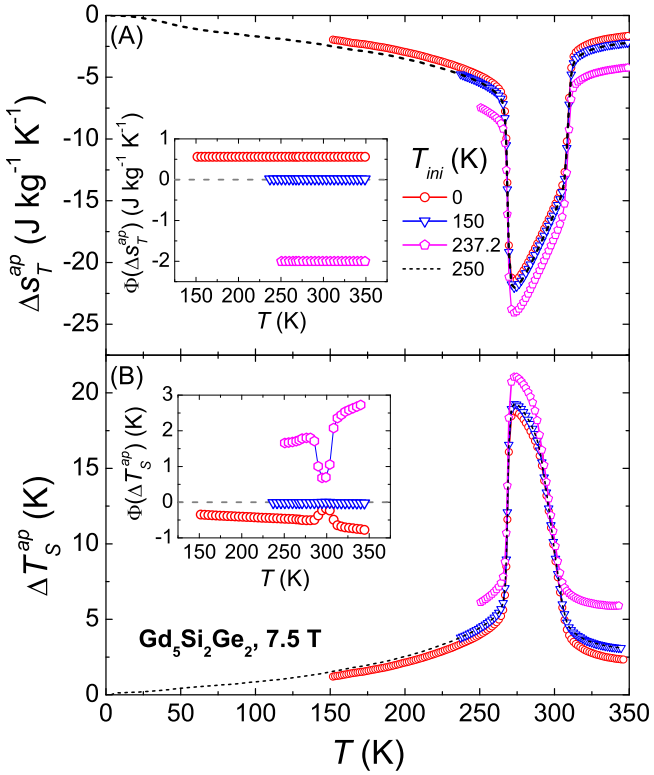

Figure 3.21: Temperature dependence of Δs_T^{ap} (A) and ΔT_S^{ap} (B) at 7.5 T for different initial temperatures for $Gd_5Si_2Ge_2$. The insets show the temperature dependence of the Φ difference of each approximated curve with respect to the curve integrated from 4 K.

$\Phi(\Delta s_T^{ap,pk})$ as a function of T_{ini} is plotted in Fig. 3.22 for various magnetic fields. It is seen that the approximated MC curves deviate in a non-monotonic trend after the integration from 4 K. Despite the observed noise in the curves, it is clear to see the trend with T_{ini} (the plotted lines are guides to the eye). The observed noise is less evident for Gd compared to $Gd_5Si_2Ge_2$. T_{ini}^{opt} can be identified from these experimental data for both samples (i.e. both types of MC materials) as mentioned in the previous section. It can be also observed that the role of finite T_{ini} is relatively less significant for $Gd_5Si_2Ge_2$ than for Gd, as was previously predicted by the simulations.

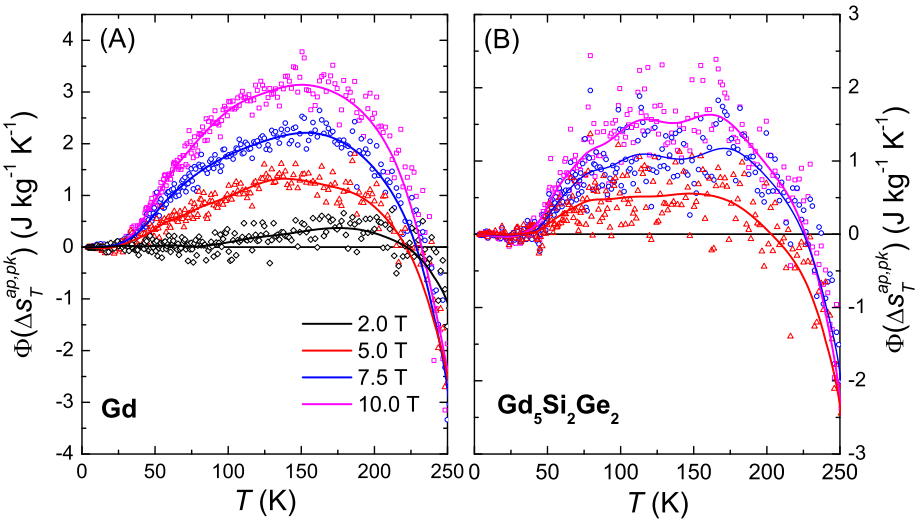

Figure 3.22: $\Phi(\Delta s_T^{ap,pk})$ as a function of T_{ini} for different applied magnetic field changes for Gd (A) and $Gd_5Si_2Ge_2$ (B). Lines are guides to the eye. For $Gd_5Si_2Ge_2$, the curve corresponding to 2 T has a poor signal to noise ratio due to the relative lower importance of the approximation for FOPT and therefore it is not plotted.

For simulations of multiphasic MC material, a non-interacting model for the heat capacity is assumed. Firstly, the simplest case is studied: a biphasic material. With this, the heat capacity of the composite is expressed as:

$$C = (1 - x_2)C_1 + x_2C_2, \tag{3.23}$$

being x_2 the phase fraction of phase 2 (secondary phase) and C_1 and C_2 are the heat capacities of phases 1 and 2, respectively. The heat capacity of each phase is obtained as the sum of the contributions of the magnetic, lattice and electronic subsystems of that particular phase (as for single phase materials).

The biphasic material is composed of two magnetic phases with different Curie temperatures ($T_{C,1}$ and $T_{C,2}$ for phases 1 and 2, respectively). Its simulations were performed by fixing $T_{C,1}$ to that of the benchmark MC material, Gd (i.e. 293 K), while $T_{C,2}$ was modified. The MC response was

determined using the simulated c_H data and further plotted in Fig. 3.23 as a function of temperature for different T_{ini} values for 1 T. It can be observed that Δs_T^{ap} curves deviate from that corresponding to $T_{ini} = 0$ K, whereby the deviations follow a temperature-independent trend. This is also previously observed for single phase case, which indicates that the deviations are not affected by the number of phases. Inset of Fig. 3.23 shows the $\Phi(\Delta s_T^{ap,pk})$ differences as a function of T_{ini}, wherein an overall non-monotonic behavior is observed though accompanied by some features different from the case of single phase materials.

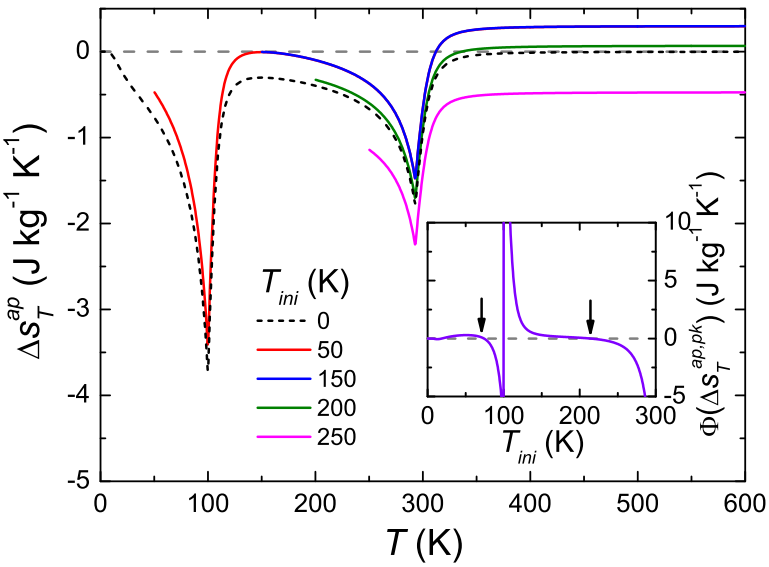

Figure 3.23: Temperature dependence of Δs_T^{ap} simulated for a biphasic material with $x_2 = 0.5$ and $T_{C,2} = 100$ K using different T_{ini} for 1 T. Inset: Φ differences at the peak temperature as function of T_{ini}.

There are two main temperature values for which zero deviations can be identified: one below $T_{C,2}$ and $T_{C,1}$, and the other between $T_{C,2}$ and $T_{C,1}$ (both are marked by arrows in the figure). They are related to the T_{ini}^{opt} of each individual phase but not the exact value of the single phase, as it is influenced by the other phase. When T_{ini} is close to $T_{C,2}$, a discontinuity in Φ is observed at $T_{C,2}$, implying that the presence of

extra phases at low temperatures can considerably affect the calculated MC response from heat capacity data. Nevertheless, it is important to note that the proposed method for experimentally identifying T_{ini}^{opt} is also applicable for multiphasic cases.

A similar analysis was also performed for ΔT_S, where the deviations from that integrated from 0 K can be observed to follow a temperature-dependent behavior. As a first approximation, the temperature dependence of these deviations is proportional to T/c_H, which was earlier observed for the single phase case. The results show a similar curve shape as that found for Δs_T^{ap} (inset of Fig. 3.23), except for the different signs of the deviations (including two points of zero deviation and a discontinuity at $T_{C,2}$). These results considering different phase fractions are shown in Fig. 3.24.

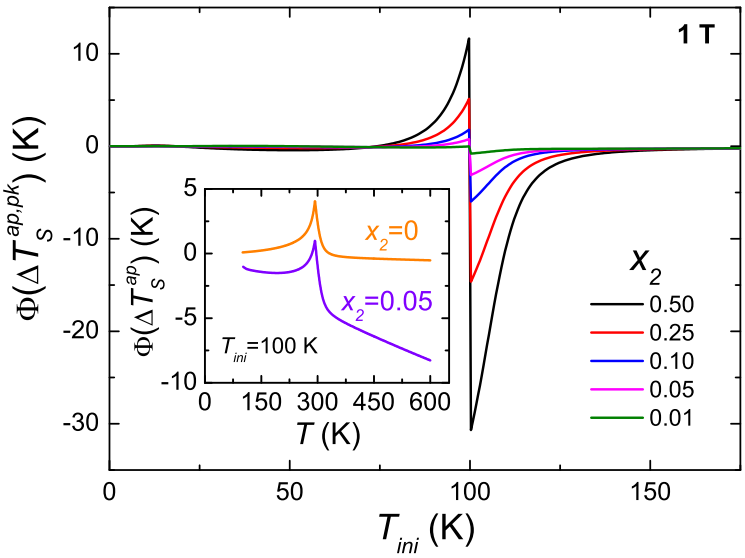

Figure 3.24: Φ differences of $\Delta T_S^{ap,pk}$ as function of T_{ini} in the temperature region close to the phase transition of the secondary phase (various phase fractions are also considered). Inset: Comparison of the temperature dependence of ΔT_S for a pure phase ($x_2 = 0$) and for a system with a secondary phase fraction of 0.05 using $T_{ini} = 100$ K (coinciding with $T_{C,2}$).

In all cases, the T_{ini} dependence of $\Phi(\Delta T_S^{ap,pk})$ shows larger deviations for temperatures above $T_{C,2}$ than for those at lower temperatures, resulting in an asymmetric shape. In addition, when the phase fraction of secondary phase increases, the deviations get more evident, indicating the stronger influence of the extra phase in the system. As an example, the temperature dependence of ΔT_S^{ap} for a pure phase ($x_2 = 0$) is compared to that of a system with a secondary phase fraction of $x_2 = 0.05$ in the inset of Fig. 3.24. For both cases, $T_{ini} = 100$ K (which coincides with $T_{C,2}$) was used. It is evident that this relatively small fraction of secondary phase led to a clear deviation when compared to the curve for $x_2 = 0$. This manifests the significance of accounting for the influence of secondary phases for MC calculations from calorimetric measurements.

For the experimental application of the proposed method, Gd-GdZn MC system was selected for investigation (readers should refer to Section 5.1.3 for elaborated descriptions and discussions).

3.4 Measurement protocols for direct adiabatic temperature change

For FOPT MC materials, it has been previously mentioned that temperature and field variations of the sample state are irreversible in the region close to their FOPT due to the intrinsic hysteresis associated to the phase transition. This leads to implications when calculating Δs_T from isothermal magnetization curves, for which artificial peaks arising from partial transformations or retainment of previous magnetic history states can be found when using continuous measurement protocols [75, 108, 110]. For direct measurements of ΔT_S, the temperature change is measured as a function of the magnetic field and, therefore, the effects of partial transformations during each measurement can also affect these direct MC measurements (also in cyclic conditions [51, 139]). As Heusler alloys exhibit inverse and conventional MC effects, which arise from martensitic

transition (FOPT) and Curie transition of the austenite (SOPT), they were selected for the study of this section: the influence of various protocols to erase the sample's memory for direct ΔT_S measurements of SOPT and FOPT MC materials [140].

The Heusler compounds for study were nominally $Ni_{49}Mn_{36}In_{15}$ and $Ni_{49.5}Mn_{35.5}In_{15}$ (detailed information on their synthesis and structural characterization can be found in [141]). Their temperature dependences of σ for 0.05 T are shown in Fig. 3.25. It can be observed that they exhibit a martensitic (martensite to austenite) transition followed by a Curie transition of the austenitic phase at higher temperatures.

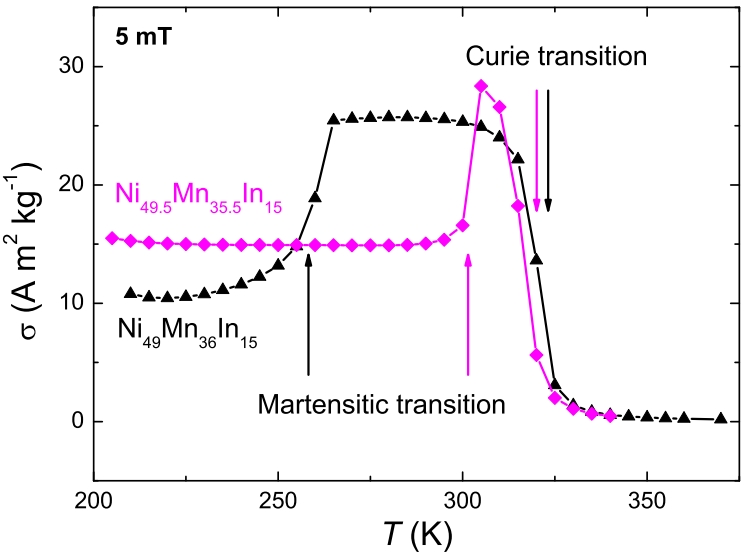

Figure 3.25: Temperature dependence of σ for $Ni_{49}Mn_{36}In_{15}$ and $Ni_{49.5}Mn_{35.5}In_{15}$ measured at low field.

Fig. 3.26 shows the temperature dependence of ΔT_S measured while cooling for 1.76 T (at a sweep rate of 0.5 T s^{-1}) with continuous and discontinuous measurement protocols for $Ni_{49.5}Mn_{35.5}In_{15}$. The latter consists of erasing of the memory of the sample, which was performed by subjecting it to field heating up to a reset temperature of 350 K (this

was selected as it is well above the martensitic transition $\sim$ 295 K) prior to measurements at each temperature.

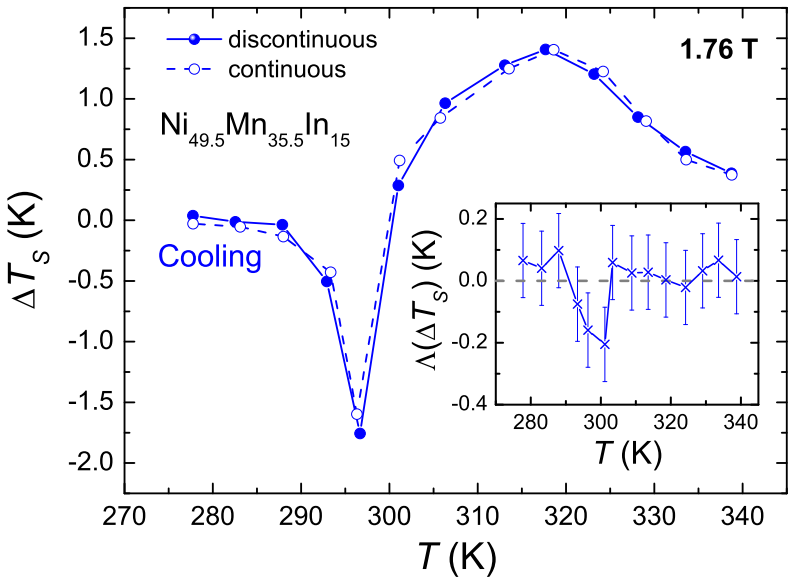

Figure 3.26: Temperature dependence of ΔT_S for $Ni_{49.5}Mn_{35.5}In_{15}$ for 1.76 T measured using discontinuous (solid symbols) and continuous (hollow symbols) cooling protocols. Inset: Temperature dependence of $\Lambda(\Delta T_S)$.

For a quick glance, no significant difference in the curves is observed in the studied temperature range (martensitic FOPT and ferro-paramagnetic SOPT) when erasing the history of the sample or not doing it. When taking the difference of both curves, defined as $\Lambda(\Delta T_S)$ (inset of Fig. 3.26), an observable difference is seen for the region close to the martensitic transition, however, the error bars prevent any further discussion.

For $Ni_{49}Mn_{36}In_{15}$, its temperature dependence of ΔT_S for 1.76 T measured while cooling (A) and heating (B) are presented in Fig. 3.27. In this case, the cooling protocol was performed by subjecting it to field heating up to a reset temperature of 350 K while for heating, a reset temperature of 200 K at zero field was used. In this case, significant differences between the continous and discontinuous measurement curves are clearly

observed (further magnified by $\Lambda(\Delta T_S)$ in the inset of Fig. 3.27). The MC response associated to the martensitic transition shows an underestimation of ~ 20 % when not erasing the thermal and field history of the sample, unlike the case for the conventional MC effect. This is clearly depicted in the insets.

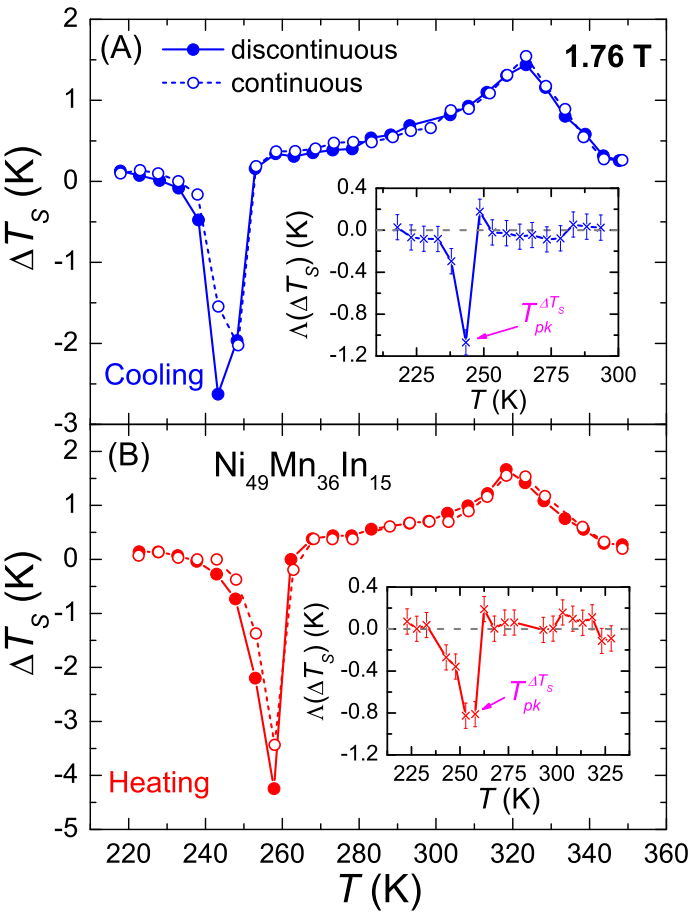

Figure 3.27: Temperature dependence of ΔT_S for $Ni_{49}Mn_{36}In_{15}$ for 1.76 T measured using discontinuous (solid symbols) and continuous (hollow symbols) cooling (A) and heating (B) protocols. Insets: Temperature dependence of $\Lambda(\Delta T_S)$.

To compare these results obtained for both compositions, it is important to note that sample masses and shapes used are quite similar. Hence, any

observed differences in the data are related to the hysteretic behavior when magnetizing/demagnetizing the samples while the measurement procedure register the induced temperature change at a certain initial temperature of the sample. Fig. 3.28 shows the magnetization/demagnetization curves at selected temperatures close to the martensitic transitions of both samples.

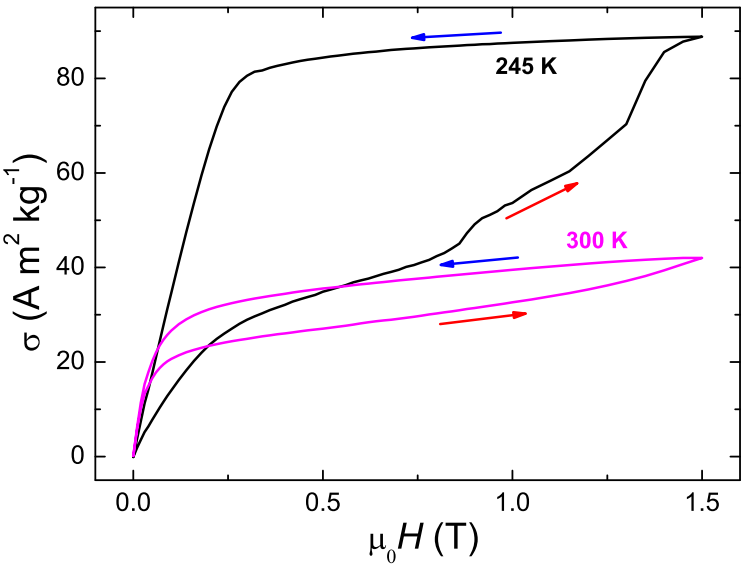

Figure 3.28: Magnetic field dependence of σ for $Ni_{49}Mn_{36}In_{15}$ and $Ni_{49.5}Mn_{35.5}In_{15}$ at temperatures close to their martensitic transition.

The hysteresis can be quantified by the area enclosed between magnetization/demagnetization curves, being 50.2 and 9.6 A m^2 kg^{-1} T^{-1} for $Ni_{49}Mn_{36}In_{15}$ and $Ni_{49.5}Mn_{35.5}In_{15}$, respectively. According to this, the former exhibits a larger magnetic hysteresis, which attributes to the huge $\Lambda(\Delta T_S)$ found when accounting for the differences between considering the sample's history or not considering it. Moreover, the observed thermal hysteresis span between the cooling and heating curves is larger for $Ni_{49}Mn_{36}In_{15}$ sample ($\approx$ 12 K) than that for $Ni_{49.5}Mn_{35.5}In_{15}$ ($\approx$ 6 K), which agrees with the previous argument. In addition, the observed span of $\approx$ 6 K is equivalent to the selected temperature step used for the measurements (i.e. 5 K), hence, further measurements were

performed with a finer step resolution of 2.5 K. Using a finer temperature step resolution of 2.5 K, the influence of the sample's prior history on its MC response becomes more significant near the martensitic transition, in particular for $Ni_{49}Mn_{36}In_{15}$, as shown in Fig. 3.29. In this case, the cooling protocol was used with a reset temperature of 350 K and 1.76 T. The underestimation of ΔT_S^{pk} associated to the martensitic transition increases to ∼40 % (a two-fold increase from that observed using 5 K). Moreover, it can be observed that the peak temperature shifts to higher temperatures when not accounting for the history of the sample.

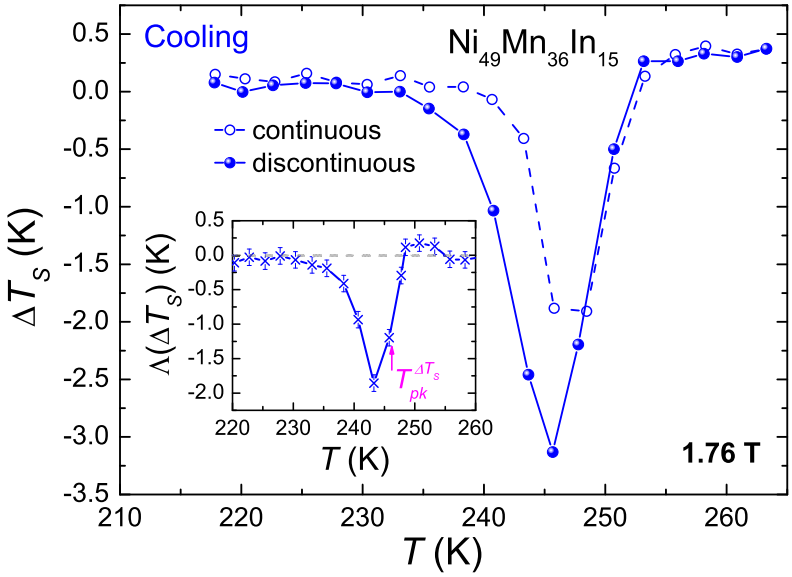

Figure 3.29: Temperature dependence of ΔT_S for $Ni_{49}Mn_{36}In_{15}$ for 1.76 T using discontinuous (solid symbols) and continuous (hollow symbols) cooling protocols.

In contrast to Δs_T, wherein an overestimation is obtained from indirect measurements when the memory of the sample is not accounted for, the effect of using an inappropriate measuring protocol for direct ΔT_S gives rise to a decrease in the measured response close to the martensitic transition. This difference is ascribed to the application of the Maxwell relation to different isothermal magnetization measurements

for determining Δs_T. The different fraction of phase transformation (due to a temperature variation) at the initial magnetic field when compared to the one in an isofield curve leads to an artificial increment of the magnetization change that produces an spurious spike. In contrast, for direct ΔT_S measurements the deviations are ascribed to the irreversibility of the magnetization/demagnetization path, which leads to a reduced fraction of the transformation, resulting in a decrease in the ΔT_S value. In the case of using a finer temperature step, the differences in the amount of transformed fraction ascribed to the irreversibility increases with the number of measurement steps (every measurement contributes to the total amount of transformed phase), which magnifies the error of the continuous protocol.

3.5 Conclusions

In this chapter, the influence of various experimental factors on the MC response was analyzed. For the indirect determination of the MC effect, in the case of calculating Δs_T and its field dependence exponent n from magnetization measurements, the effects of the demagnetizing field and compositional inhomogeneities were analyzed. For determining both Δs_T and ΔT_S from calorimetric measurements, the influence of the low temperature limitation was studied. Finally, the influence of measurement protocols (discontinuous and continuous) on direct ΔT_S was studied. For these different studies, several conclusions are derived as follow:

- The influence of the demagnetizing factor on Δs_T and the exponent n was experimentally and numerically studied, taking Co-based amorphous alloys as the case study due to the mayor contribution of shape anisotropy. Though the demagnetizing factor does not significantly affect Δs_T, it was found that it plays a role in the exponent n, in particular at the ferromagnetic regions for low fields. Theoretical values of $n \approx 1$ are found at ferromagnetic region and

only decreases to a minimum at the T_C. However, the contribution of demagnetizing factor of the samples is observed to cause deviations from this feature for temperatures well below T_C and at T_C, which can, in turn, lead to errors when determining critical exponents. This deviation is also predicted by results from numerical simulations using the A-N EOS by introducing shape anisotropy.

- For analyzing the MC behavior of materials with compositional inhomogeneities, we assumed a Gaussian distribution of T_C. Experimentally, it is observed that mechanically alloyed samples show an exponent n abnormally high at T_C when compared to those of rapid quenched samples, both with the same composition. This should be because the milled samples exhibit amorphous matrix with some crystallites that are retained from elemental precursors, causing a distribution of T_C. The results of modelling the Δs_T of the former sample by the A-N EOS using a Gaussian distribution of T_C show a good agreement with the experimental data, further reinforcing the assumption of a distribution. In addition, a standard deviation around 30 K is estimated, which implies a variation of 1 at. % in the B content of the matrix, being a realistic value.

- Simulations of c_H of single phase and multiphasic MC materials were performed using the B-R model, Debye and Fermi models under the assumption of non-interactting phases. It was found that the MC curves using an optimal choice of the initial temperature of integration, T_{ini}^{opt}, are the same as those integrated starting from a temperature close to zero kelvin. This feature is observed to be η independent (i.e. valid for both FOPT and SOPT cases). The values obtained for T_{ini}^{opt} are the same for both Δs_T and ΔT_S magnitudes. In addition, it is shown that when determining Δs_T from a finite T_{ini} different from 0 K, the resulted deviations are temperature independent. This is not the case for ΔT_S: the differences are temperature dependent, whereby they follow T/c_H in first approximation. These are also confirmed by experimental

measurements of Gd and $Gd_5Si_2Ge_2$, indicating the good agreement between numerical simulations and experimental results. It is further proposed that T_{ini}^{opt} can be experimentally found as those T_{ini} that makes MC magnitudes equal to zero well above the transition. For multiphasic materials, T_{ini}^{opt} is also observed. The MC deviations and T_{ini}^{opt} values vary with the amount of secondary phases and the separation of transition temperatures between the phases. When T_{ini} is close to T_{trans} of one of the phases, the approximated data separate strongly with respect to those integrated from zero kelvin, even for small amounts of the secondary phase.

- The influence of discontinuous and continuous measurement protocols on the direct ΔT_S of Ni-Mn-In Heusler compounds (that exhibit a FOPT martensitic transition) was investigated. For measurements that did not account for the previous state of the samples (i.e. using continuous protocols), underestimations of ΔT_S values were obtained in the region of the martensitic transition, with together a shift of the peak temperature. These discrepancies are shown to be highly dependent on the temperature span of the hysteresis of the sample with respect to the temperature step used for the measurements (discrepancies up to 40 % were observed for $Ni_{49}Mn_{36}In_{15}$).

4 Analyses based on the field dependence of the magnetocaloric effect

As MC effect maximizes at the abrupt change of magnetization that occurs near the magnetic phase transition, its study can also offer useful insights on the thermomagnetic phase transitions of the material. Hence, this chapter will further describe various analyses based on the field dependence of the MC effect that are shown as powerful tools for investigating thermomagnetic phase transitions. A procedure to determine the Curie temperature of SOPT MC materials is proposed. The critical exponents of the transition can also be determined even for multiphasic materials (this could not be attained by other conventional methods). Furthermore, analyses to determine the order of phase transitions and the critical SOPT-FOPT composition will also be covered. Results from the numerical calculations are found to exhibit excellent agreement to the experimental data.

4.1 Curie temperature

T_C is an essential parameter to describe the magnetic behavior of thermomagnetic SOPT. Any inaccuracy in its determination could lead to erroneous interpretation of the data, which also has consequences in the determination of critical exponents of the transition.

The method proposed in this thesis for T_C determination is based on the scaling laws of the MC effect. It has been already demonstrated that Δs_T scales at the critical region as:

$$\frac{\Delta s_T}{\Delta H^{(1-\alpha)/\Delta}} = f_{s,\pm}\left(\frac{|t|}{\Delta H^{1/\Delta}}\right). \tag{4.1}$$

If the magnetic field dependence of Δs_T follows a power law in the form of $\Delta s_T \propto \Delta H^{n(T,H)}$ and defining $\varrho = t/\Delta H^{1/\Delta}$, the exponent n can be obtained using the following equation:

$$n(T, \Delta H) = \frac{\partial \ln \Delta s_T}{\partial \ln \Delta H} = \frac{1-\alpha}{\Delta} - \frac{1}{\Delta}\left(\frac{\partial \ln f_{s,\pm}(\varrho)}{\partial \ln \varrho}\right) \tag{4.2}$$

whereby Eq. (4.1) has been used. The derivative vs. ϱ vanishes at $T = T_C$, where $\varrho = 0$ and $f_{s,\pm}(0)$ is a constant value, and also at $T = T_{pk}^{\Delta s_T}$, where $\mathrm{d}s(\varrho)/\mathrm{d}\varrho = 0$, leaving:

$$n(T_C, \Delta H) = n(T_{pk}^{\Delta s_T}, \Delta H) = \frac{1-\alpha}{\Delta}. \tag{4.3}$$

Therefore, the values of n are the same at T_C and $T_{pk}^{\Delta s_T}$ and also field independent (as it is related with the critical exponents of the transition). Based on Eq. (4.3), the proposed method wherein T_C can be obtained from MC data following three steps:

1. Firstly, $T_{pk}^{\Delta s_T}$ is to be determined from the $\Delta s_T(T, \Delta H)$ curves.
2. Next, $n(T, \Delta H)$ is calculated from the experimental $\Delta s_T(T, \Delta H)$ data and evaluated at $T_{pk}^{\Delta s_T}$.

3. Finally, T_C is identified as the temperature for which $n = n(T_{pk}^{\Delta s_T})$.

These 3 steps of the proposed method for T_C determination are further illustrated as (1), (2) and (3) in Fig. 4.1 (according to the previous numeration), wherein it shows the temperature dependence of simulated Δs_T and n for 1.5 T using A-N EOS and Heisenberg critical exponents ($\gamma = 1.388$ and $\beta = 0.367$) with typical values for amorphous alloys ($a = 1$ $(10^{-4}$ T$)^{1/\gamma}$(A m^2 kg^{-1})$^{-1/\gamma}$K^{-1} and $b = 0.01$ $(10^{-4}$ T$)^{1/\gamma}$ (A m^2 kg^{-1})$^{-(1/\beta+1/\gamma)}$ and $T_C = 300$ K). It can be observed that $T_{pk}^{\Delta s_T}$ at 1.5 T does not coincide with T_C (it is shifted to higher temperatures as the magnetic field increases).

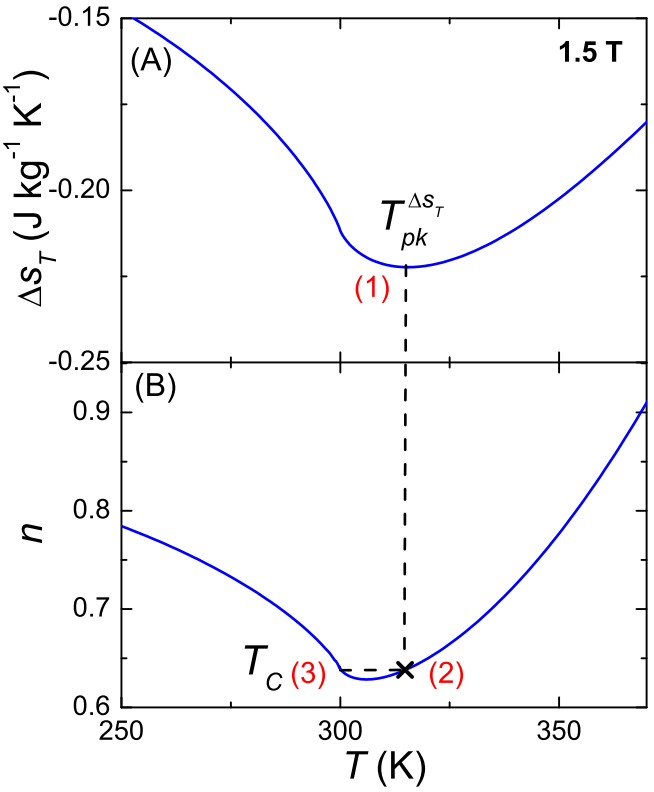

Figure 4.1: Temperature dependence of the Δs_T (A) and n (B) simulated for 1.5 T using Heisenberg critical exponents. Illustration of the proposed method to obtain T_C from MC measurements.

For a more general numerical investigation, Fig. 4.2 shows the field dependence of $T_{pk}^{\Delta s_T}$ and T_C obtained after applying the method simulated upon applying the proposed procedure using Heisenberg (main panel) and mean field (inset) exponents.

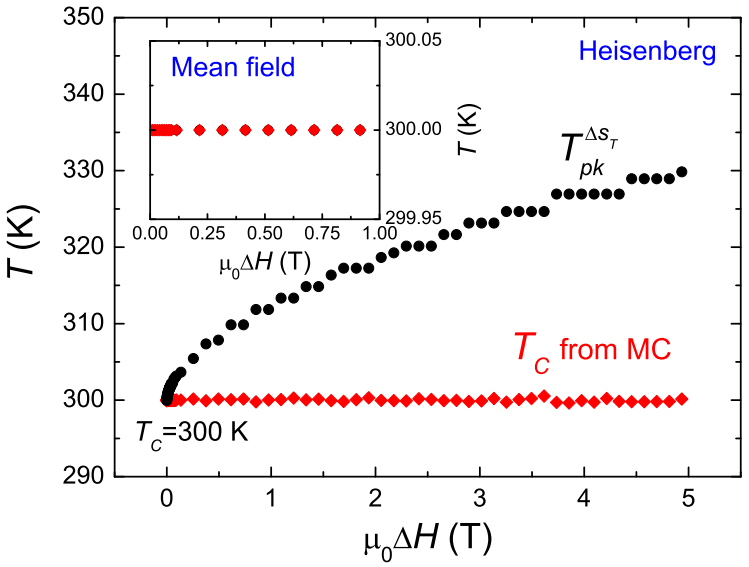

Figure 4.2: $T_{pk}^{\Delta s_T}$ and T_C obtained after applying the proposed method to the simulated data using Heisenberg (main panel) and mean field (inset) exponents.

Using Heisenberg critical exponents, $T_{pk}^{\Delta s_T}$ varies with applied magnetic field and coincides with T_C at $H = 0$, meanwhile T_C obtained from the proposed method remains field independent and equal to T_C. For the mean field case, $T_{\Delta s_T}^{pk}$ and T_C from MC method are field independent and coincident with T_C as shown in the inset of Fig. 4.2. This field independence is an advantage of the proposed method.

The proposed procedure was applied to an amorphous alloy of nominal composition $Fe_{62}Cr_{12}Cu_1Nb_3Si_{15.5}B_{6.5}$ prepared by melt spinning by Vacuumschmelze (details about structure and magnetic properties can be found in [142]). To apply the method, $\Delta s_T(T, \Delta H)$ and $n(T, \Delta H)$

near T_C were calculated from magnetization measurements according to Eqs. (1.16) and (1.37), respectively. Gradual n values (Fig. 4.3), which monotonically increase from the minimum at values close T_C up to 2 for $T >> T_C$, according to their SOPT nature are observed [90]. The obtained $T_{pk}^{\Delta s_T}$ values from $\Delta s_T(T, \Delta H)$ vs. T curves are shown for 0.05 and 1.5 T, for which a clear evolution can be observed. It can be observed that up to 0.3 T the $n(T_{\Delta s_T}^{pk})$ is not constant due to the multidomain regime of the sample (as despicted in the inset of Fig. 4.3). Magnetic fields below 0.3 T are not considered in the analysis to avoid erroneous values.

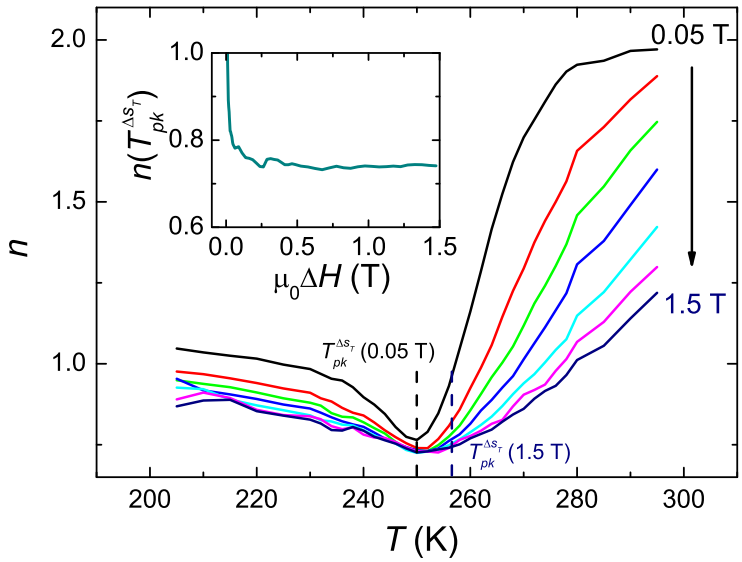

Figure 4.3: Experimental temperature dependence of exponent n for different magnetic field changes for $Fe_{62}Cr_{12}Cu_1Nb_3Si_{15.5}B_{6.5}$ amorphous alloy. Inset: Field dependence of $n^{T_{pk}^{\Delta s_T}}$

Using the above data, the proposed procedure to determine T_C was performed and the obtained values of $T_{pk}^{\Delta s_T}$ and T_C are plotted against magnetic field values in Fig. 4.4. The same qualitative behavior for the simulated data using Heisenberg critical exponents is observed. With respect to the method proposed though $T_{pk}^{\Delta s_T}$ increases with the applied magnetic field, the calculated T_C is field independent, with an average

value of 248.1(5) K. At low fields (below 0.3 T), the measurements do not have a good resolution and the exponent n varies artificially. It is worth mentioning that this is not a limitation of the proposed method as the result is field independent and the value of T_C can be obtained at higher fields, wherein the signal to noise ratio is enhanced.

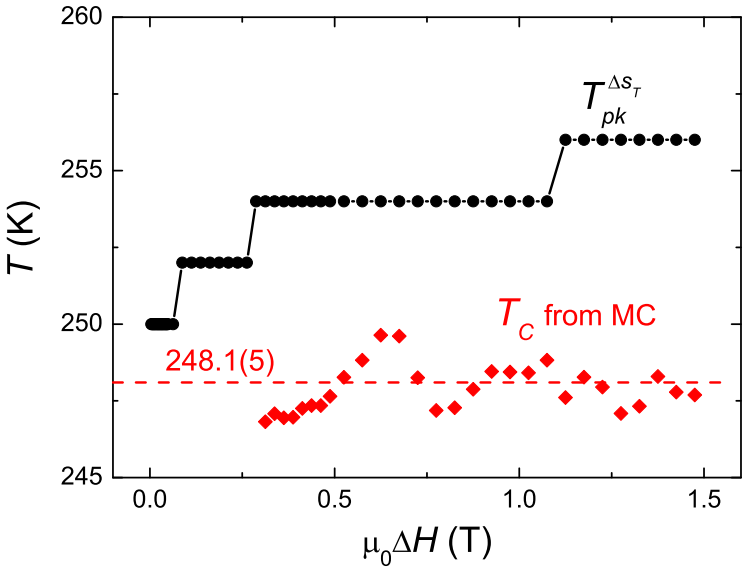

Figure 4.4: Field dependence of $T_{pk}^{\Delta s_T}$ and T_C obtained from the proposed procedure for $Fe_{62}Cr_{12}Cu_1Nb_3Si_{15.5}B_{6.5}$ amorphous alloy.

In addition, T_C was further compared to the values obtained using conventional techniques: inflection point of $M_H(T)$ curves, Arrott plot and K-F methods. The first approach approximates T_C by the inflection point of the magnetization vs. temperature curves ($M_H(T)$). The obtained value is field dependent. The Arrott plot method is based on the assumption of mean field theory and T_C approximation comes from the temperature which corresponds to the isothermal straight line that crosses the origin of $H/M_T(H)$ vs. $M_T(H)^2$. It can be generalized for any set of critical exponents, thus also known as generalized Arrott plot. The main drawback of this technique is the required knowledge of critical exponents (typical mean field or Heisenberg values are used as the first

approximation) as any inappropriate value selection will significantly affect the T_C determination thereafter. Finally, the K-F method employs an iterative procedure based on the previous modified Arrott plot method (explained in Chapter 1).

Fig. 4.5 shows the T_C values obtained using the inflection point method (A), while (B) presents the Arrott plot of the studied sample.

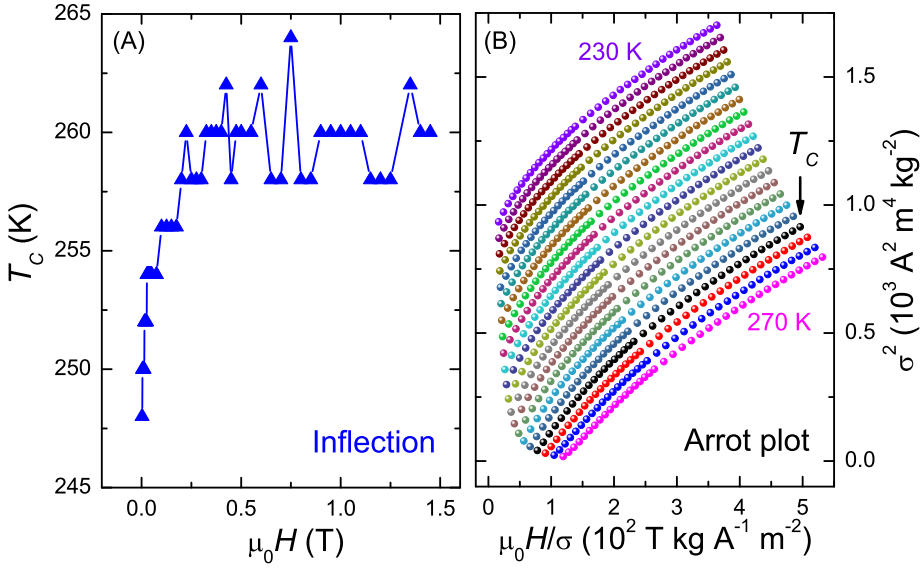

Figure 4.5: Field dependence of T_C using the inflection point method (A) and Arrott plot (B) for $Fe_{62}Cr_{12}Cu_1Nb_3Si_{15.5}B_{6.5}$ amorphous alloy.

In the first technique, for relatively low fields, a strong field dependence of T_C can be observed (e.g. for 2.5 mT, $T_C = 248(1)$ K and for 30 mT, $T_C = 254(1)$ K). On the other hand, the Arrot plot method yields to an erroneous value of $T_C = 263(1)$ K from the isothermal that intercepts at the origin. In the case of assuming the critical exponents of the Heisenberg model for a generalized Arrott plot, $T_C = 255(1)$ K is obtained. This indicates that the selection of the critical exponents strongly affects the value of T_C obtained using this method.

Fig. 4.6 shows the temperature plots of Y and X to illustrate the K-F method. This is obtained after 15 iterations, sufficient to reach convergence, obtaining $\beta = 0.43$, $\gamma = 1.67$ and $T_C = 249.6(3)$ K. It is worth mentioning that it is time consuming to obtain this final value of T_C using this method. On the other hand, our proposed method based on MC effect does not require any iterative or fitting routines (just linear interpolations).

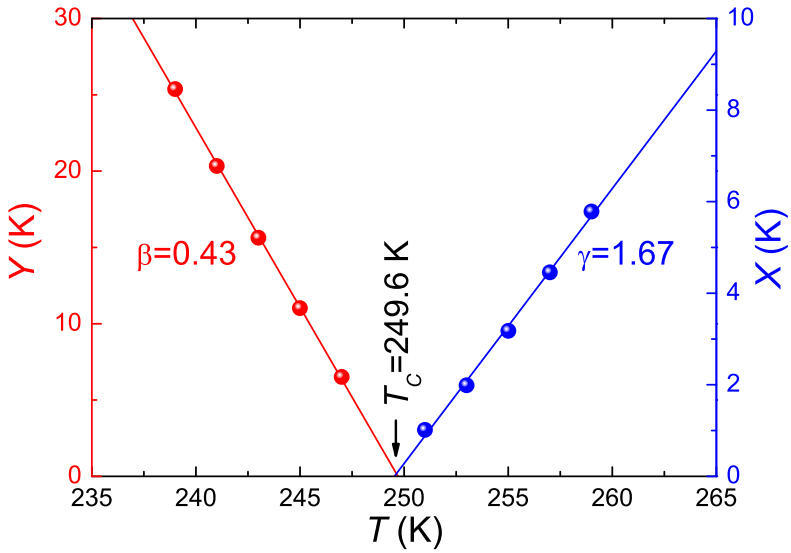

Figure 4.6: X, Y vs. T plots from the K-F method for $Fe_{62}Cr_{12}Cu_1Nb_3Si_{15.5}B_{6.5}$ amorphous alloy after convergence.

As a summary, a good agreement between MC and K-F methods is observed. For the inflection point method, an approximate value is obtained for 2.5 mT though it is strongly affected by magnetic fields (even for relatively low fields as 30 mT). Overestimated values are obtained in the case of Arrott plot method using mean field and Heisenberg critical exponents (as they are quite different from those obtained by K-F).

To reproduce the magnetization of real measurements using the A-N EOS, different levels of noise using two different approximations have been

included [143]. A constant relative error (ϵ) for all the measured moment values has been considered:

$$\sigma(T,H) = \sigma_{AN}(T,H)\left[1 + 2\epsilon\left(0.5 - \mathrm{rand}(T,H)\right)\right], \tag{4.4}$$

where σ_{AN} is the specific moment obtained from the A-N EOS, rand is a random number, between 0 and 1, different for each simulated point. The values of the magnetization can differ from the noise-free data in $\pm\epsilon\sigma_{AN}$. Well prepared experiments typically contain a signal-to-noise ratio level of 100:1 (ϵ=0.01), as typically the moment range is set to auto-range level. To quantify the signal-to-noise ratio, the root mean square (RMS) has been used:

$$RMS(\psi) = \sqrt{\sum_{i=1}^{N} \frac{1}{N} \frac{\psi_i - \overline{\psi}}{\overline{\psi}}}, \tag{4.5}$$

where ψ is a certain magnitude which has N values (where i correspond to a certain value) and $\overline{\psi}$ is the mean ψ value. In our case the used mean values are those calculated without noise. With respect to the determination of the Curie temperature, Fig. 4.7 shows the temperature values that can be identified as the T_C for both inflection and MC methods using $\epsilon = 0.01$ (the values for the inflection point method without noise are also plotted). It can be observed that while the values obtained by the inflection point method depart from the value of the Curie temperature introduced in the A-N EOS (300 K) as the magnetic field increases, the values obtained by the MC method are independent of the magnetic field, both for the curves with and without noise. The values obtained by the MC method have an upper limit that is the value of the temperature of the peak entropy change, because $T^{pk}_{\Delta s_T} \geq T_C$. The Curie temperature values obtained by the inflection point method have more noise level than the values obtained by the MC method ($RMS(T_C) = 0.1$ and 0.02, respectively). As the obtained values of the Curie temperature from the MC procedure are field independent, the whole curve can be averaged, being the mean value 301.5(9) K (close to the value used for simulation, taking into account that the temperature step is 2 K).

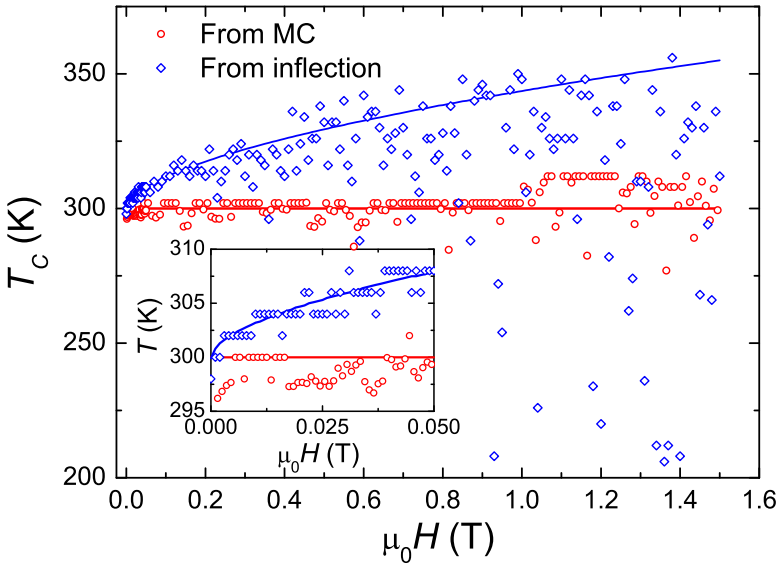

Figure 4.7: Values of the temperature assumed as the Curie temperature determined by the inflection and MC methods for ϵ=0.01 as a function of magnetic field. Inset: magnification of the low magnetic field region.

If we use both methods of determination of T_C up to low fields, for fields up to 0.02 T, the signal-to-noise ratio is similar for the MC and inflection point methods and the mean values are 298.7(3) K and 302.3(2) K, respectively. For larger fields, the results of the inflection point method quickly deviate from the correct Curie temperature value and, as seen in Fig. 4.7, having a larger noise level.

4.2 Critical exponents

From the literature, the most common way to determine the critical exponents is the K-F method. As it has been shown that SOPT MC response is strongly related to the critical exponents of thermomagnetic phase transitions, it is possible to determine the critical exponents using methods based on the magnetic field dependence of the MC effect. In this section, this alternative method will be described and its results will

be compared with those determined from K-F for single phase as-spun ribbons. In addition, the latter technique is limited to single phase systems, and it will be shown that this limitation can be overcome by the alternative method based on the field dependence of MC effect [144]. These studies were performed in amorphous ribbons prepared by melt spinning by Vacuumschmelze (compositions $Ni_{74}Fe_8Si_2B_{16}$ and $Ni_{68.8}Fe_{13.2}Si_2B_{16}$), which serve as the single phase system. They were then heat treated to form nanocrystals in their amorphous matrix, providing biphasic MC system. More details on sample preparation and their microstructures can be found in [144].

Firstly, the power law fittings to the field dependence of MC response were performed to determine the critical exponents of single phase $Ni_{74}Fe_8Si_2B_{16}$ as-spun ribbons. These are illustrated in Fig. 4.8, which shows the field dependences of Δs_T^{pk} (A) and T_r (i.e. the temperature above T_C that corresponds to 70 % of the peak) (B).

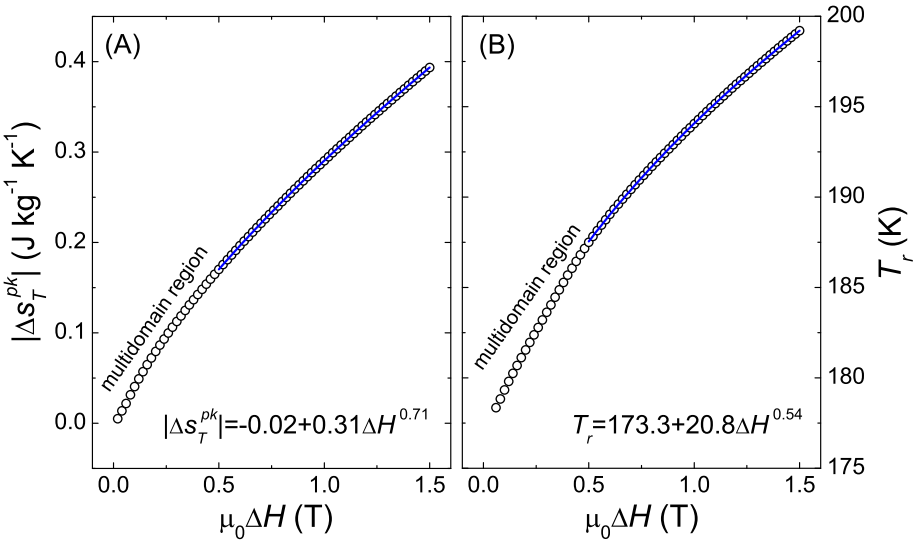

Figure 4.8: Magnetic field dependence of the Δs_T^{pk} (A) and T_r (B) for $Ni_{74}Fe_8Si_2B_{16}$ amorphous alloy (symbols). The different fittings to a power law are represented as blue lines.

Data for low fields (below 0.5 T) are not considered to avoid the region of multidomains. From the correlations of the critical exponents to MC magnitudes (refer to Table 1.1), β, γ and δ were determined from these two fittings. Next, the critical exponents were determined using the K-F method, Fig. 4.9 shows the X and Y vs. T plots after convergence of the values. Table 4.1 shows the comparison of critical exponents β, γ and δ obtained for single phase amorphous $Ni_{74}Fe_8Si_2B_{16}$ and $Ni_{68.8}Fe_{13.2}Si_2B_{16}$ from the fittings of MC analyses and from the K-F method. An excellent agreement is observed between both methods.

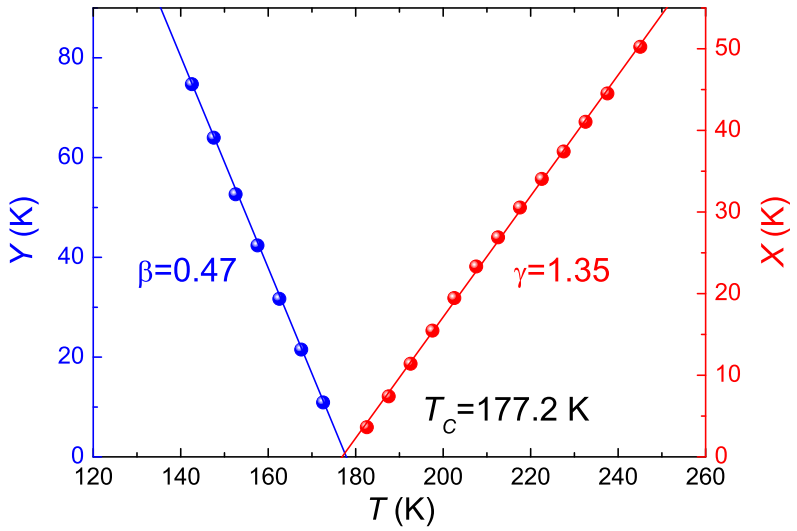

Figure 4.9: X and Y vs. T after applying the K-F method to $Ni_{74}Fe_8Si_2B_{16}$ amorphous alloy: fittings (lines) and experimental data (symbols).

Sample	$Ni_{74}Fe_8Si_2B_{16}$		$Ni_{68.8}Fe_{13.2}Si_2B_{16}$	
Method	K-F	MC	K-F	MC
β	0.47	0.47	0.42	0.41
γ	1.35	1.33	1.51	1.55
δ	3.86	3.82	4.60	4.83

Table 4.1: Critical exponents for $Ni_{74}Fe_8Si_2B_{16}$ and $Ni_{68.8}Fe_{13.2}Si_2B_{16}$ amorphous alloys obtained by the K-F and MC methods.

The reliability of results were further investigated by constructing the universal curves using these critical exponents. There are two possible universal constructions: one presents $\sigma H^{-1/\delta}$ vs. $tH^{-1/(\beta+\gamma)}$ and the other plots $t^{-\beta}\sigma$ vs. $t^{-(\beta+\gamma)}H$. Fig. 4.10 shows the two constructions for $Ni_{74}Fe_8Si_2B_{16}$ amorphous alloy, wherein the curves constructed using the critical exponents from K-F and MC methods are presented in (A)-(B) and (C)-(D), respectively.

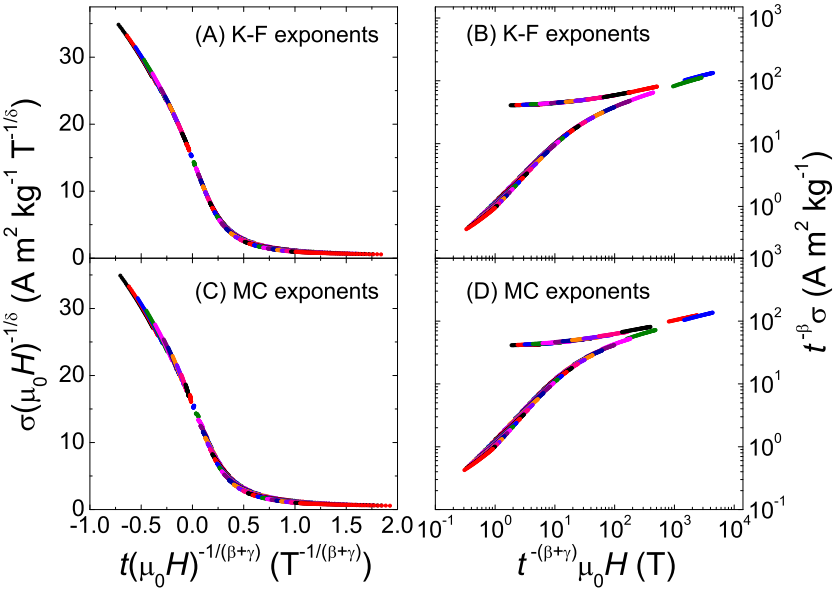

Figure 4.10: Universal constructions for $Ni_{74}Fe_8Si_2B_{16}$ amorphous alloy with critical exponents determined by the K-F (A)-(B) and MC (C)-(D) methods.

It is observed that experimental points collapse for both methods of critical exponent determination, indicating that a good scaling of the results is obtained independently of the method. This is in agreement to Table 4.1.

For the second case study, both samples were partially crystallized by heat treating them in a differential scanning calorimetry to obtain around 20 % of nanocrystalline phase. The formed nanocrystalline phase is $\gamma-$(Ni,Fe). More details about the microstructure of the nanocrystallized samples

can be found in [144]. Similar to the previous case study (fully amorphous counterparts), the critical exponents determined from the power law fits to the field dependence of MC magnitudes are further employed to construct the universal curves. As an example, the universal curves of heat treated $Ni_{74}Fe_8Si_2B_{16}$ ribbons are plotted in Fig. 4.11.

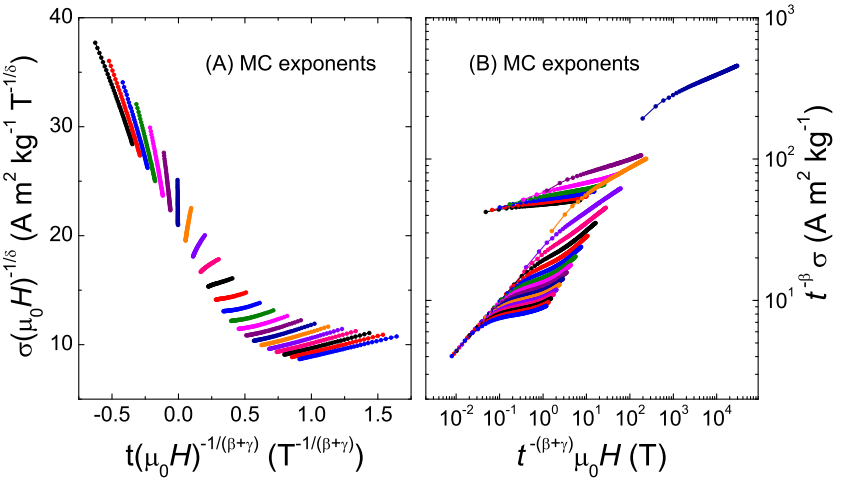

Figure 4.11: Universal constructions for $Ni_{74}Fe_8Si_2B_{16}$ nanocrystalline alloy with critical exponents obtained from MC method (A)-(B).

Important dispersion is observed for both constructions. This can be ascribed to the contribution of the γ-(Ni,Fe) nanocrystalline phase to the total magnetization of the sample. Therefore, the removal of the contribution of this nanocrystalline phase to the magnetization should improve the representation of both universal constructions. To do that, the following process was adopted, assuming that the magnetization of the crystalline phase is temperature independent within the studied temperature range as it is well below its T_C (illustrated in Fig. 4.12):

1. At temperatures much higher than the T_C of the amorphous phase and magnetic fields high enough to saturate the ferromagnetic crystalline phase, the magnetization curves are linear (experimental data as black symbols). Therefore, under these conditions, the

paramagnetic susceptibility of the amorphous phase can be obtained from the slope of this straight line (represented by the red lines).

2. The previously obtained linear magnetic response of the amorphous phase is subtracted from the experimental magnetization data, leaving only the contribution coming from the nanocrystalline phase for analysis (hollow symbols).

3. Therefore, this nanocrystalline contribution is subtracted to each experimental magnetization data for all the studied temperatures, which then results in an estimation of the individual contribution of the amorphous phase.

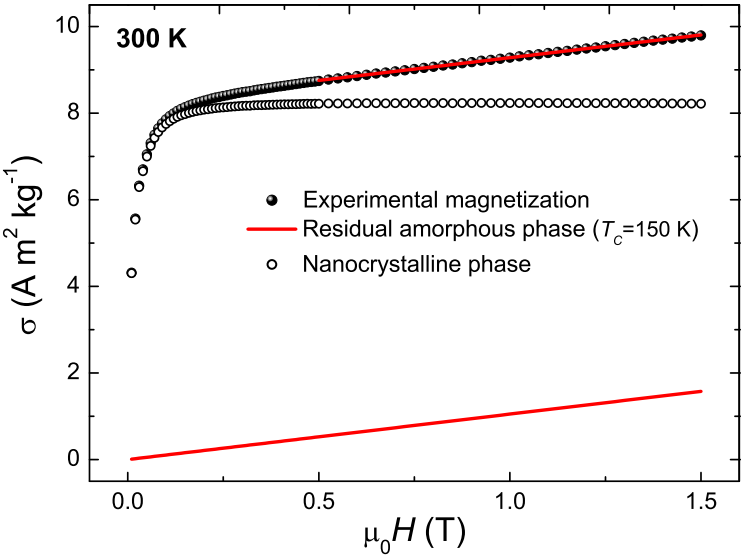

Figure 4.12: Process of removing the contribution of the nanocrystalline phase to the total magnetization for $Ni_{74}Fe_8Si_2B_{16}$ nanocrystalline alloy.

With this, it is possible to apply the K-F method to these data corresponding to the individual contribution of the residual amorphous phase. Table 4.2 shows the critical exponents obtained from both methods (MC and K-F after deconvolution) and a good agreement is observed between them. It is important to stress that the MC method did not

require any deconvolution. The reconstructed universal curves of the contribution of the residual amorphous phase are presented in Fig. 4.13 ((A)-(B):K-F method ; (C)-(D): MC analysis). It can be observed that the formerly observed dispersion is significantly reduced.

Sample	$Ni_{74}Fe_8Si_2B_{16}$ nanocrystalline		$Ni_{68.8}Fe_{13.2}Si_2B_{16}$ nanocrystalline
Method	KF	MC	MC
β	0.56	0.56	0.66
γ	1.37	1.32	0.96
δ	3.44	3.38	2.45

Table 4.2: Critical exponents for $Ni_{74}Fe_8Si_2B_{16}$ nanocrystalline alloy obtained by the K-F and MC methods and for $Ni_{68.8}Fe_{13.2}Si_2B_{16}$ nanocrystalline determined by MC method.

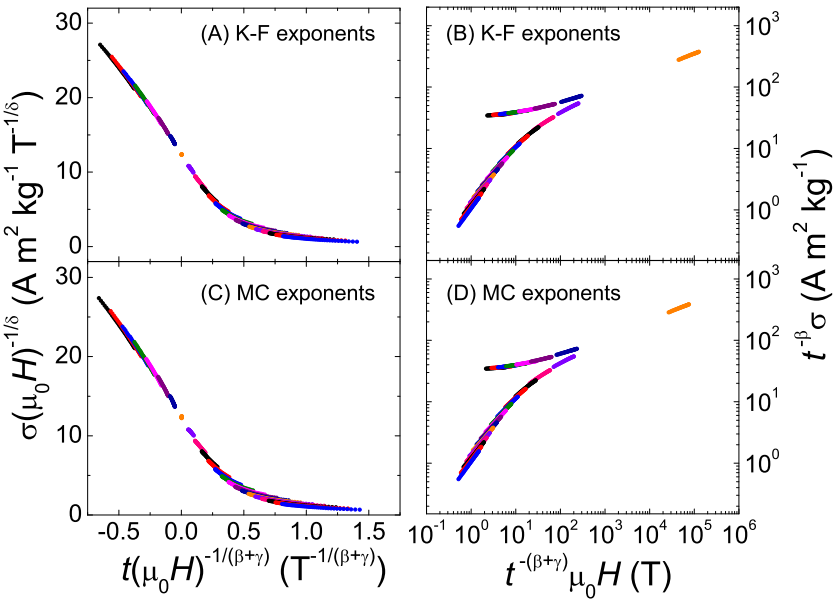

Figure 4.13: Universal curves constructed with critical exponents for $Ni_{74}Fe_8Si_2B_{16}$ nanocrystalline alloy, for which the crystalline contribution has been removed, obtained from K-F (A)-(B) and MC (C)-(D) methods.

The large separation between the Curie temperatures of the amorphous and nanocrystalline phases in the $Ni_{74}Fe_8Si_2B_{16}$ sample yields the most

favorable case to apply the proposed deconvolution method and extract the contribution of the latter phase. On the other hand, for $Ni_{68.8}Fe_{13.2}Si_2B_{16}$ partially crystallized alloy, the proximity of the Curie temperatures of the two phases prevents the assumption of a temperature independent behavior of the nanocrystalline phase, making the deconvolution of the magnetization of the two phases unreliable. As the MC method does not require deconvolution, it can still be applied in that case, as shown in Table 4.2. This is because the transition temperature of the nanocrystalline phase is much higher than that of the amorphous phase and, therefore, the contribution of the nanocrystals to Δs_T is negligible.

4.3 Order of the phase transition and critical composition

The field dependence analyses of MC effect can be extended to FOPT MC materials [71,145]. Even though the results are not related with the critical exponents of the transition, they allow the identification of the order of the thermomagnetic phase transitions and the critical SOPT-FOPT composition (where the order of the phase transition changes from FOPT to SOPT).

For numerical simulations of the MC behavior of FOPT and SOPT materials, B-R model is frequently used in the literature. It has to be noted that though it is based on mean field theories, the qualitative behavior of both SOPT and FOPT MC materials is well described, as we already showed with the analysis of the low-temperature limitation of calorimetric measurements (section 3.3). The aim of this section is to use the model to systematically analyze the possibility of determining the order of the phase transition and the composition of the critical SOPT-FOPT point, in a quantitative way, by studying the field dependence of the MC effect.

Entropy curves as a function of temperature and magnetic field were generated using the parameters of Gd and $LaFe_{11.5}Si_{1.5}$ (representing the examples of SOPT and FOPT MC materials, respectively) for different values of the parameter η. Δs_T and exponent n were calculated from these entropy curves according to Eqs. (1.16) and (1.37), respectively.

Fig. 4.14 shows the temperature dependence of the exponent n for a magnetic field change of 1 T for different values of η using Gd parameters. It is observed that for $T > T_{trans}$ and $\eta \leq 1$ (values to describe SOPT), the exponent n goes smoothly up to the maximum value of $n = 2$ (corresponding to paramagnetic region). This behavior was already observed when using the A-N EOS or the Brillouin function. However, for $\eta \geq 1$ (values to describe FOPT), the exponent n shows an overshoot up to values larger than 2 near the transition temperatures before arriving to the $n = 2$ value of the paramagnetic range. The overshoot values depend on η and the magnetic field change but it is always found to be above 2. This overshoot of the exponent n is shown to be characteristic of FOPT MC materials [145].

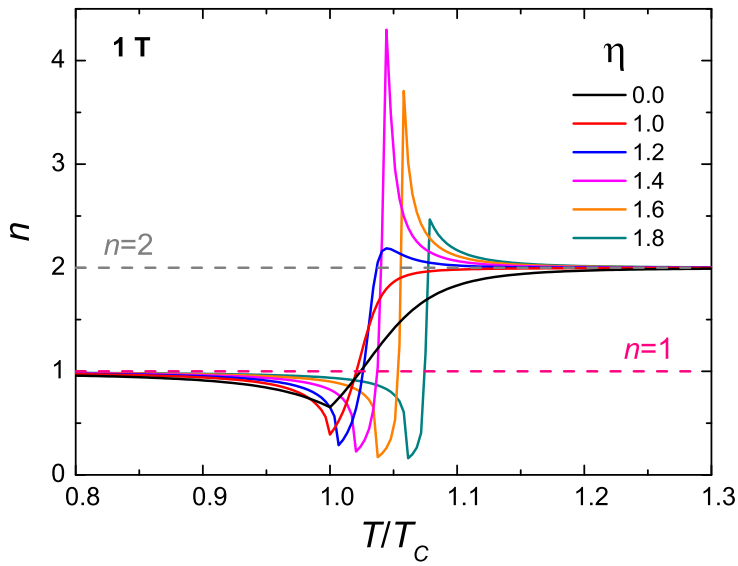

Figure 4.14: Temperature dependence of the exponent n for a magnetic field change of 1 T for different η parameters (Gd parameters).

To analyze the influence of the magnetic field on the exponent n, Fig. 4.15 shows the temperature dependence of n at a fixed value $\eta = 1.4$ using $LaFe_{11.5}Si_{1.5}$ parameters for fields up to 5 T. The exponent n shows an overshoot near the transition temperature followed by a decrease to values close to 2 in the paramagnetic region and this is observed for all the magnetic fields. It has to be noted that the observed characteristic overshoot is independent of the simulation parameters (though the values of the overshoot can differ) but only dependent on the η parameter. The overshoot is observable for all the magnetic fields though the values present a non-monotonous trend. For very high magnetic fields it is expected that FOPT characteristics dissipate and the overshoot would be not observed.

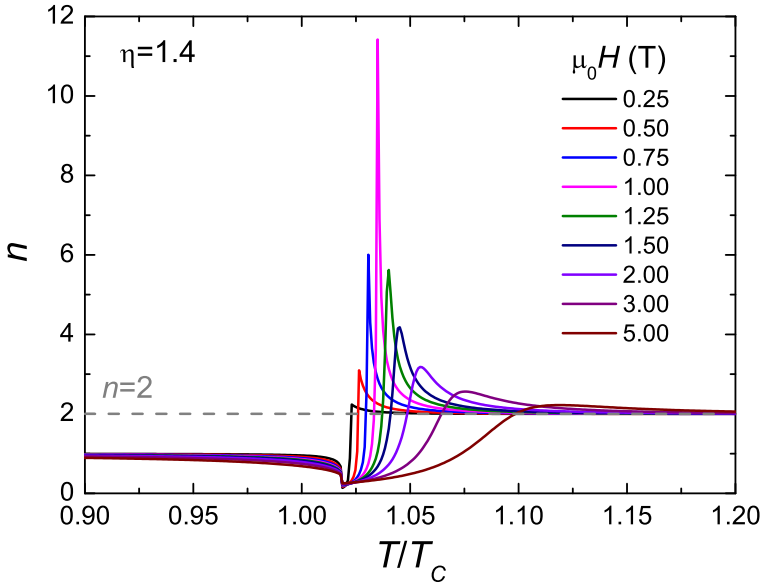

Figure 4.15: Temperature dependence of the exponent n for $\eta = 1.4$ for different magnetic field changes ($LaFe_{11.5}Si_{1.5}$ parameters).

These simulations constituted a firm basis for supporting the new criterion for quantitatively determining the order of thermomagnetic phase transitions, proposed in collaboration with J. Y. Law, which has been successfully applied to different MC materials, such as $La(Fe,Si)_{13}$,

Heusler compounds and composite materials [145]. To show the excellent agreement with experimental results, Fig. 4.16 shows the temperature dependence of the exponent n for a $LaFe_{11.6}Si_{1.4}$ compound for different magnetic field changes. The overshoot is corroborated and, moreover, its field dependence is in an excellent agreement with the simulated results using the B-R model (see Fig. 4.15).

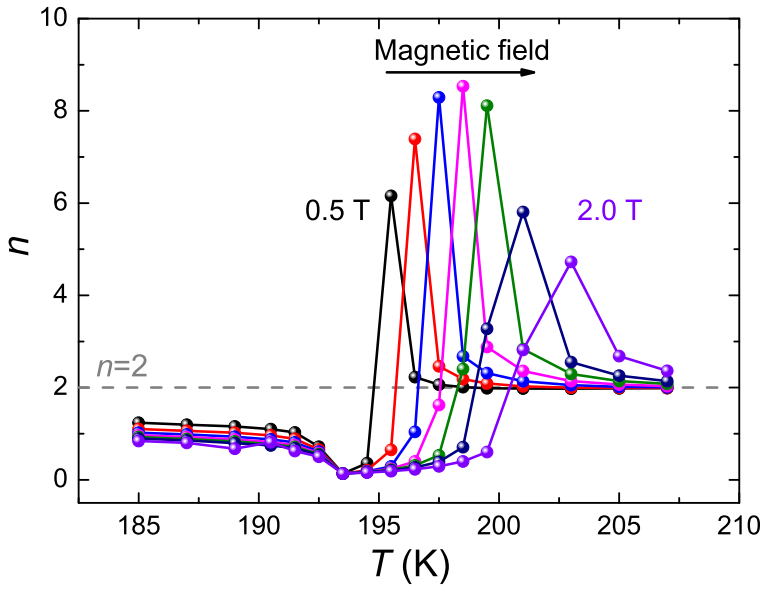

Figure 4.16: Temperature dependence of the exponent n for $LaFe_{11.6}Si_{1.4}$ for different magnetic field changes.

It has to be noted that Heusler compounds cannot be described through the use of the B-R model as they present a magneto-structural transition, however the criterion is shown to be also applicable for these materials. Fig. 4.17 shows the temperature dependence of Δs_T and exponent n for $Ni_{49}Mn_{36}In_{15}$ compound. It can be observed the overshoot above 2 at temperatures below $T_{pk}^{\Delta s_T}$, indicating the FOPT character of the martensitic transition. In addition, abrupt changes of n are observed due to the change of sign of Δs_T (marked with cyan areas) though they do not affect the general conclusions.

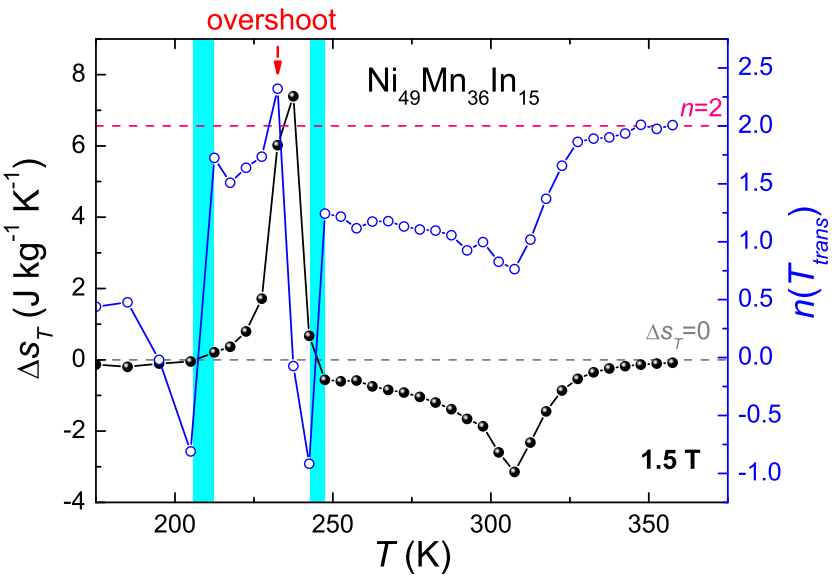

Figure 4.17: Temperature dependence of Δs_T and exponent n for $Ni_{49}Mn_{36}In_{15}$ Heusler alloy at 1.5 T.

Exponent n minima are also observed near the transition temperatures (Fig. 4.14). These minimum values show a clear tendency as η is modified. Fig. 4.18 shows the n values at T_{trans} as a function of η. It can be observed that $n(T_{trans})$ values show a monotonous trend with the η parameter. Two regions and a point can be distinguished: for SOPT region (where $\eta < 1$), $n(T_{trans}) > 0.4$ while for FOPT (where $\eta > 1$), $n(T_{trans}) < 0.4$. For $\eta = 1$, $n(T_{trans}) = 0.4$. The $n(T_{trans}) = 0.4$ value agrees with the theoretical assumptions for the critical point ($\beta = 0.25$ $\gamma = 1$ [146], which lead to $n = 0.4$ according to Eq. (1.38)). Therefore, with the analysis of $n(T_{trans})$ values it is possible to establish another criterion to distinguish between FOPT and SOPT [71]. Moreover, the critical composition of SOPT-FOPT point (FOPT crossovers to SOPT) can be determined when $n(T_{trans}) = 0.4$. The current simulations also give support to that criterion and show the compatibility between both methods. However, it has to be noted that the criterion is limited to materials that follow the B-R model, in contrast with the overshoot criterion.

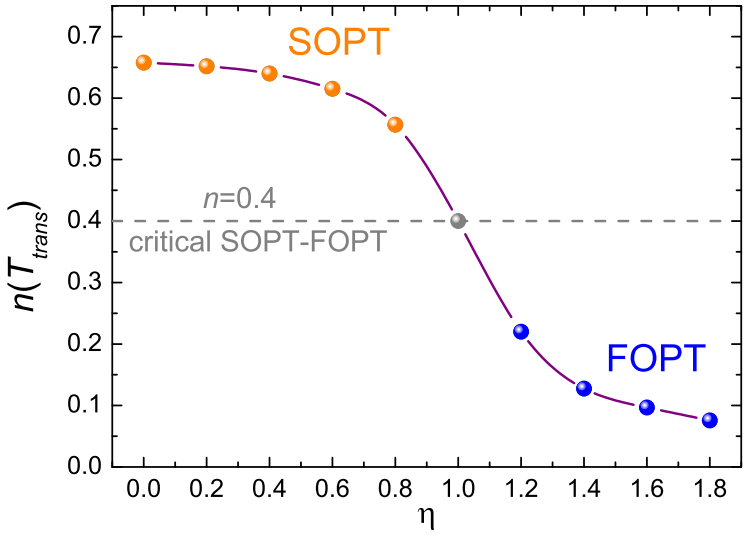

Figure 4.18: $n(T_{trans})$ as a function of the η parameter for 1 T ($LaFe_{11.5}Si_{1.5}$ parameters).

These features will be further discussed when analyzing $La(Fe,Si)_{13}$ compounds in Chapter 6.

4.4 Conclusions

In this chapter, several MC analyses based on the field dependence of the MC effect have been shown as an alternative to conventional methods for getting information on thermomagnetic phase transitions. These allow the determination of the Curie temperature and the critical exponents of SOPT MC materials. Furthermore, the field dependence of MC effect is extended to determine the order of the transition and the critical SOPT-FOPT composition.

The main results are:

- We proposed a method for determining T_C based on the equality of the field dependence exponent n at T_C and that at $T_{pk}^{\Delta s_T}$. The

method was successfully applied to a Fe-based amorphous alloy and numerical simulations. The advantages of the proposed method are:

  - The obtained temperature is field independent.
  - It is not an iterative or a fitting procedure.
  - No assumptions on the critical exponents describing the transition are required.

- The field dependence analysis of MC effect is shown as a precise technique to determine the critical exponents of the phase transition. For a set of Ni-based amorphous alloys, the values of the critical exponents determined from K-F and MC methods are in excellent agreement. The amorphous alloys were then partially crystallized to a biphase material composed by the residual amorphous and nanocrystalline phases. With the MC method, the critical exponents of the residual amorphous phase were determined when the T_C of the crystalline phase is well separated from that of the residual phase (to assume that his MC contribution is negligible) while the K-F method is not applicable. A deconvolution procedure to remove the secondary phase was employed to use the K-F method, which then results in critical exponents that are in good agreement with those from the MC results (that did not require using the deconvolution).

- When field dependence MC analyses are extended to study both FOPT and SOPT MC materials, they provide a powerfull criterion to determine the order of the phase transition and the critical SOPT-FOPT composition. The numerical results simulated from the B-R model were found in an excellent agreement with experimental $La(Fe,Si)_{13}$ results. Two criteria are shown:

  - For FOPT MC materials, the identification of the order of the phase transition is based on the overshoot of exponent n above 2 at temperatures near the transition temperatures. For SOPT MC materials, the overshoot is not observed and the exponent n monotonously increases from $n(T_C)$ up to 2.

– The values of the exponent n at the transition temperature are below 0.4 for FOPT MC materials, above 0.4 for SOPT and exactly 0.4 at the critical SOPT-FOPT point, allowing for the identification of the critical composition.

5 Studies of Gd-based materials

The previously proposed methods for characterizing MC materials are now applied with the aim to optimize their response. In this chapter we will focus on SOPT MC materials. Our aim is attained via two ways: (i) optimizing refrigerant capacity in a multiphase systems or (ii) enhancing magnetic field responsiveness by T_C distributions. Gd was used as the base material for these optimization studies. For the first approach, a series of Gd-GdZn were developed with varying phase fractions. The increased refrigerant capacity of the alloy compared to that of pure Gd is achieved. Assuming a non-interacting model for the phases, our model agrees with the experimental results. Moreover, the proposed procedure to minimize deviations in heat capacity measurements that started from finite temperatures is successfully applied. For the second approach for MC optimization, a Gd/Ti multilayer system with tunable T_C distribution due to the layer thickness was developed, for which an increase of the magnetic field responsiveness of the MC effect is achieved. The results are also found to follow a Gaussian distribution of Curie temperatures.

5.1 Gd-GdZn composites

One approach to optimize the performance of MC materials is to develop composite materials with the appropriate selection of phases and transition temperatures [37, 147, 148]. By appropriately selecting the transition temperatures, these composites can exhibit table-like responses (constant Δs_T values in the operational temperature span), which are highly desired for the Ericsson refrigeration cycle. MC composites have been both theoretically and experimentally shown to exhibit enhanced coefficient of refrigerant performance in comparison to those of single phase MC materials [149]. Their numerical reports show that up to 83 % improved RCP can be possible by proper selection of the composite system: optimum T_C difference of the existing phases and their phase proportions.

As Gd is the paradigmatic SOPT MC material near room temperature, and with the aim to investigate the MC behavior of a multiphase composite, GdZn phase was selected as the other coexisting phase with Gd for the study. With respect to the T_C of Gd (290 K), the GdZn intermetallic compound is relatively near (265 K) and in addition, it is associated with a large MC response. As its binary phase diagram shows that it can coexist with Gd, their composites fulfill the criteria selection of MC composite assembly for RCP optimization. Moreover, unlike others composites, this can be synthesized in a single step. With this, the MC effects of the Gd-GdZn composite materials were studied [150].

5.1.1 Synthesis

Varying phase proportions of Gd-GdZn composites were produced by induction melting $Gd_{50+z}Zn_{50-z}$ (where z = 0, 5, 15 and 25) in an Ar-controlled atmosphere. Both commercial Gd and Zn were 99.9 and 99.98 wt.% pure, respectively. The ingot was melted twice to ensure homogeneity. For comparison, MC effect of pure Gd piece was used as the reference for this work.

5.1.2 Microstructure

Micro-XRD experiments were performed using a Bruker D8 Discover diffractometer. This technique allows to characterize small areas (~ 1 mm^2) of the samples. The micro-XRD patterns of the different produced composites are shown in Fig. 5.1.

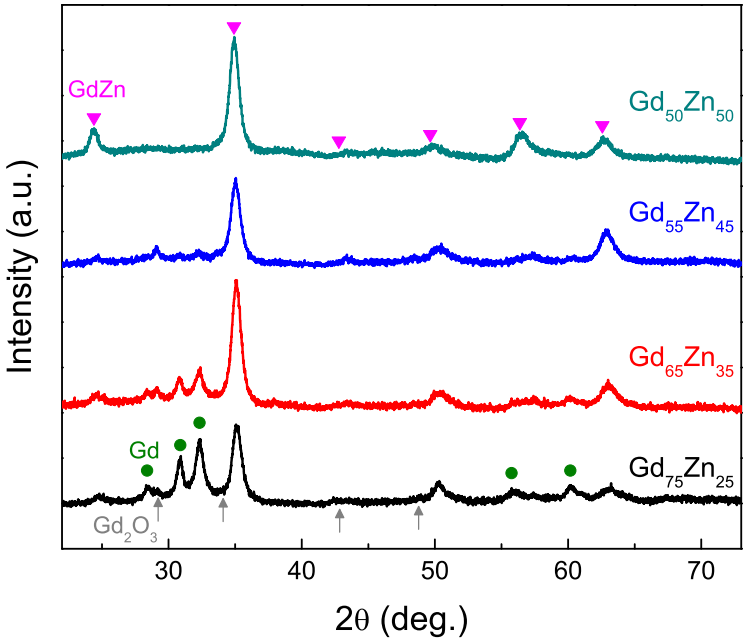

Figure 5.1: Micro-XRD patterns of the Gd-GdZn composites. Circular symbols denote the Gd phase detected while triangles correspond to GdZn. Very minor Gd_2O_3 phase is detected (denoted by the grey arrows).

As expected, the diffraction patterns of the composites can be mainly indexed to Gd (hcp structure), GdZn (CsCl-type structure) and Gd_2O_3 (cubic Ia-3 structure), which is very minor phase. To quantify the different phase fractions presented in the composites, a Rietveld refinement of the patterns was performed. Results of the different phase fractions are shown in Table 5.1. Only 4-8 wt.% of Gd_2O_3 was detected, which can be due to surface oxidation related to the Gd phase (as no oxide phase is observed for the single phase GdZn in $Gd_{50}Zn_{50}$). The refinement results reveal an

increment in the phase fraction of GdZn with Zn concentration, which is in good agreement with the nominal composition.

Nominal comp.	x_{Gd} (wt.%)	x_{GdZn} (wt.%)	$x_{\mathrm{Gd_2O_3}}$ (wt.%)
$Gd_{50}Zn_{50}$	0.0	100.0	0.0
$Gd_{55}Zn_{45}$	7.6	84.7	7.7
$Gd_{65}Zn_{35}$	23.8	70.5	5.7
$Gd_{75}Zn_{25}$	51.0	45.0	4.0

Table 5.1: Phase contents obtained from the Rietveld refinement analyses of the micro-XRD patterns.

5.1.3 Magnetic and MC properties

Δs_T was indirectly calculated from isothermal magnetization curves according to Eq. (1.16) with an initial magnetic field equal to zero. To avoid a relevant influence of the demagnetizing field on the MC determination, the samples were prepared as thin plates for measurements. The temperature dependence of Δs_T for Gd-GdZn composites for 2 T is presented in Fig. 5.2. The results for Gd (also in thin plates) are included as green dashed line. It is observed that the composites show two Δs_T^{pk} values that correspond to the various phases they exhibit for Zn contents up to 35 at. %. They are associated to the T_C of the GdZn and Gd phases at 265 K and 290 K, respectively. Despite that the Δs_T^{pk} of Gd phase for $Gd_{55}Zn_{45}$ is less evident compared to the GdZn, one can still notice small shoulder bump (at temperatures higher than 265 K), which corresponds to the Gd phase. In the case of the $Gd_{50}Zn_{50}$, which exhibits only single phase GdZn intermetallic, only a single Δs_T^{pk} is observed, corresponding to 67 % of that observed for pure Gd (3.2 and 4.8 J kg^{-1} K^{-1}, respectively). This can be expected as nonmagnetic Zn dilutes the behavior of Gd in the GdZn intermetallic like trade-offs in alloys compared to pure Gd. Hence, as the GdZn phase fraction increases (see Table 5.1), the MC response decreases though the values at the peak are similar (around 3.2(0.2) J kg^{-1} K^{-1}) in the range of 265-290 K for the composites. For $Gd_{75}Zn_{25}$ composite

(phase fraction ratio close to 1:1), a table like response is observed as the magnitudes of the Δs_T^{pk} values are almost constant in a temperature span of 25 K (3.1(3) J kg^{-1} K^{-1}).

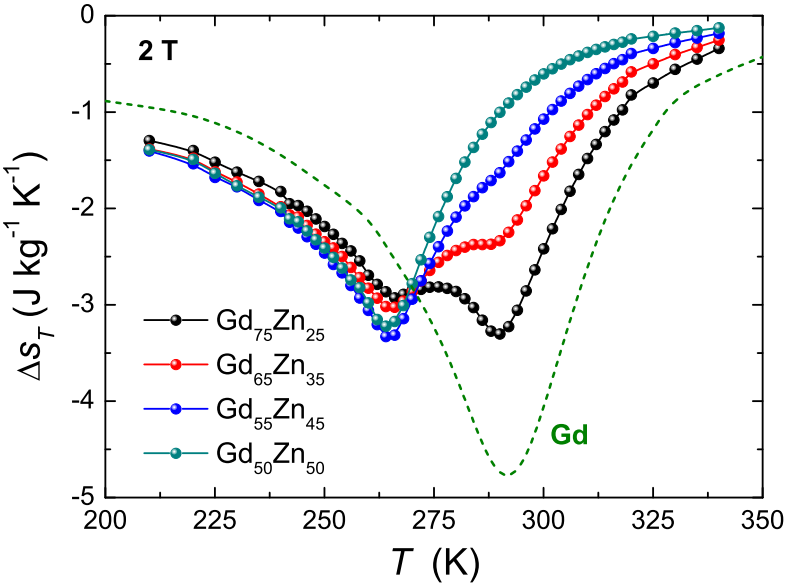

Figure 5.2: Temperature dependence of Δs_T for the Gd-GdZn composites for 2 T (the MC response of pure Gd is shown for comparison).

Assuming a non-interacting phase model for the composites, the total Δs_T can be expressed as:

$$\Delta s_T = x_{\mathrm{Gd}} \Delta s_{T,\mathrm{Gd}} + x_{\mathrm{GdZn}} \Delta s_{T,\mathrm{GdZn}}, \tag{5.1}$$

where x_{Gd} and x_{GdZn} are the Gd and GdZn phase fractions, respectively. $\Delta s_{T,\mathrm{Gd}}$ and $\Delta s_{T,\mathrm{GdZn}}$ are the isothermal entropy changes of pure Gd and GdZn, respectively. It has to be noted that the contribution of the Gd_2O_3 phase ($\Delta s_{T,\mathrm{Gd_2O_3}}$) is not considered as it is Curie-Weiss paramagnet and $\Delta s_{T,\mathrm{Gd_2O_3}} << \Delta s_{T,\mathrm{Gd}}$ and $\Delta s_{T,\mathrm{GdZn}}$ at the studied temperature range. From this, the quantitative phase fractions (or alternatively, the Zn content) can be extracted from the deconvolutions of their various MC responses ($\Delta s_{T,\mathrm{Gd}}$ and $\Delta s_{T,\mathrm{GdZn}}$ are known). This Δs_T deconvolution of

Gd-GdZn composites is presented in Fig. 5.3 (A)-(C). The obtained results show the various contributions arising from the phases exhibited, whereby magenta represents that from GdZn phase and green from Gd phase. This also enabled the determination of the phase proportions in the composites, whereby it is observed that GdZn fraction increases with the nominal Zn content. With these, the Zn content can also be obtained, which is then further compared to those obtained by the Rietveld refinement as shown in Fig. 5.3 (D).

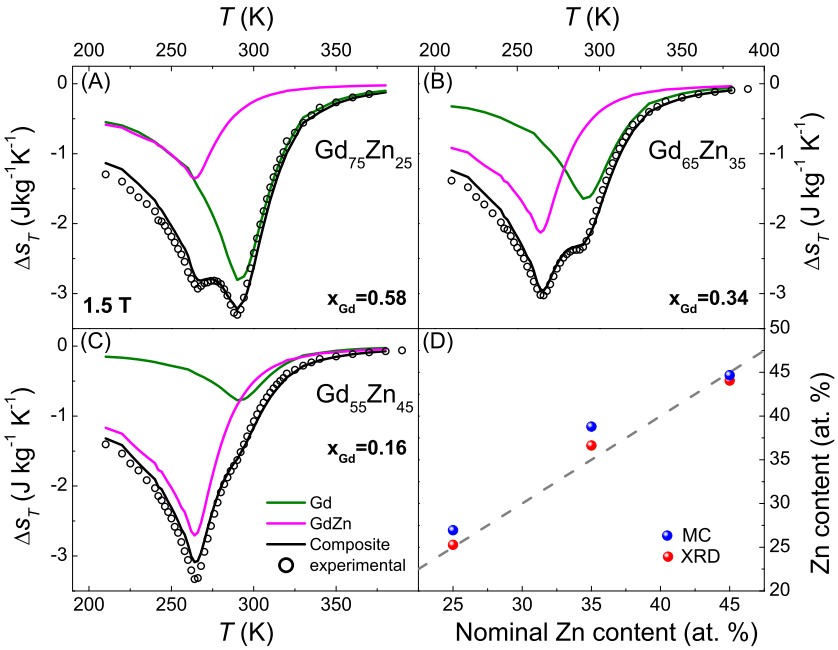

Figure 5.3: Various phase proportions determined from their deconvoluted MC contributions for: $Gd_{75}Zn_{25}$ (A), $Gd_{65}Zn_{35}$ (B) and $Gd_{55}Zn_{45}$ (C). Calculated Zn content from Rietveld refinement and MC analysis vs. nominal composition (D).

As the mass fraction of Gd_2O_3 cannot be obtained by this method, a re-normalization was performed using the values extracted from micro-XRD. The results show that the composites are well represented by this model. The Zn content obtained by the Rietveld refinement and MC analyses show a good agreement. Moreover, they also agree with the

nominal compositions, as the experimental points follow a linear trend with a slope close to 1, as observed in Fig. 5.3 (D). This indicates that the simplified fabrication procedure in this work (only a single step) enables Zn to be fully integrated in the GdZn phase.

To evaluate the MC performance of the composites, the RCP was analyzed. Fig. 5.4 shows the compositional dependence of RCP for the Gd-GdZn series for 2 T

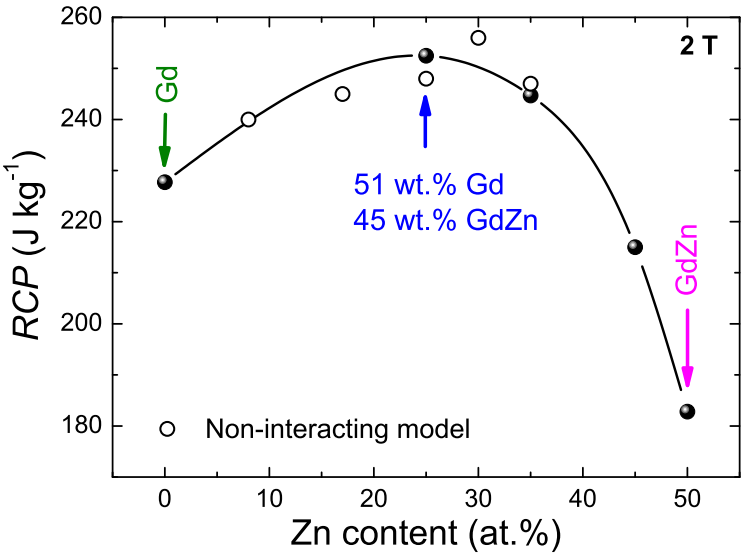

Figure 5.4: Compositional dependence of RCP for the Gd-GdZn series: experimental data (solid symbols) and predicted using a non-interacting model (hollow symbols).

It has to be noted that though the use of RCP is prone to lead to erroneous interpretation of the results in the case of very broad peaks with small magnitude, a valid comparison can be performed for this study since the explored temperature ranges are similar to that of pure Gd. A RCP enhancement is attained by the composites as compared to those of their individual phases (11 % and 45 % when comparing to Gd and GdZn phases, respectively), which could be attributed to their larger temperature spans. The largest RCP value is reached for

$Gd_{75}Zn_{25}$ composite (with 45 wt. % GdZn and 51 wt.% Gd phases) which also corresponds to the one with a table-like Δs_T behavior. It can be observed in Fig. 5.4 that experimental studies for Zn content < 25 at. % are not covered. Hence, to estimate the RCP values in this range, the non-interacting model is used as can reproduce the Δs_T data. The obtained RCP values are plotted in Fig. 5.4 as hollow symbols for which a good agreement with experimental data is observed. From the predicted data, it is observed that the optimal RCP value is obtained for a Zn content close to 30 at.%. This Zn content is close to the 1:1 phase fraction ratio ($x_{\mathrm{Gd}} = x_{\mathrm{GdZn}}$).

The ΔT_S data were determined from the isofield heat capacity measurements. The specific heat capacity data for 0, 1 and 2 T are plotted in Fig. 5.5.

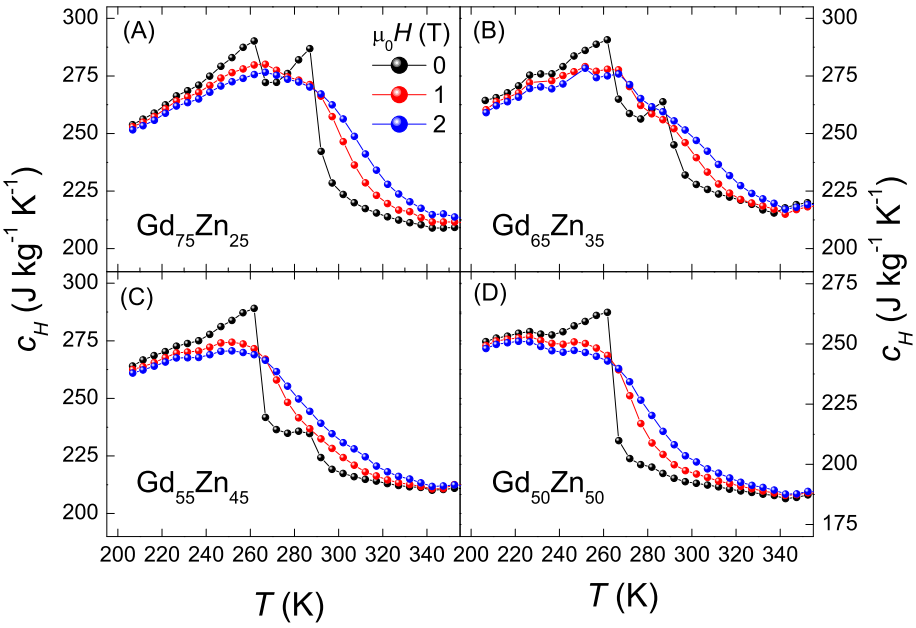

Figure 5.5: Temperature dependence of the molar specific heat for 0, 1 and 2 T for the Gd-GdZn series.

For all biphasic samples (except for single phased $Gd_{50}Zn_{50}$), two abrupt transition peaks are observed for zero field. They become smoother and disappear for higher magnetic fields, according to SOPT characteristics. Moreover, it is observed that $c_H(T)$ data are almost field-independent for 1-2 T even for the temperature region close to the transitions. The observed decrease in c_H values with Zn content (or alternatively, the GdZn phase fraction) can be ascribed to the lower molar mass of the GdZn phase with respect to that of Gd. The calculated data of Δs_T and ΔT_S from these heat capacity measurements was then determined using the earlier proposed method (Section 3.3) [134] as the measurements were performed starting from 200 K, which is close to the T_C of GdZn.

As an example, Fig. 5.6 (A) shows Δs_T^{ap} values for $Gd_{50}Zn_{50}$ composite at temperatures well above the transitions (380 K) for different T_{ini}.

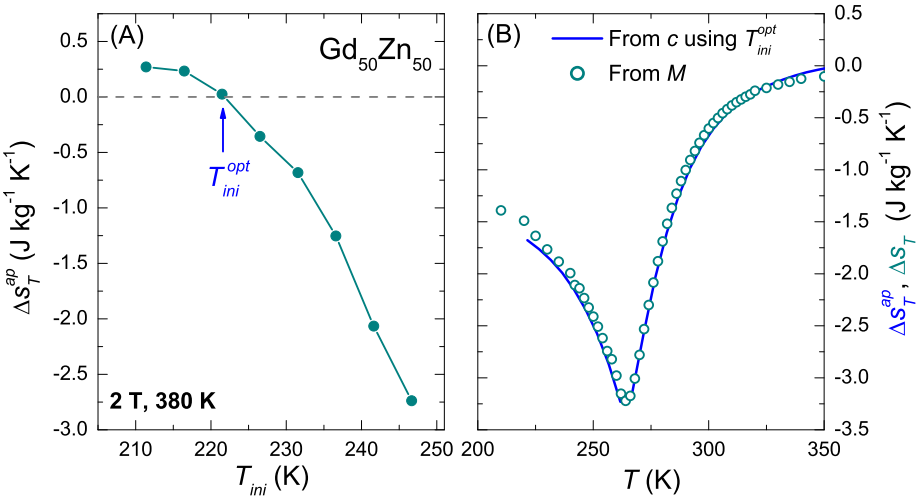

Figure 5.6: Illustration of the previously proposed procedure for MC determination from truncated c_H data with minimal deviations for $Gd_{50}Zn_{50}$. (A): Δs_T^{ap} values for 2 T well above the transition temperatures as a function of T_{ini} to find the optimal T_{ini}. (B): temperature dependence of Δs_T for 2 T obtained by the proposed procedure (line) and from magnetization measurements (hollow symbols).

According to the procedure proposed in Section 3.3, T_{ini}^{opt} with minimal data deviations (i.e. the data calculated using this initial temperature are the same as those integrated from 0 K) are found to be those T_{ini} for which $\Delta s_T = 0$ for $T >> T_C$. From this, $T_{ini}^{opt} = 221.5$ K is found for $Gd_{50}Zn_{50}$. Hence, the temperature dependence of Δs_T determined from c_H measurements was calculated by the proposed method using $T_{ini} = 221.5$ K. The results were then compared with those determined from magnetization data (see Fig. 5.2) and plotted in Fig. 5.6 (B) for comparison. An excellent agreement between both methods is observed. The same was also performed for the other compositions, which further shows that the proposed procedure is applicable to the composite series.

With the obtained T_{ini}^{opt} for each composite, ΔT_S was then calculated according to Eq. (1.3), as depicted in Fig. 5.7.

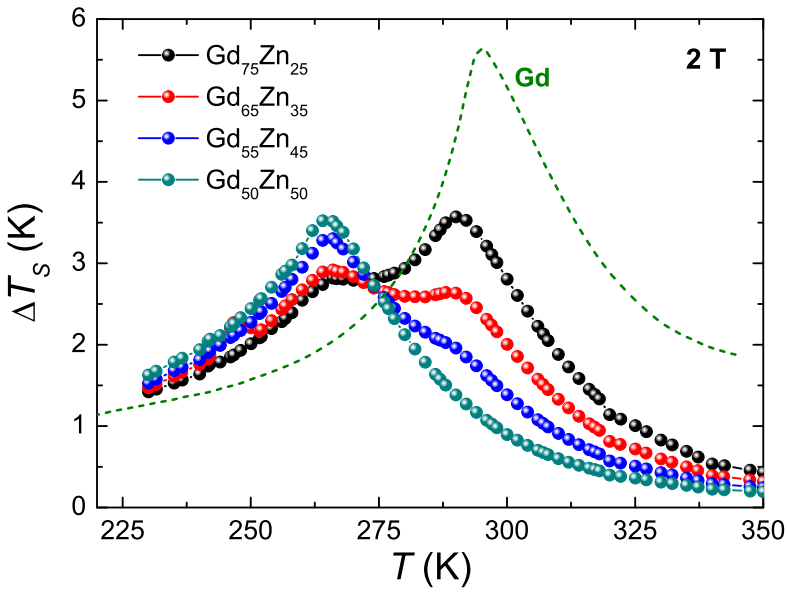

Figure 5.7: Temperature dependence of ΔT_S for 2 T calculated from c_H measurements using the proposed procedure (Section 3.3) for the Gd-GdZn series (MC reponse of pure Gd is shown for comparison).

Similar to the Δs_T behavior, the samples show two peaks corresponding to the presence of the two magnetic phases in the composites for Zn content up to 45 at. % (for $Gd_{55}Zn_{45}$, a small shoulder is observed for its Gd phase). ΔT_S curves show maximum values around 3.3(3) K for all the composites. For $Gd_{50}Zn_{50}$ (100 wt. % GdZn phase), its ΔT_S^{pk} is 62 % of that observed for pure Gd (3.50 and 5.65 K, respectively).

As c_H data are almost field independent for 1-2 T, ΔT_S can be also calculated using Δs_T and c_H data according to Eq. (1.20). It can be observed from Eq. (1.20) that while Δs_T is calculated for a magnetic field change, c_H data appear as a function of a single magnetic field. Hence, c_H data measured for the initial and final magnetic fields (0 and 2 T, respectively) were used for the calculations. Fig. 5.8 shows the temperature dependence of ΔT_S for $Gd_{50}Zn_{50}$ and 2 T calculated from c_H (after applying the proposed procedure) and from Δs_T-c_H combination according to Eq. (1.20).

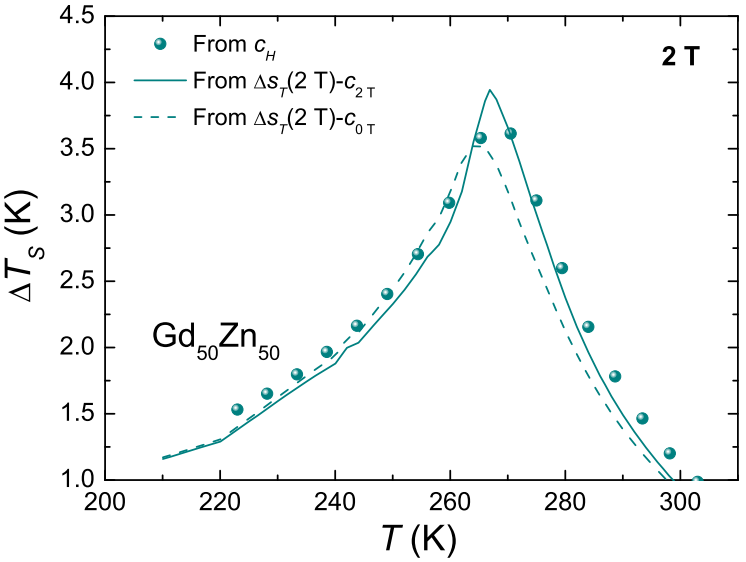

Figure 5.8: Temperature dependence of ΔT_S for 2 T calculated from c_H data and from Δs_T-c_H data combination according to Eq. (1.20) for $Gd_{50}Zn_{50}$.

It can be observed that larger ΔT_S^{pk} values are observed when determined using Δs_T-c_{2T} than those using Δs_T-c_{0T}. The results show a relatively good agreement between the different approximations though differences of $\approx$ 10 % at the peak are clearly observed. It has to be noted that Eq. (1.20) was obtained after strong approximations (mainly that calorimetric data are field independent) and that relatively small differences are acceptable for cases of smooth field dependence of c_H data as compared to other techniques. This approximation will not be recommended for analyzing FOPT MC materials. On the other hand, the proposed procedure from truncated calorimetric data does not assume any approximation and has been experimentally and theoretically validated for both SOPT and FOPT MC materials.

5.2 Gd/Ti multilayers

Besides the RCP optimization by proper selection of phases coexisting in composite materials, other strategy to improve the performance of MC materials is to increase the magnetic field responsiveness of the MC effect [147]. For all temperature ranges, the MC response increases as the magnetic field increases. However, the application in magnetic refrigerator prototypes, when looking for real commercial applications, use permanent magnet arrays as magnetic field generators that, nowadays, can only generate magnetic fields around 2 T [151]. Increasing the field beyond this value can add complications to the design of the device and the associated cost. Therefore, the search for methods (as well as comprehending them) on how to enhance the magnetic field responsiveness of MC materials could eventually lead to newer possibilities in the application of magnetic refrigeration. The actual problem is that the exponent controlling the field dependence of the MC effect has a minimum at the temperature at which the material has the largest response, the transition temperature. One possible way to increase that minimum can be attained by a distributed T_C in the material, which was reported for a Ni-Cu multilayered system

[41]. The T_C distribution arose from the varying composition of each layer, which enhanced its magnetic field dependence of the MC effect as compared to that of the corresponding bulk counterparts. These thin film systems have been studied as MC refrigerants [152] as well as for permanent magnets [153, 154], multiferroic materials [155], etc. With the aim of tuning a distributed T_C by the layer thickness of a multilayer MC material, the magnetic field responsiveness of Gd/Ti multilayered system was studied [156]. The compositions of the layers was not varied but the thickness of Gd layers were varied with the aid of nonmagnetic Ti spacer layers, which was chosen as spacer due to its low solubility in Gd that minimizes intermixing.

5.2.1 Synthesis and microstructure

A Gd/Ti multilayered sample was produced using alternative rf-sputtering deposition of Gd layers and Ti spacers onto glass substrates. Sample fabrication and microstructural characterization were performed by A.V. Svalov and G.V. Kurlyandskaya and more details can be found in [157]. For the sputtering process, a base pressure of $3{\cdot}10^{-7}$ mbar and an Ar gas flow with a pressure of $5{\cdot}10^{-3}$ mbar were used. The deposition rate was about 0.15 nm s^{-1} for Gd and about 0.07 nm s^{-1} for Ti. The deposition times were varied to obtain Gd and Ti layers with thickness (L_{Gd} and L_{Ti}, respectively) of 1.5 and 2 nm, respectively. A total number of 50 layers was chosen, being the sample denoted as $[\mathrm{Ti(2\ nm)/Gd(1.5\ nm)}]_{50}$. The sample has a protective coating Ti(5 nm) layer.

It has to be noted that the mass of the Gd layers for $[\mathrm{Ti(2\ nm)/Gd(1.5\ nm)}]_{50}$ was calculated using the thickness of the layers, the area of the sample and the density of bulk Gd. If the densities of the thin Gd layers are smaller than that of bulk Gd, it is expected to get a smaller error in their mass determination with this method than to take their mass with a mass balance (the substrate has a much larger mass than that of the sample itself). Although this error can produce an

underestimated value of Δs_T, it does not alter its field or temperature dependence. As a reference for this work, Gd (99.9 %) was melt spun into ribbons 20 μm thick and 3 mm wide (to avoid demagnetizing field effects) and the results of multilayered sample were compared to those of Gd ribbons.

Fig. 5.9 shows the low-angle XRD results (performed using a Rigaku D/max-RB) for [Ti(2 nm)/Gd(1.5 nm)]$_{50}$, which clearly show a well-defined layered structure with two distinct diffraction peaks at 2θ = 3.77 and 7.16 °. In agreement to the XRD data, its cross-sectional HRTEM image (characterized using a JEOL JEM-2100 TEM) also reveals well-defined layers (inset of Fig. 5.9).

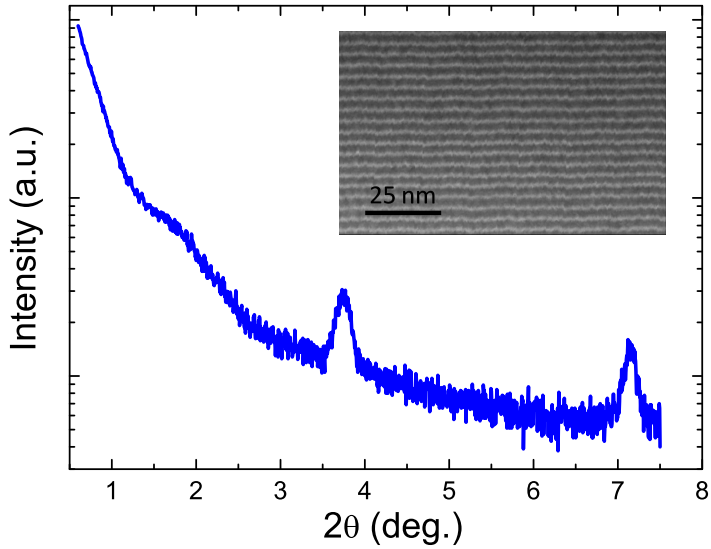

Figure 5.9: Low-angle X ray pattern and cross-sectional HRTEM image (inset) for [Ti(2 nm)/Gd(1.5 nm)]$_{50}$.

5.2.2 Magnetic and MC properties

Fig. 5.10 shows the temperature dependence of σ for a magnetic field of 0.012 T for [Ti(2 nm)/Gd(1.5 nm)]$_{50}$ and the inset shows the thickness dependence of T_C for Gd [158].

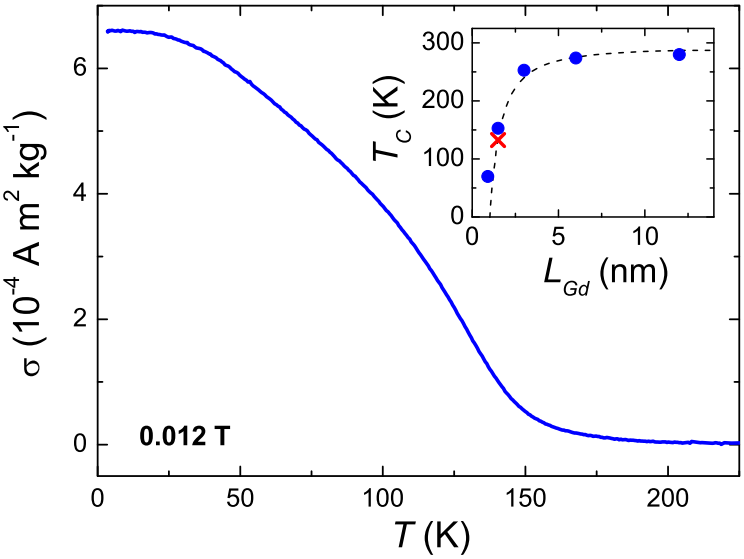

Figure 5.10: Temperature dependence of σ for 0.012 T for $[\mathrm{Ti}(2\ \mathrm{nm})/\mathrm{Gd}(1.5\ \mathrm{nm})]_{50}$. Inset: T_C evolution with respect to the Gd layer thickness: symbols for experimental data while the line represents the power law fit according to [158].

It is observed a smooth decrease of σ values from low temperatures to almost 0 around 200 K, indicating a notable SOPT character. T_C is estimated as 130 K from the inflection point of this σ vs. T curve (red cross in inset of Fig. 5.10). This value is much lower than the one obtained for Gd bulk (293 K) as ascribed to the finite size scaling. For such system, the value of T_C is related to the thickness of the layer (L_{Gd}) by a phenomenological power law previously reported for epitaxial Gd [158]:

$$\frac{T_{C,\mathrm{bulk}} - T_C}{T_{C,\mathrm{bulk}}} \propto L_{Gd}^{-\phi}, \tag{5.2}$$

where $T_{C,\mathrm{bulk}}$ is the Curie temperature of the bulk material and ϕ is a constant. Using the previously obtained T_C value from the inflection point of magnetic data, an estimated L_{Gd} of 1.5 nm is observed, in agreement with the expected value from the deposition time.

Fig. 5.11 shows the field dependence of σ for Gd bulk material (A) and [Ti(2 nm)/Gd(1.5 nm)]$_{50}$ (B). Typical magnetic behavior of the Gd bulk ribbons is observed while that of the [Ti(2 nm)/Gd(1.5 nm)]$_{50}$ is also accompanied by some temperature-independent contributions from the sample holder, glass substrate and Ti spacers (as the sample mass is quite small), which is plotted as a dashed line in Fig. 5.11 (B). As this additional signal does not exhibit a noticeable temperature dependence, the calculation of Δs_T is not affected by this contribution. Furthermore, it is observed that both samples show ferro-paramagnetic behavior with increasing temperatures, wherein this occurs at a lower temperature in the multilayer sample compared to that of the bulk counterpart.

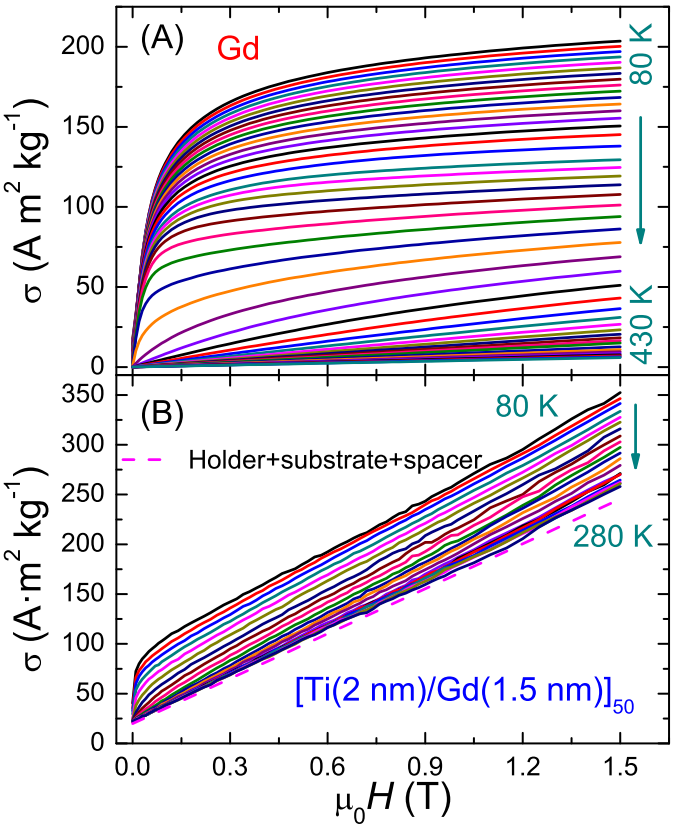

Figure 5.11: Magnetic field dependence of σ for Gd bulk (A) and [Ti(2 nm)/Gd(1.5 nm)]$_{50}$ (B), respectively. Dashed line corresponds to the temperature independent external magnetic contribution.

Fig. 5.12 shows the temperature dependence of Δs_T for Gd bulk and [Ti(2 nm)/Gd(1.5 nm)]$_{50}$ for magnetic field changes of 0.75 and 1.5 T. Comparing both samples, it is observed that the curves for Gd bulk look sharper than those of the [Ti(2 nm)/Gd(1.5 nm)]$_{50}$ (for 1.5 T, Δs_T^{pk} of Gd is -3.5 with narrower temperature width while the latter shows -1.0 J kg^{-1} K^{-1} with broader temperature width).

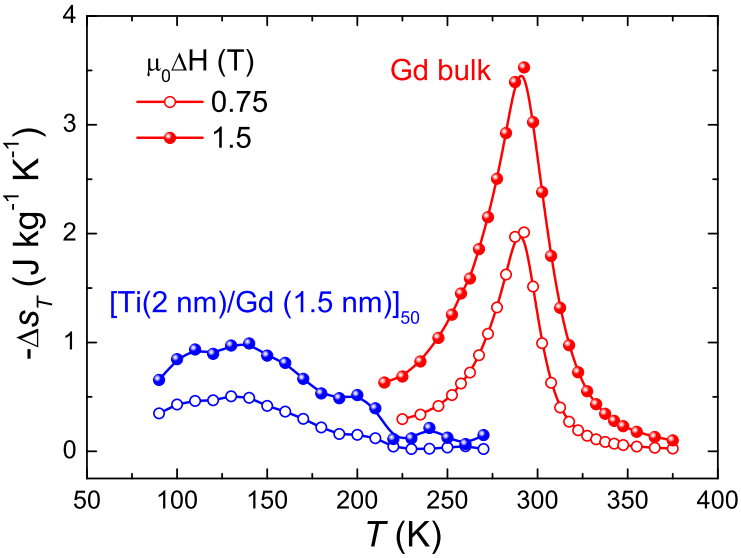

Figure 5.12: Temperature dependence of Δs_T for Gd bulk and [Ti(2 nm)/Gd(1.5 nm)]$_{50}$ for magnetic field changes of 0.75 and 1.5 T.

In general, larger Δs_T responsiveness to magnetic fields for SOPT MC materials occurs at the temperature ranges that they are in fully ferro- or para-magnetic states but having small Δs_T values. This is represented by the field dependence exponent $n(T)$ behavior, wherein shows $n \approx 1$ at the ferromagnetic region and $n \approx 2$ at the paramagnetic range. The lowest field responsiveness of Δs_T is found at the region close to the transition temperature, while Δs_T has a maximum value. Consequently, an increase in n in the region close to T_C can improve the applicability of these MC materials (provided that the magnitude of the MC effect is not reduced). Fig. 5.13 shows the field dependence of Δs_T^{pk} (in a log-log plot) for Gd bulk and [Ti(2 nm)/Gd(1.5 nm)]$_{50}$.

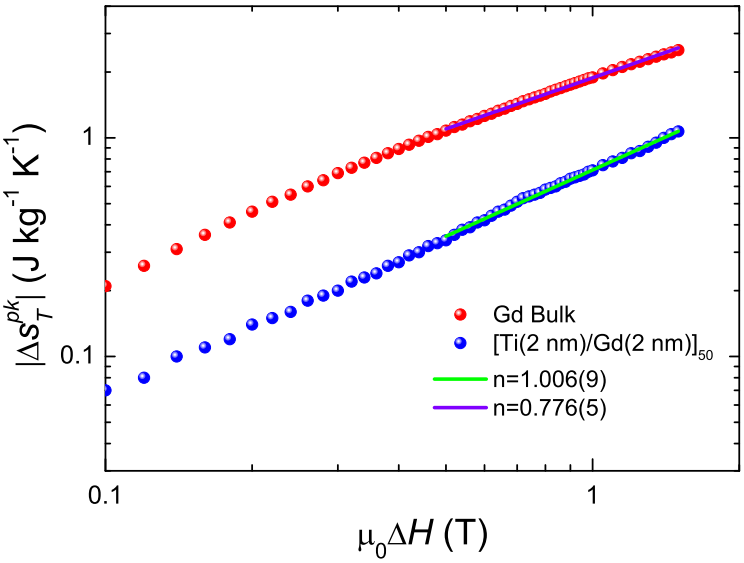

Figure 5.13: Magnetic field dependence of Δs_T^{pk} for Gd bulk and [Ti(2 nm)/Gd(1.5 nm)]$_{50}$.

The value of the slope for the former is 0.776 while that for [Ti(2 nm)/Gd(1.5 nm)]$_{50}$ its slope increases up to 1.006, which indicates that the MC response of this thin film is more field responsive than those of bulk systems (also in agreement with literature). At low magnetic fields, the field dependence deviates from the expected linear behavior in log-log plots due to the multidomain structure of the samples and, therefore, it is not fitted.

For comparing the $n(T)$ behaviors of both samples (shown in Fig. 5.14), a rescaled temperature axis was used since the T_C for both samples are different. The data of Gd bulk have to be corrected for its demagnetizing factor. For bulk Gd, the observed n behavior corresponds to the typical behavior of a single phase SOPT MC material: $n \approx 1$ at $T << T_C$, then decreases to a minimum at T_C and eventually to $n \approx 2$ at $T >> T_C$. The additional peak observed around 235 K can be ascribed to the spin reorientations [159]. On the other hand, for [Ti(2 nm)/Gd(1.5 nm)]$_{50}$, its n behavior differs from that of bulk Gd, in particular the value of $n \approx 1$

in a broad temperature span around T_C (unlike the deep minimum at T_C that is < 1 for Gd bulk). This is in agreement to the n behavior of the Ni-Cu multilayered system with varying compositions in each layer that was reported in literature [41]. In our case this is achieved with a single composition.

To describe the observed MC response of Gd multilayered sample (smeared yet wide Δs_T as compared to that of bulk counterparts), it is assumed that it exhibits a distributed T_C due to finite size scaling that can occur for the varying layer thickness for the studied [Ti(2 nm)/Gd(1.5 nm)]$_{50}$. With this assumption, numerical simulations were also performed. The magnetization of the Gd bulk was modeled using the Brillouin function. For the modeling of the multilayer sample, the previous model of the bulk behavior was modified using a Gaussian distribution of T_C (see Section 3.2). The calculated values of the exponent n at T_C as a function of ω are represented in the inset of Fig. 5.14.

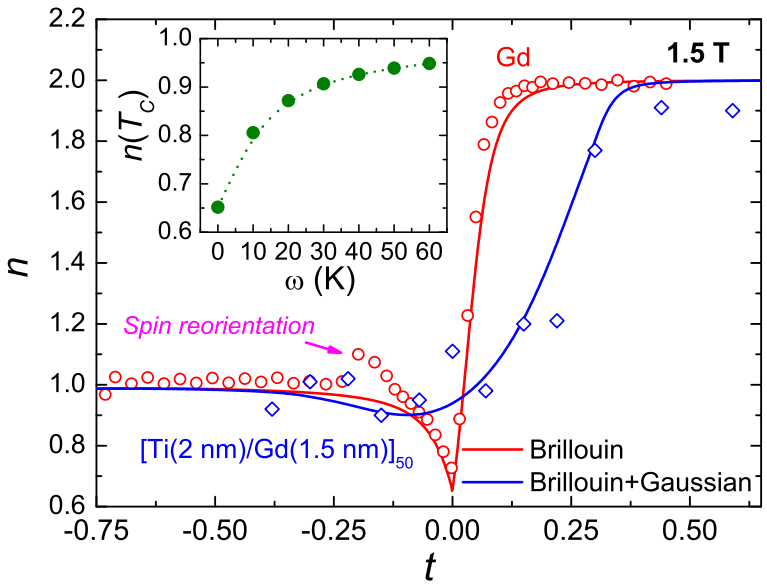

Figure 5.14: Temperature dependence of the experimental and simulated ($\omega = 30$ K) exponent n for Gd bulk and [Ti(2 nm)/Gd(1.5 nm)]$_{50}$ for 1.5 T. Inset: $n(T_C)$ vs. ω.

It is observed that the values of $n(T_C)$ increase as ω increases, reaching values close to the experimental observations (1.0 in main panel of Fig. 5.14) at $\omega \approx 30$ K. This can be ascribed to small differences in the layer thickness, as the addition or subtraction of one atomic layer leads to a variation of T_C around 100 K (see inset of Fig. 5.10), which according to sputtering experiments is reasonable. In the simulations, the obtained $n(T_C)$ values are nearly independent of the temperature range (2Ω) near $\Omega = 2\omega$ (the integrand for values larger than $T_C + 2\omega$ is negligible). In addition, the temperature dependence of the simulated n for Gd bulk and [Ti(2 nm)/Gd(1.5 nm)]$_{50}$ are also included in the main panel of Fig. 5.14, which shows a good agreement with experimental results.

5.3 Conclusions

In this chapter, we have analyzed possible ways for optimization of SOPT MC material systems based on Gd:

- For the RCP optimization of MC materials in composite systems, a series of Gd-GdZn composites (using 25 - 50 at.% Zn content) were successfully prepared in a single synthesis step with a good control of the phase fractions and the element contents. This fabrication route overcame several typical drawbacks, such as multiple preparation steps and poor thermal contact between phases. The samples exhibit a similar table-like Δs_T. This characteristic leads to the enhanced RCP values as those compared to the pure materials: 11 % and 45 % improvement with respect to Gd and GdZn pure phases, respectively. It is shown that Δs_T of Gd-GdZn composites can be modeled by considering non-interacting phases, which further enabled the predictions of the MC behavior for the whole compositional range (i.e. extended to compositions not studied experimentally). From their heat capacity data, a ΔT_S^{pk} of 3-3.5 K for 2 T was obtained for all the composites using different analysis methods described

in earlier chapters. The developed procedure to calculate the MC effect from truncated calorimetric data has been succesfully applied for Gd-GdZn composites, showing a good agreement with those calculated from independent magnetization measurements.

- The field responsiveness of SOPT MC materials is enhanced in a Gd/Ti multilayer system prepared by rf sputtering. Its field dependence exponent of Δs_T is shown to be 30 % larger than that of a Gd bulk (micro-thick ribbons), indicating that the former is more responsive to magnetic fields. It is further shown that this observation can be ascribed to a Curie temperature distribution arising from the small variations in the layer thickness by the order of one atomic layer magnitude. This is also observed for their numerical simulations, in which the multilayered material was reproduced using the Brillouin function to describe each contribution of a Gaussian distribution of Curie temperatures.

6 Studies of La(Fe,Si)$_{13}$-based materials

FOPT MC materials are broadly studied due to their attractive MC responses, which can be larger than those of SOPT type. However, applicability can be compromised by hysteresis. La(Fe,Si)$_{13}$ is a FOPT MC material with large MC response but accompanied by moderate hysteresis, as compared to other materials. In addition, its abundant, non-critical and non-contaminant elemental composition adds on to its character as a promising MC material. Still, it calls for properties optimization if it is going to be used in magnetic refrigerators, such as decreasing hysteresis and/or tuning their transition temperatures to room temperature. We have used two approaches to optimize the response of La(Fe,Si)$_{13}$: reducing the hysteresis arising from FOPT and increasing the FOPT character of the transition. For the former, a reduced hysteresis is clearly attained by Ni additions while, for the second approach, an enhanced FOPT character is attained by Cr addition. These investigations, including both direct and indirect MC measurements of Δs_T and ΔT_S, are further described and discussed in this chapter.

6.1 Ni-doped series

The MC response of $La(Fe,Si)_{13}$ compounds is tunable by the addition of different dopants, mainly rare earth substitution to La [160–162] or transition metals to Fe [163–168]. It was reported that for elements on the left of Fe as positioned in the periodic table, only those exhibiting similar atomic radius as that of Fe shift the transition temperature (around 200 K) to lower temperatures and at the same time induce antiferromagnetic coupling to Fe. Conversely, those on the right side with similar atomic radius tune the transition to higher temperatures producing ferromagnetic coupling to Fe [169]. A significant tuning of the transition temperature to room temperature was found for Co addition [170,171]. However, Co is one of the critical raw elements and the sustainability of critical raw materials has been a global rising concern. This can then poise challenges for upscale fabrication of these compounds for magnetic refrigeration, which impedes MC progressing for commercialization.

Ni has a similar metallic radius to that of Co, which can then serve as an economical choice for substituting Co dopant and at the same time tune the transition temperature in a similar way. Hence, with the aims of reducing hysteresis in $La(Fe,Si)_{13}$ and tuning its transition to room temperature, we have developed a series of $La(Fe,Ni,Si)_{13}$ compounds with varying Ni content and studied for their MC behavior [107].

6.1.1 Synthesis

$La(Fe,Si)_{13}$ compound with nominal composition of $LaFe_{11.6}Si_{1.4}$ was chosen as the parent composition as it undergoes a FOPT [71, 172]. The varying Ni additions in nominal composition $LaFe_{11.6-x}Ni_xSi_{1.4}$ were selected from x = 0 up to 0.4. In order to avoid the incorporation of oxides originated from raw elemental pieces, La was initially cleaned by arc melting and surface polishing. The elements were then induction melted to ingots, which were further annealed at 1050 °C for 3 h (encapsulated

in quartz tubes under Ar atmosphere) for improved homogeneity. The annealed ingots were next segmented into different pieces for subsequent suction casting (with a rectangular mold of 10×4×0.5 mm^3). A 9 wt.% excess of La was also added in the initial element mixture to compensate its vaporization during the different melts. Suction casted samples (wrapped in Ta foil and sealed in quartz tubes under Ar atmosphere) were annealed in a electric resistance tube furnace at various temperatures and durations to obtain high phase fractions of the desired $NaZn_{13}$-type phase (denoted as 1:13 from now) and then water quenched.

6.1.2 Microstructure

Firstly, optimal phase fraction of 1:13 phase had to be attained, which was performed by optimizing the annealing profiles of the pristine and Ni-doped samples. For that, their microstructures were characterized to identify the presence of the phases formed upon annealing. It is found that the annealing duration of one to two days is enough sufficient for reaching an stable phase formation. It has to be noticed that, in comparison to the as-melted counterparts (prior to suction casting), the annealing profile is drastically reduced from weeks to merely up to two days. This is ascribed to the low dimensionality of the suction casted samples compared to those of the as-melted ones and to a better compositional homogenization (in the case of ribbons obtained by melt spinning, the annealing duration is reduced to hours [173]). With the annealing duration optimized (one day), the different doped samples of varying Ni content were annealed at different temperatures to obtain a high fraction of the desired 1:13 phase. Fig. 6.1 shows the BSE images of the sample with the highest Ni content (nominal x = 0.4) after annealing one day at 1060 °C, 1100 °C and 1160 °C. Bright spots indicate the $La_1Fe_1Si_1$ phase (P4/nmm), dark ones correspond to α-Fe phase (Im-3m) and the grey to the desired 1:13 phase (Fm-3c). This was verified by EDX and XRD.

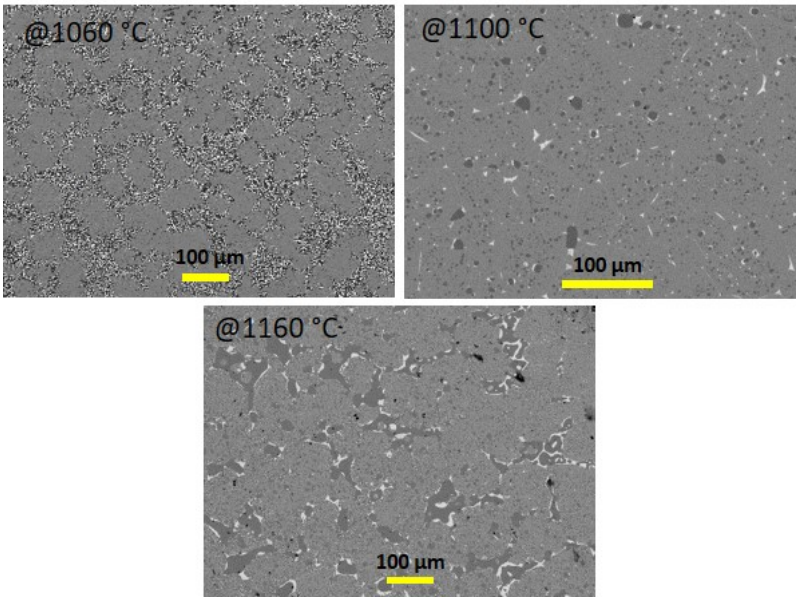

Figure 6.1: BSE images of the highest Ni-doped sample (nominal x = 0.4) annealed for 1 day at 1060 °C, 1100 °C and 1160 °C.

It can be observed that 1100 °C is the optimal annealing temperature for Ni-doped $La(Fe,Si)_{13}$, which is the same for the pristine compound, as its BSE image shows the least amount of secondary phases. For an annealing temperature of 1060 °C, the sample exhibits large amounts of $La_1Fe_1Si_1$ dentrites and α-Fe. For the annealing temperature of 1160°C, $La_1Fe_1Si_1$ degenerates into granular particles that surround α-Fe, as previously observed [174]. It is also noticed that this highest Ni-doped sample shows a higher concentration of secondary phases than those of the parent composition. Further attempts of optimizing the annealing profile of this Ni-doped sample for improving the 1:13 phase fraction were also carried out (for e.g. 1075 °C for two days) but to no avail. This can indicate a solubility limit of Ni in the 1:13 phase.

From the annealing profile optimization performed before, the Ni-containing compounds were annealed at 1100 °C for one day. Their BSE images in Fig. 6.2 show a homogenous structure with a main phase

corresponding to the desired 1:13. The different samples are now denoted by their Ni content in the 1:13 phase determined by EDX (x = 0.00, 0.10, 0.18, 0.26, 0.33).

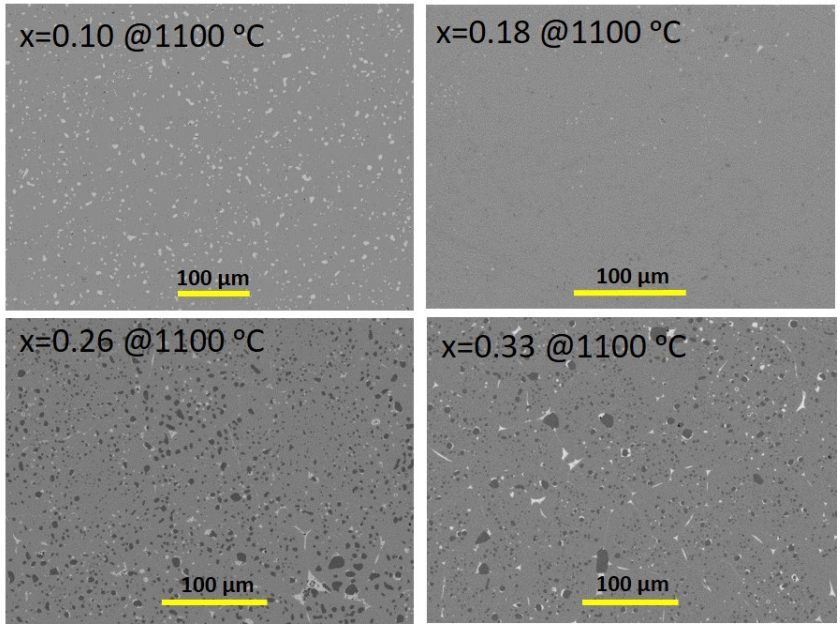

Figure 6.2: BSE images of the Ni-doped La(Fe,Si)$_{13}$ series annealed at 1100 °C for 24 h.

Almost negligible α-Fe impurities were observed for low Ni contents, i.e. nominal x = 0.1 and 0.2, though minor amount of α-Fe was reported for similar alloys [171]). Some bright spots of $La_1Fe_1Si_1$ phase can be noticed, which could be due to the excess La added in the initial mixture. However, this phase is more preferred to the formation of α-Fe. The dark spots, corresponding to α-Fe, become more noticeable with increasing Ni concentration for higher Ni content (nominal x = 0.3 and 0.4) though still attaining a high amount of 1:13 phase. Detailed compositional analysis of the 1:13 phase of the Ni-doped samples was further studied using EDX. Table 6.1 shows the composition of the 1:13 phase determined from the EDX results for each sample. A good agreement between the measured and nominal compositions is observed, only very slight deviations can

be found for samples with higher Ni content. Considering the obtained compositions and the presence of secondary phases, the series shows a solid solutbility limit of ~ 0.3, which is a 1.4-fold extension compared to literature [171]. When the incorporation of Ni in the 1:13 matrix becomes challenging, a slight increment of the Si amount is observed. However, it has to be noted that though Si content has increased, it still does not exceed the critical SOPT composition point of 1.65 [71].

Fig. 6.3 shows the XRD spectra for the Ni-doped series.

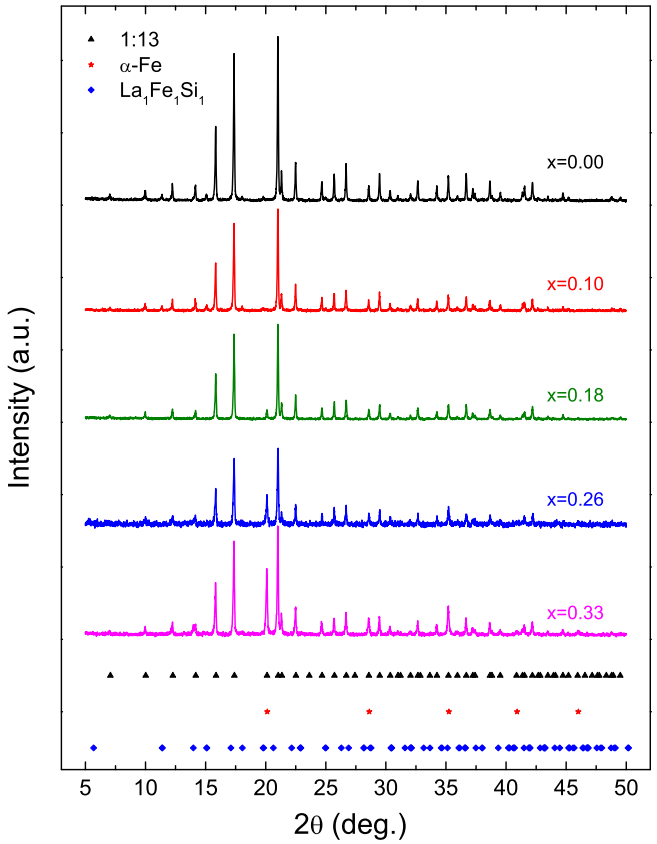

Figure 6.3: XRD spectra for the Ni-doped $La(Fe,Si)_{13}$ series.

It is also observed that the samples mainly consist of 1:13 phase despite of minor traces of α-Fe and $La_1Fe_1Si_1$ detected, which are in agreement

with results obtained from EDX and BSE. The results from the Rietveld refinement of the different XRD spectra, including phase fractions, lattice parameter of 1:13 ($l_{1:13}$) and the goodness of fit (GoF), are tabulated in Table 6.1, in which GoF values close to 1 (ideal case) for all samples are observed [175]. The amount of α-Fe increases with Ni content, showing a large increment for x = 0.26, which are consistent with the EDX, BSE and XRD results. It is observed that though Ni additions do not modify the $NaZn_{13}$-type structure, the lattice parameter decreases with increasing Ni content at a rate of -0.0018(6) Å (at.% Ni)$^{-1}$ [107].

Sample	1:13 phase composition	$x_{1:13}$ (wt.%)	$x_{\alpha-Fe}$ (wt.%)	$x_{La_1Fe_1Si_1}$ (wt.%)	$l_{1:13}$ (Å)	GoF
x = 0.00	$La_{1.00(3)}Fe_{11.2(4)}Si_{1.45(12)}$	97.9	0.2	1.9	11.49043(13)	1.35
x = 0.10	$La_{1.00(3)}Fe_{11.2(2)}Ni_{0.10(2)}Si_{1.42(12)}$	96.9	0.9	2.3	11.49179(16)	1.17
x = 0.18	$La_{1.00(3)}Fe_{11.1(2)}Ni_{0.18(3)}Si_{1.44(12)}$	96.2	3.8	0.0	11.48836(15)	1.26
x = 0.26	$La_{1.00(3)}Fe_{10.9(2)}Ni_{0.26(3)}Si_{1.50(12)}$	84.9	14.2	0.9	11.4884(3)	1.01
x = 0.33	$La_{1.00(3)}Fe_{10.9(2)}Ni_{0.33(3)}Si_{1.54(12)}$	77.6	21.3	1.1	11.4857(5)	1.10

Table 6.1: 1:13 phase composition determined by EDX, phase fractions, $l_{1:13}$ and GoF from Rietveld refinement of the XRD spectra of the Ni-doped La(Fe,Si)$_{13}$ series.

To determine the preferential incorporation of Ni in the various phases existing in the samples, the Ni/Fe ratio of the various existent phases for the samples with high Ni content (x = 0.26 and 0.33) are tabulated in Table 6.2.

Sample	Ni/Fe nominal	Ni/Fe (1:13)	Ni/Fe (α-Fe)	Ni/Fe ($La_1Fe_1Si_1$)
x = 0.26	0.0265	0.024	0.012	0.44
x = 0.33	0.0357	0.030	0.014	3.55

Table 6.2: Ni/Fe ratio determined by EDX for the different phases presented in the higher Ni-doped La(Fe,Si)$_{13}$ samples (x = 0.26 and 0.33).

The results show that the Ni/Fe ratio is higher in the $La_1Fe_1Si_1$ phase than those in α-Fe and 1:13 phases, indicating a preferential segregation of Ni in La-rich phase.

6.1.3 Magnetic and MC properties

Fig. 6.4 shows the temperature dependence of the normalized magnetization (with respect to the magnetization value at 150 K) for an applied field of 0.05 T (A) together with T_{trans} (B) and thermal hysteresis (ΔT_{hyst}) (C) as functions of the Ni content for the set of Ni-doped La(Fe,Si)$_{13}$ series.

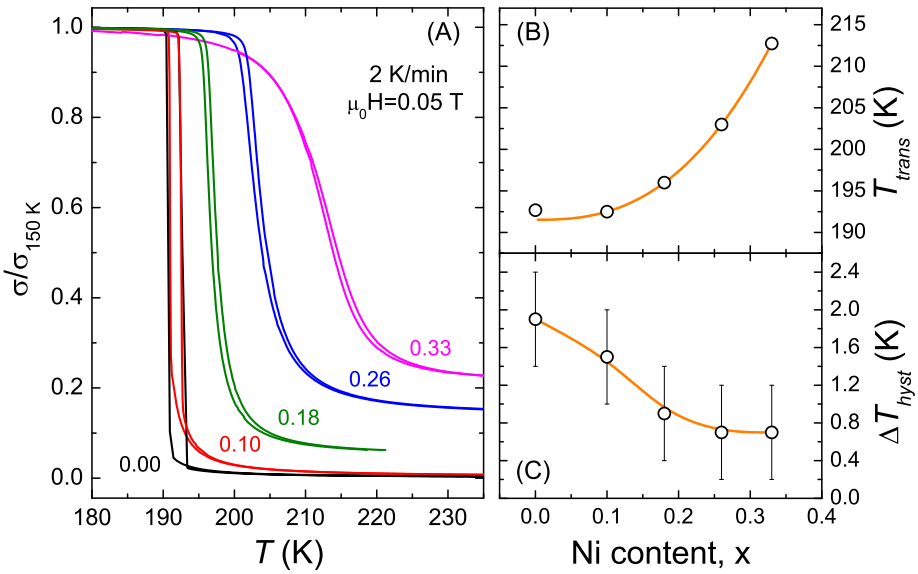

Figure 6.4: Normalized magnetization (with respect to the value at 150 K) for 0.05 T (A), T_{trans} (B) and ΔT_{hyst} (C) as a function of Ni content for the La(Fe,Ni,Si)$_{13}$ series.

A correction for the temperature is needed in order to remove thermal lag at that heating/cooling rates ($\approx$ 1.25 K for each curve). T_{trans} is determined as the temperature for which dσ/dT is maximum. From the normalized representation, it is possible to quickly estimate the amount of α-Fe from the high temperature magnetization, in good agreement with those obtained from the Rietveld refinement of XRD spectra. It can be observed that T_{trans} phenomenologically follows a monotonous increase with increasing Ni content (fitted to a power law of the form

$T_{trans} = \kappa^{(0)} + \kappa^{(1)} \mathrm{x}^{\kappa^{(2)}}$ with $\kappa^{(0)} = 192.6(5)$ K, $\kappa^{(1)} = 159(17)$ K, $\kappa^{(2)} = 2.19(13)$). It can be observed that ΔT_{hyst} is reduced with increasing Ni concentration, reaching a minimum value for x = 0.26 (further discussed later in this chapter). Spontaneous magnetization values of the 1:13 phase for the different samples are slightly modified with Ni additions. Removing the contribution of the α-Fe phase from σ vs. H (not shown) (from the fitting of the paramagnetic tail, as it was shown previously in Fig. 4.12) a decrease of σ_S values at rates of ≈ 7 A m^2 kg^{-1} (at.% Ni)$^{-1}$ is observed, although the presence of α-Fe prevents any further analysis.

As FOPT MC materials exhibit thermal and magnetic hysteresis, discontinuous measurement protocols have been applied for both Δs_T, by indirect measurements, and ΔT_S, by direct measurements. Fig. 6.5 shows the continuous and discontinuous Δs_T measurements from isothermal magnetization curves. The characteristic artifact is observed for the continuous case, while it disappears for the discontinuous. It has to be stressed that the influence is quite notable though the hysteresis of the sample is relatively small.

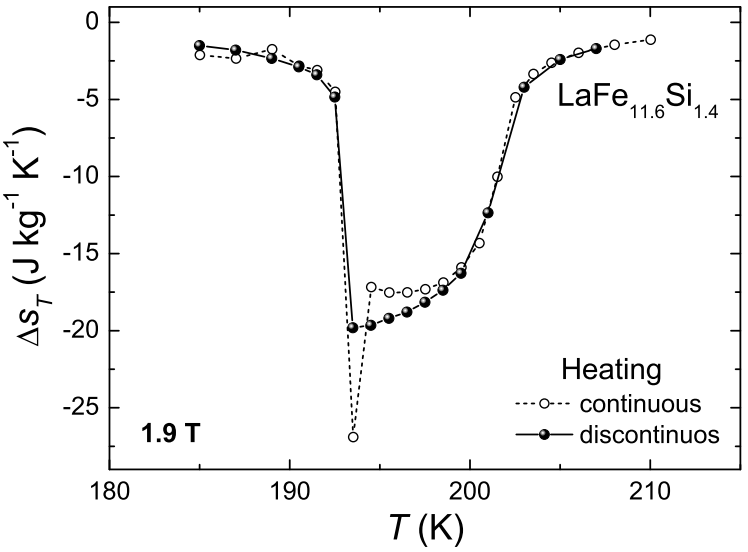

Figure 6.5: Δs_T continuous and discontinuous measurement of the $LaFe_{11.6}Si_{1.4}$ compound.

Fig. 6.6 shows the temperature dependence of Δs_T and the Ni-content dependence of $|\Delta s_T^{pk}|$ for a magnetic field change of 1.9 T for Ni-doped La(Fe,Si)$_{13}$ series calculated from $\sigma_T(H)$ measurements according to Eq. (1.16) while heating. A monotonic decrease of $|\Delta s_T^{pk}|$ with the Ni content is observed, at a rate of -7.0(7) J kg^{-1} K^{-1} (at.% Ni)$^{-1}$. In addition, the corresponding temperatures of the peak shift to higher temperatures with Ni addition, while the curves become broader (ΔT_{FWHM} varies from 8.6 to 25.7 K for the samples with x = 0.00 and 0.33, respectively). Moreover, ΔS_T curves for x = 0.00 and x = 0.10 (despite the slight reduction in magnitude for the latter) maintain an abrupt low temperature increase that change into a gradual type for higher Ni content (x > 0.18) although it can be observed that x = 0.18 sample is an intermediate case.

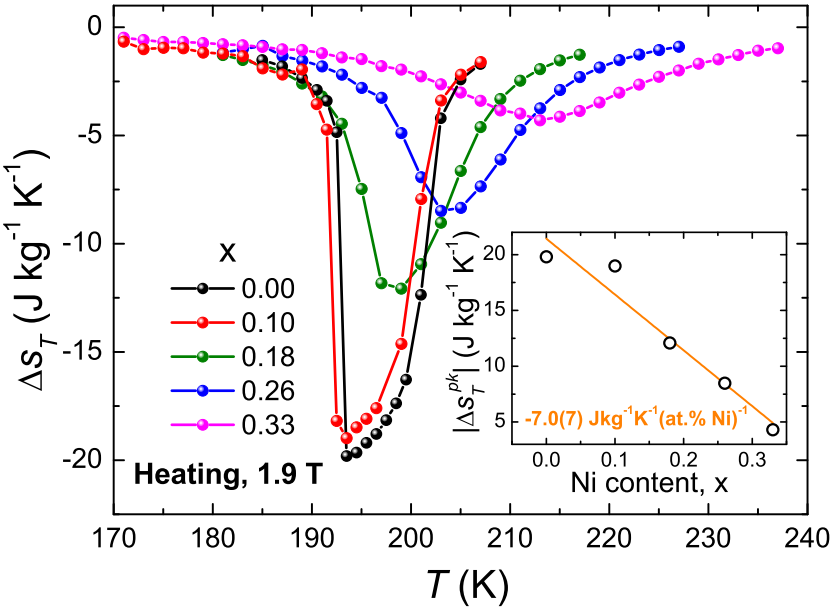

Figure 6.6: Temperature dependence of Δs_T for 1.9 T while heating for the Ni-doped La(Fe,Si)$_{13}$ series. Inset: $|\Delta s_T^{pk}|$ as a function of Ni content.

The effect of the demagnetizing field has been checked. The demagnetizing factor has been determined from σ vs. H_{app} curves at low fields and

temperatures well below the transition. For x = 0.00 sample, N_D is estimated as 0.0927(3) which should be similar for all the samples, as the geometry of the different samples is the same. Fig. 6.7 shows the effect of considering the demagnetizing field over Δs_T and exponent n (inset) for parent $LaFe_{11.6}Si_{1.4}$ compound. The recalculation of Δs_T values considering the internal field instead the applied one shows a 2 % difference at the peak value, having no influence over the analysis performed. In the case of the exponent n, a notable influence of the demagnetizing field in the ferromagnetic range (as for SOPT MC materials) is observed while the differences are negligibles at the transition temperature.

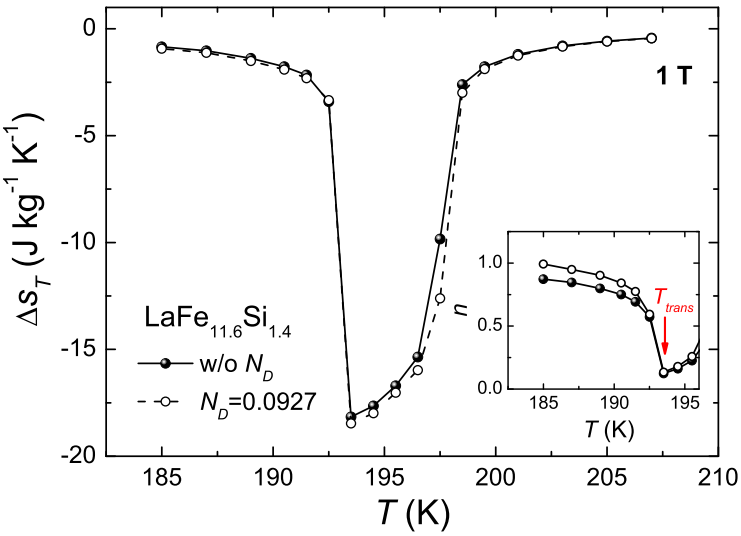

Figure 6.7: Temperature dependence of Δs_T and exponent n (inset) for $LaFe_{11.6}Si_{1.4}$ compound considering the applied (solid symbols) and internal (using $N_D = 0.0927$, hollow symbols) field of 1 T.

Fig. 6.8 shows the temperature dependence of ΔT_S and the Ni-content dependence of the peak (ΔT_S^{pk}) for the Ni-doped series while heating. Similar features as those observed for Δs_T are obtained: the shape of $\Delta T_S(T)$ curves become gradual for x > 0.18 (for x = 0.10, a similar shape to that of the x = 0.00 sample is obtained), the ΔT_S^{pk} values are reduced at a rate of -1.81(10) K (at.% Ni)$^{-1}$, the peak is shifted to higher

temperatures with Ni additions, and the FWHM of the peak increases with Ni content (from 5.3 to 25.7 K for x = 0.00 and 0.33 samples, respectively).

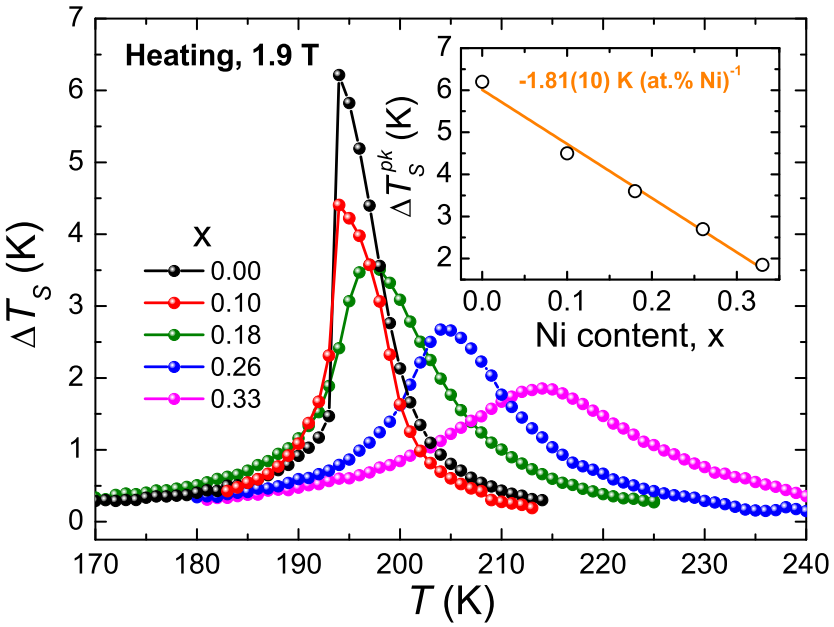

Figure 6.8: Temperature dependence of ΔT_S for 1.9 T while heating for the Ni-doped La(Fe,Si)$_{13}$ series. Inset: ΔT_S^{pk} as a function of the Ni content.

To estimate the cooling power of the samples, CRP_{min} was calculated according to Eq. 1.23. Fig. 6.9 shows CRP_{min} as a function of the Ni content for the series. The CRP_{min} value decreases with Ni addition (from CRP_{min}=3.1 to 0.2 for x = 0.00 and 0.4 samples, respectively). This decrease cannot be ascribed to the presence of α-Fe observed for higher Ni content samples since the α-Fe transition is well above that of 1:13 phase and its mass fraction is not enough to explain the drastic decrease. It should be noted that this tendency is also observed when comparing RCP for the different compositions. In addition, as both experimental and DFT calculations [107] show no drastic modification of magnetization with Ni additions, the alteration of the nature of the phase transition could arise as responsible for this change, which is also compositional dependent.

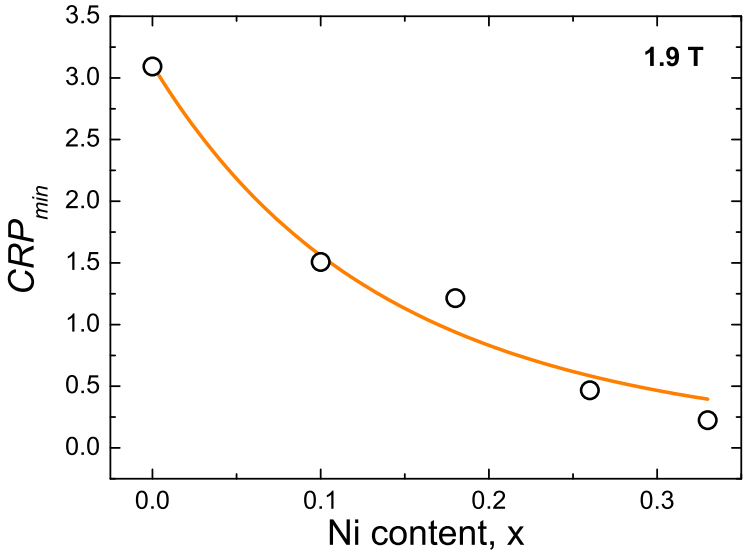

Figure 6.9: Ni content dependence of the minimal coefficient of refrigerant performance for the Ni-doped La(Fe,Si)$_{13}$ series.

To analyze the characteristics of the phase transition ascribed to the MC response of the 1:13 phase, the MC field dependence analyses presented in Section 4.3 have been used. On the one hand, the analysis of the overshoot in the temperature dependence of exponent n is performed. Fig. 6.10 shows the temperature dependence of exponent n for a magnetic field change of 1.9 T. Overshoots of n near the phase transition for x = 0.00, 0.10 and 0.18 samples are observed, which indicate that they undergo a FOPT. It can be also observed that the magnitude of the overshoot is decreasing as the Ni content increases, indicating that the FOPT-character is also decreasing. x = 0.18 should be very close to the composition corresponding to the critical SOPT-FOPT point. On the other hand, for higher Ni-doped samples it is observed a gradual increase from the minimum towards a maximum value at the paramagnetic region, indicating SOPT behavior. It can be noticed that the presence of α-Fe can modify the values of n above T_{trans}, reducing the expected value for the 1:13 single phase [130]. This fact does not modify the procedure as the overshoot above 2 is observed although when impurities are present [145].

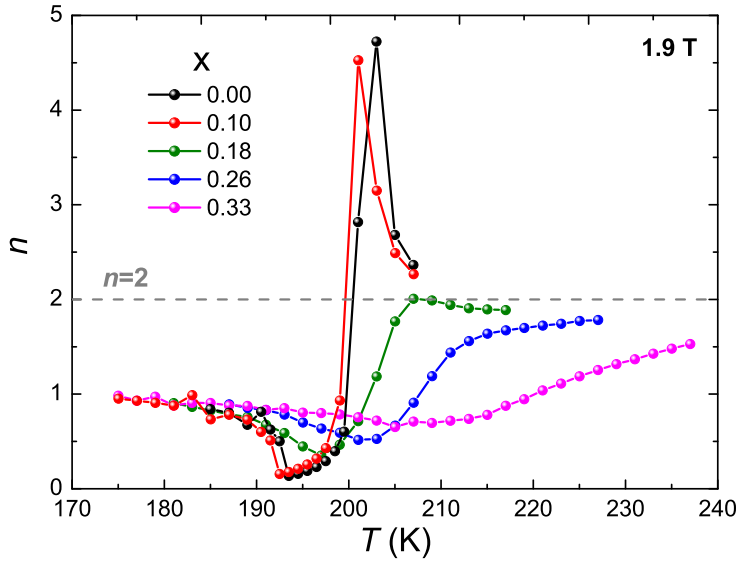

Figure 6.10: Temperature dependence of the field dependence exponent n for the Ni-doped La(Fe,Si)$_{13}$ series.

In addition, the analysis of the exponent n values at the transition is performed. Fig. 6.11 shows the $n(T_{trans})$ as a function of Ni content. It can be observed that x = 0.00, 0.10 and 0.18 samples show $n(T_{trans}) < 0.4$ values, indicating they undergo a FOPT. $n(T_{trans})$ values above 0.4 are obtained for x = 0.26 and 0.33 samples, indicating they undergo SOPT. These results are in agreement with the previous MC analysis. Moreover, this procedure allows to calculate the critical SOPT-FOPT composition. For the studied case, it is predicted for a Ni content x = 0.19 (where it is assumed a linear interpolation between the different points). An excellent agreement with numerical calculations using the B-R model can be observed (see Fig. 4.18). For samples with $LaFe_{11.5-x}Ni_xSi_{1.5}$ compositions, it was reported that their critical SOPT-FOPT composition coincides with a Ni content of x = 0.08 [171], which is a smaller limit compared to our case, though the procedure used by the other authors was less quantitative. Hysteresis results (Fig. 6.4 (C)) follow a complementary trend of those of $n(T_{trans})$, indicating that the reduction of the hysteresis is produced by the reduction of the FOPT character by Ni doping. This is

produced with a very minor modification of the T_{trans} and σ in comparison to similar elements as Co [163, 164, 167].

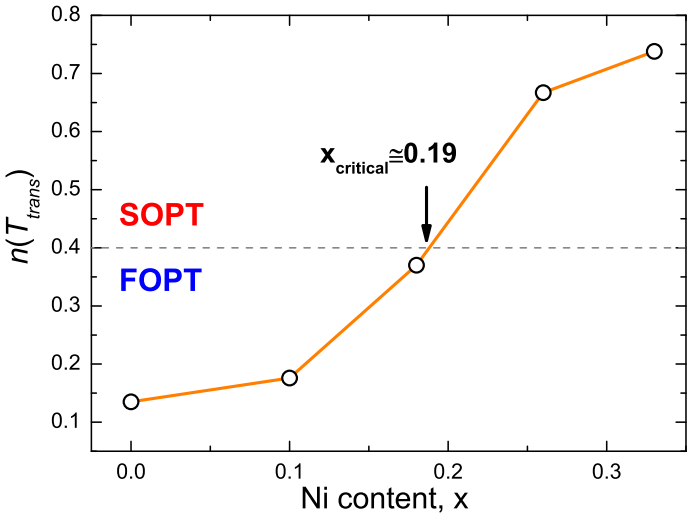

Figure 6.11: $n(T_{trans})$ values as a function of Ni content for the Ni-doped La(Fe,Si)$_{13}$ series.

The results obtained by the analysis of the exponent n can be compared to those of applying the Banerjee's criterion. The Arrott plots of the studied samples for temperatures close to T_{trans} are plotted in Fig. 6.12 (low magnetic fields are not considered, as the samples are in multidomain state). The curves show negative slopes for x = 0.00 and 0.10 samples, indicating that they undergo a FOPT, while only positive slopes are observed for x = 0.18, 0.26 and 0.33 samples, indicating a SOPT behavior. These results are in good agreement with the MC field dependence analysis except for x = 0.18 sample. It should be noticed that this sample exhibits a composition very near to the critical SOPT-FOPT composition for this series. The imposition of a mean field model in this method leads to values of the critical exponents rather different from those of the critical SOPT-FOPT point, which attributes to its failure for this composition. Some discrepancies of the Banerjee's criterion were also reported for other MC materials [94].

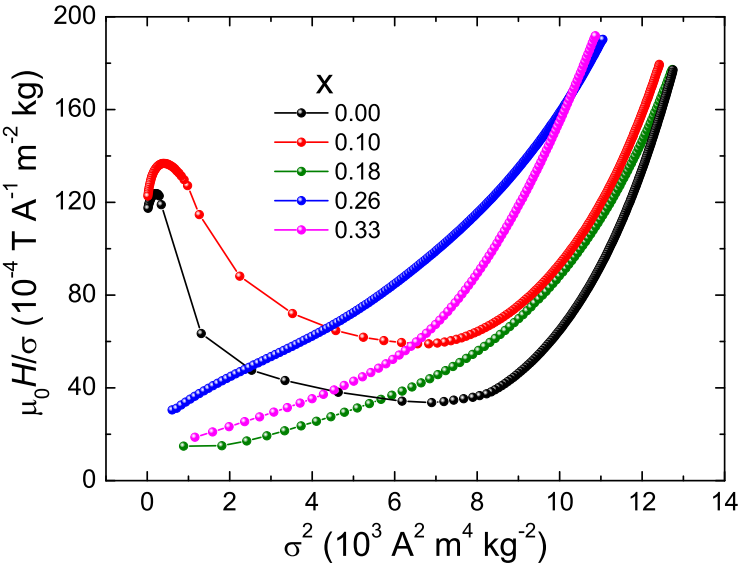

Figure 6.12: Arrott plots for selected temperatures close to their transitions for the Ni-doped La(Fe,Si)$_{13}$ series.

6.2 Cr-doped series

An alternative approach for MC optimization of La(Fe,Si)$_{13}$ is to optimize its FOPT character, which, in other words, will be to drive towards the FOPT category, unlike the former section. For that purpose, Cr-doped La(Fe,Si)$_{13}$ compounds are studied [176]. In addition, the critical composition of this series of compounds was also determined to attain reduced hysteresis.

6.2.1 Synthesis

La(Fe,Si)$_{13}$ compound with nominal composition LaFe$_{11.6}$Si$_{1.4}$ compound was chosen as parent composition. Nominal compositions LaFe$_{11.6-y}$Cr$_y$Si$_{1.4}$ (with y from 0 up to 0.6) were produced by induction melting from pure elements. A similar procedure as for Ni-doped

series was followed (see Subsection 6.1.1) though to enhance the Cr incorporation, the obtained ingot from induction melting was re-melted by arc melting instead of annealed at 1050 °C for 3 h. To introduce the arc melting step in the protocol, the initial mass amount was reduced from 20 to 5 g.

6.2.2 Microstructure

According to the previous observations for suction casted $La(Fe,Si)_{13}$ compounds, an annealing duration of 2 days has been chosen for Cr-doped series (double of the previous Ni-series to ensure good homogeneity and Cr incorporation, as the dopant amount is higher). Fig. 6.13 shows the BSE images for the higher Cr-doped sample after annealing at different temperatures in order to find the purest sample possible.

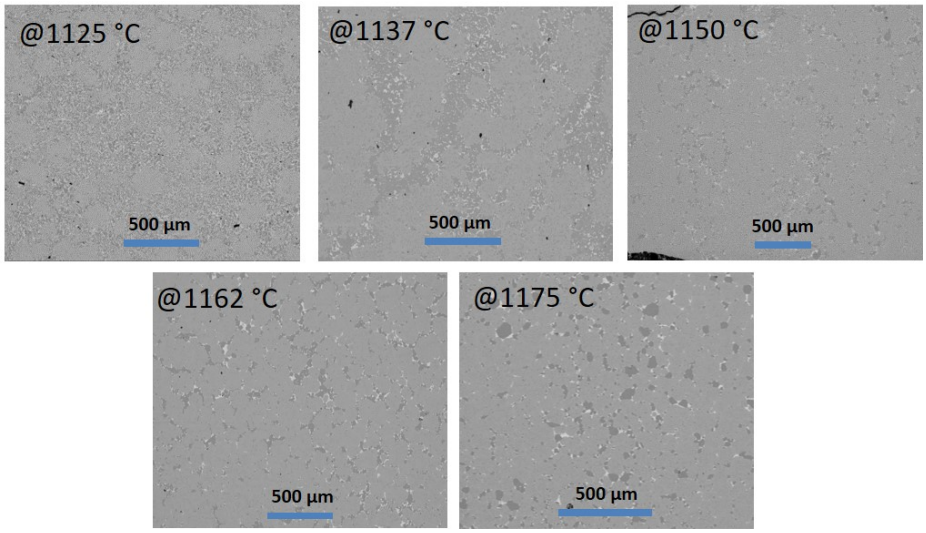

Figure 6.13: BSE images of the higher Cr-doped composition (nominal y = 0.6) treated at different temperatures during 2 days.

As for Ni-series, bright spots indicate the $La_1Fe_1Si_1$ phase (P4/nmm) though a new La-rich phase also appears (La_3Si_2 (tP10)), dark ones

correspond the α-Fe phase (Im-3m) and the grey ones to the desired 1:13 phase ($NaZn_{13}$-type, Fm-3c). The La_3Si_2 phase is more noticeable as Cr content increases. It can be observed that α-Fe and La-rich phases are abundant for the lowest annealing temperature (1125 °C), while the amount is reduced as temperature increases. For higher temperatures (above 1150 °C) the α-Fe areas start to increase, reducing the 1:13 purity. As for Ni-doped series, a dendritic structure is obtained for the secondary phases at low temperatures, while it evolves into granular particles (α-Fe surrounded by La-rich phase) at high temperatures. With this, the optimal annealing temperature for this sample is found for 1150 °C.

Fig. 6.14 shows the BSE images for Cr-doped $La(Fe,Si)_{13}$ series annealed during 2 days at the optimal temperatures for each composition.

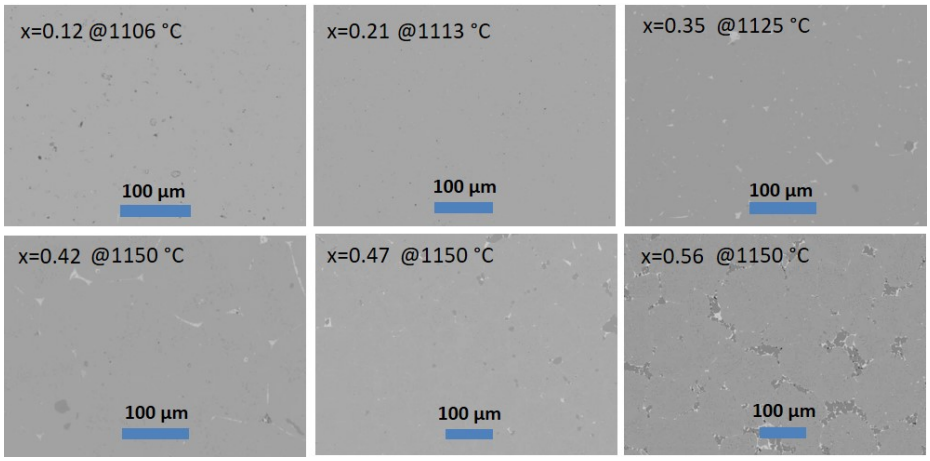

Figure 6.14: BSE images of the Cr-doped $La(Fe,Si)_{13}$ series annealed at different temperatures during 2 days.

It should be noted, in contrast to the Ni case, that the optimal temperature is significantly affected by Cr content. As a general feature, BSE images show a homogenous structure with the main phase of the desired 1:13 phase. Almost negligible α-Fe impurities were observed for samples with low Cr contents. Some bright spots of $La_1Fe_1Si_1$ phase can be noticed, which could be due to the excess La added in the initial powder mixture.

α-Fe phase becomes more noticeable with increasing Cr concentration. The different samples are now denoted by their Cr content in the 1:13 phase determined by EDX (y = 0.00, 0.12, 0.21, 0.35, 0.42, 0.47 and 0.56).

The large amount of the obtained 1:13 phase with compositions close to the nominal one (up to values close to 0.5) shows an extension of the solid solubility limit previously ascribed to Cr (y = 0.25) [171]. To determine the phase incorporation preference of Cr atoms, Table 6.3 shows the Cr/Fe ratio in the different presented phases for the higher Cr content samples (y = 0.47 and 0.56), where the presence of secondary phases is more significant. It is observed that the Cr/Fe ratio is the highest in α-Fe than in La-rich and 1:13 phases, indicating a preferential segregation of Cr into α-Fe. Cr traces are not detected in La_3Si_2. In addition, Table 6.4 shows the EDX analysis for the 1:13 phase presented in the Cr-doped La(Fe,Si)$_{13}$ series. A good agreement between the measured and nominal compositions is observed.

Sample	Cr/Fe nominal	Cr/Fe (1:13)	Cr/Fe (α-Fe)
y = 0.47	0.045	0.044	0.068
y = 0.56	0.054	0.051	0.071

Table 6.3: Cr/Fe ratio for the different phases presented in higher Cr-doped compositions.

Fig. 6.15 shows the XRD spectra for Cr-doped La(Fe,Si)$_{13}$ series. It can be observed that the samples mainly consist of 1:13 phase (the structure remains unaltered with Cr incorporation in the explored range) and trace amounts of α-Fe, in agreement with the BSE results. In contrast to BSE images, where some minor fractions of La-rich phases there were detected, in the case of XRD experiments were not detected. Minor peaks corresponding to α-Fe phase (2θ = 20.13º) become more evident with higher Cr content, especially for y = 0.47 and 0.56. The results from the Rietveld refinement of the different XRD spectra are tabulated in Table 6.4, in which all the GoF values close to 1 (ideal case) are observed.

The lattice parameter slightly decreases at a rate of 6(4) Å(at.% Cr)$^{-1}$.

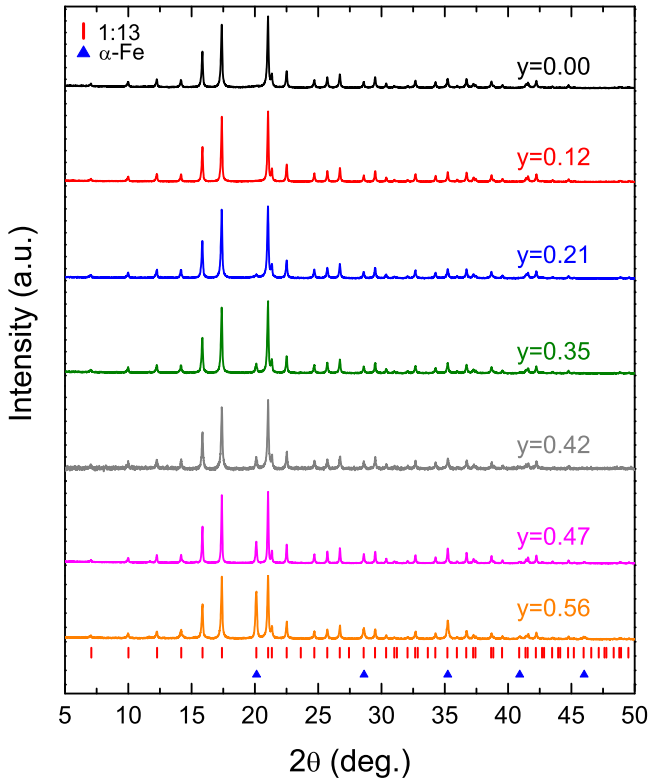

Figure 6.15: XRD spectra for the Cr-doped La(Fe,Si)$_{13}$ series.

Sample	1:13 phase composition	$x_{1:13}$ (wt.%)	$x_{\alpha-Fe}$ (wt.%)	$l_{1:13}$ (Å)	GoF
y=0.00	$La_{1.00(4)}Fe_{11.5(6)}Si_{1.40(14)}$	100	0	11.478(3)	1.55
y=0.12	$La_{1.00(4)}Fe_{11.3(7)}Cr_{0.12(2)}Si_{1.42(14)}$	100	0	11.476(3)	1.49
y=0.21	$La_{1.00(3)}Fe_{11.1(5)}Cr_{0.21(2)}Si_{1.42(14)}$	97.7	2.3	11.478(4)	1.39
y=0.35	$La_{1.00(6)}Fe_{11.0(7)}Cr_{0.35(5)}Si_{1.42(17)}$	94.9	5.1	11.477(4)	1.25
y=0.42	$La_{1.00(3)}Fe_{10.8(7)}Cr_{0.42(4)}Si_{1.53(16)}$	92.8	7.2	11.475(2)	1.10
y=0.47	$La_{1.00(3)}Fe_{10.8(5)}Cr_{0.47(3)}Si_{1.59(16)}$	87.5	12.5	11.477(2)	1.99
y=0.56	$La_{1.00(3)}Fe_{10.7(5)}Ni_{0.56(4)}Si_{1.59(16)}$	75.5	24.5	11.476(2)	1.34

Table 6.4: 1:13 phase composition determined by EDX, phase fractions, $l_{1:13}$ and GoF from Rietveld refinement of the XRD spectra of the Cr-doped La(Fe,Si)$_{13}$ series.

6.2.3 Magnetic and MC properties

Fig. 6.16 shows the temperature dependence of the normalized magnetization (with respect to the magnetization at 100 K) at 0.05 T (A) and T_{trans} (B) and ΔT_{hyst} (C) as function of the Cr content.

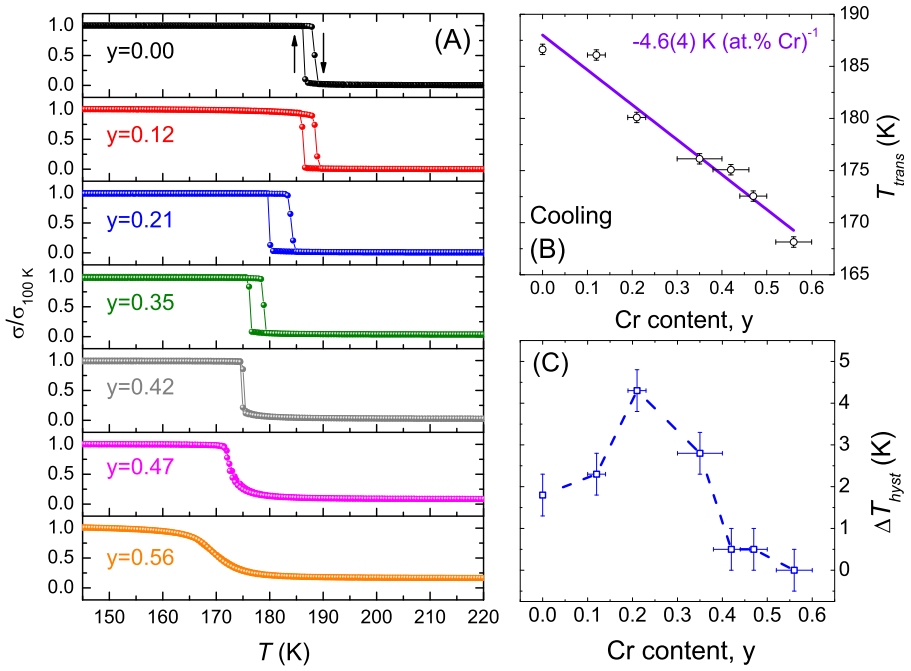

Figure 6.16: Temperature dependence of the normalized magnetization (with respect to the value at 100 K) at 0.05 T for the Cr-doped La(Fe,Si)$_{13}$ series (A). Transition temperature of 1:13 phase as a function of Cr content (B). Thermal hysteresis as a function of Cr content (C).

A clear shift of T_{trans} to lower values is observed; by using a linear fit to the data, a reduction of 4.6(4) K (at.% Cr)$^{-1}$ is estimated. It is observed that ΔT_{hyst} follows a non monotonous dependence as a function of Cr content. A maximum for the hysteresis values of 4.3(5) K is found for y = 0.21 (further discussed later). Removing the α-Fe effect in magnetization curves (from the fitting of the paramagnetic tail of

the data) it can be observed that the spontaneous magnetization at 150 K for the 1:13 phase decreases as Cr content increases at a rate of ≈ -10 A m^2 kg^{-1} (at.% Cr)$^{-1}$, although the presence of α-Fe prevents any further analysis.

The field hysteresis (ΔH_{hyst}) is analyzed from magnetization and demagnetization curves. Fig. 6.17 (A) shows the magnetic field dependence of σ (normalized with respect to the value for 2 T), for temperatures close to the transition, for the samples from y = 0.00 to 0.42. From these curves, ΔH_{hyst} values are obtained as a function of Cr content, as depicted in Fig. 6.17 (B). The data show a non-monotonic evolution of the field hysteresis (as also observed for the thermal hysteresis).

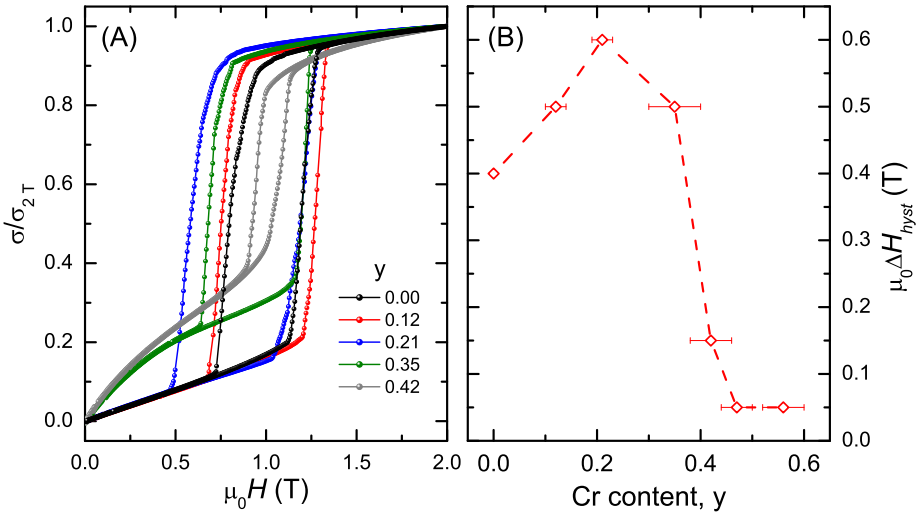

Figure 6.17: Magnetic field dependence of the normalized magnetization (with respect to the magnetization at 2 T), at temperatures close to the transition, for the set of samples from y = 0.00 up to 0.42 of the Cr-doped La(Fe,Si)$_{13}$ series (A). ΔH_{hyst} as a function of the Cr content (B).

Fig. 6.18 shows the temperature dependence of Δs_T and the Cr content dependence of $|\Delta s_T^{pk}|$ for 1.9 T for Cr-doped series measured while cooling. It is observed that Δs_T curves are shifted to lower temperatures with Cr addition, while the width of the curves becomes larger (from

$\Delta T_{FWHM} = 8.1$ to 14.4 K for y = 0.00 and 0.56, respectively). With respect the shape of the curves, a clear evolution can be observed: retaining similar shape to the parent composition up to y = 0.42 sample, being y = 0.47 an intermediate case between y = 0.56 and y = 0.42. In addition, it can be observed that $|\Delta s_T^{pk}|$ decreases with Cr content, following a power law of the form $|\Delta s_T^{pk}| = \kappa^{(0)} + \kappa^{(1)} \mathrm{x}^{\kappa^{(2)}}$ with $\kappa^{(0)} = 22.1(5)$ J kg^{-1} K^{-1}, $\kappa^{(1)} = -69(10)$ J kg^{-1} K^{-1} and $\kappa^{(2)} = 2.6(3)$.

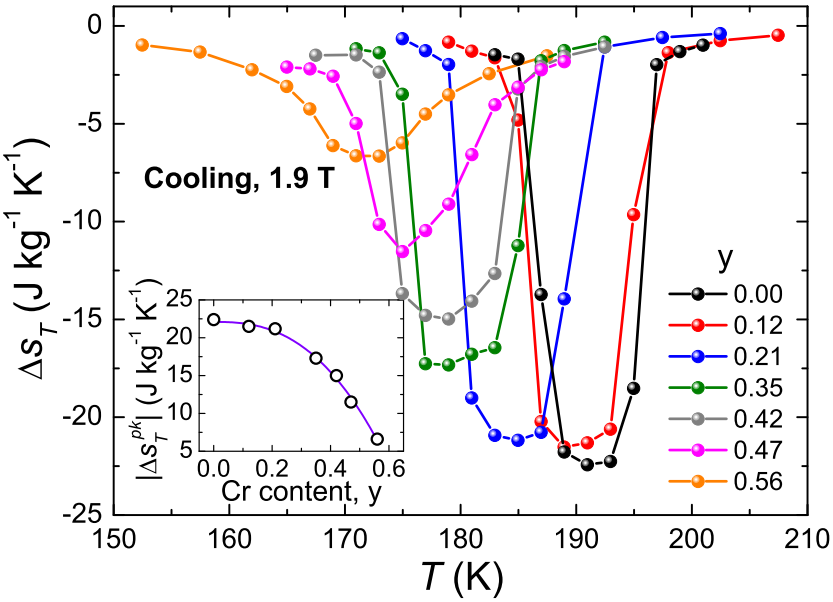

Figure 6.18: Temperature dependence of Δs_T for 1.9 T for the Cr-doped La(Fe,Si)$_{13}$ series measured while cooling.

Fig. 6.19 shows the temperature dependence of ΔT_S and the Cr content dependence of ΔT_S^{pk} for 1.9 T measured while cooling. The same features as for Δs_T are observed though, in this case, y = 0.47 retains a more similar shape to the parent compound. ΔT_S^{pk} decreases as Cr content increases, following a power law $\Delta T_S^{pk} = \kappa^{(0)} + \kappa^{(1)} \mathrm{x}^{\kappa^{(2)}}$ with $\kappa^{(0)} = 6.7(4)$ K, $\kappa^{(1)} = 10(3)$ K and $\kappa^{(2)} = 2.8(7)$. In addition, CRP_{min} is calculated using previous Δs_T, ΔT_S and $\sigma(T_C)$ data. Fig. 6.20 shows the CRP_{min} values as a function of Cr content.

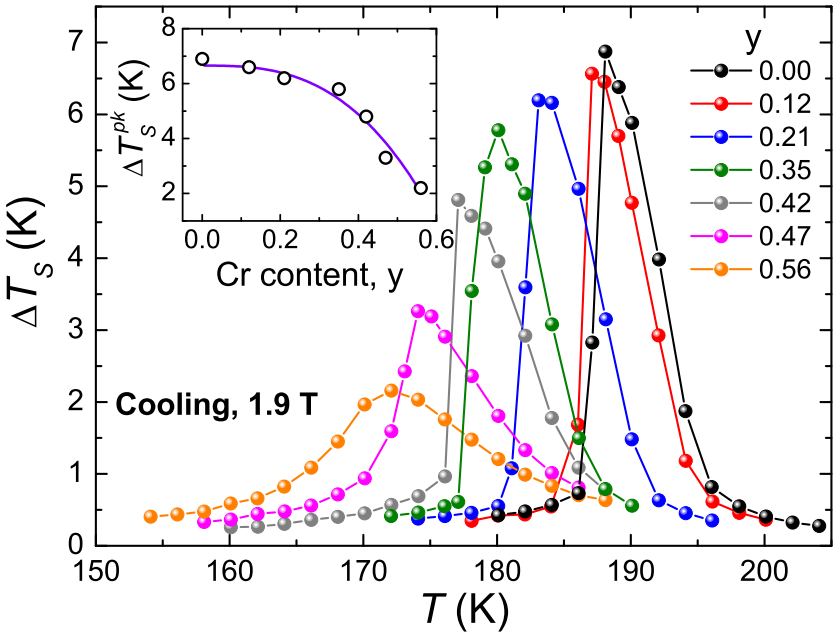

Figure 6.19: Temperature dependence of ΔT_S for Cr-doped La(Fe,Si)$_{13}$ series measured while cooling and 1.9 T.

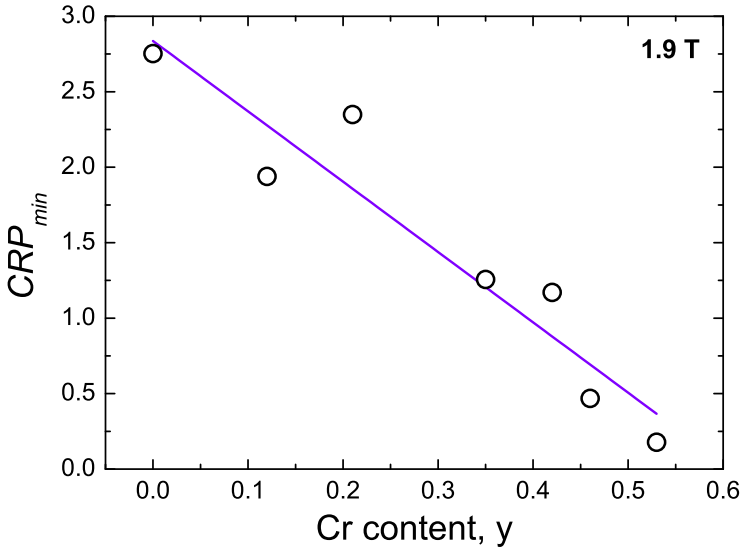

Figure 6.20: Cr content dependence of CRP_{min} for the Cr-doped La(Fe,Si)$_{13}$ series and 1.9 T.

A decrease of CRP_{min} with Cr addition is observed, though it is interesting to observe that Cr produces a larger decrease of the magnetization than Ni, the values of the MC magnitudes (Δs_T, ΔT_S and CRP_{min}) are less affected. This indicates the importance of the order of the phase transition.

To analyze the order of the phase transition of the series, the MC field dependence analyses have been applied. On one hand, Fig. 6.21 shows the temperature dependence of the exponent n for 1.9 T for Cr-doped series. An overshoot in the curves is observed near the phase transition from y = 0.00 up to y = 0.47 samples, indicating that they undergo FOPT. For the higher Cr-containing sample (y = 0.56), a gradual increase of n is observed from the minimum towards a maximum value of 2, indicating SOPT behavior.

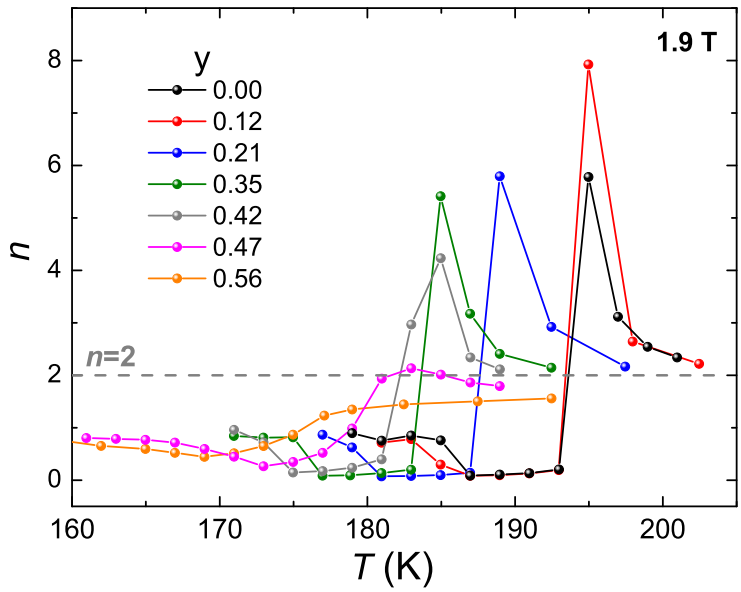

Figure 6.21: Temperature dependence of the exponent n for 1.9 T as a function of Cr content for the Cr-doped La(Fe,Si)$_{13}$ series.

On the other hand, Fig. 6.22 shows the exponent n values at the transition temperature for 1.9 T as a function of Cr content. It is observed that samples up to y = 0.47 show $n(T_{trans}) < 0.4$, indicating that they

undergo a FOPT. On the other hand, a larger $n(T_{trans})$ value (above 0.4) is observed for y = 0.56 sample, indicating that it undergoes a SOPT. These results are in agreement with the previous MC analysis. Moreover, the critical SOPT-FOPT composition is predicted for a Cr content of y = 0.53 (where it is assumed a linear interpolation between the different points). As in the case of the Ni-doped samples, the influence of the demagnetizing factor and impurities are neglected, as it is demonstrated that they have a small influence. For samples with a Si content of 1.5 ($LaFe_{11.5-y}Cr_ySi_{1.5}$), it was reported a critical Cr content of y = 0.26 [171], which is a smaller limit compared to our case.

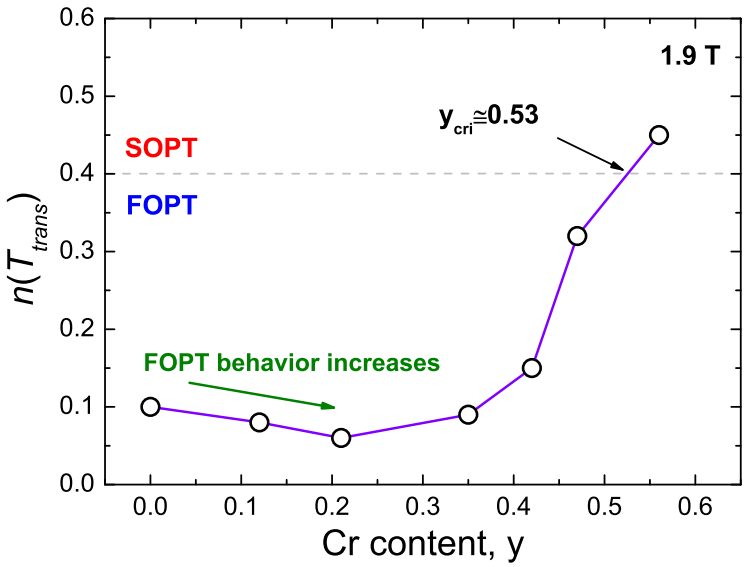

Figure 6.22: $n(T_{trans})$ as a function of Cr content for the Cr-doped $La(Fe,Si)_{13}$ series.

Moreover, from the values of $n(T_{trans})$ an increase of the FOPT character can be detected for samples y = 0.12, 0.21 and 0.35 compared to the parent sample (according to the analysis shown in Fig. 4.18) and the $n(T_{trans})$ values decrease as η increases. This is in agreement with the performed analysis of the hysteresis.

The results obtained from the field dependence MC analyses can be compared to those of applying the Banerjee's criterion. The Arrott plots of the Cr-series samples are plotted in Fig. 6.23 (low magnetic fields are not considered, as samples are in multidomain state). They show good agreement with the former analyses, except for y = 0.47, which shows positive slopes in the Arrott plot (except for the first point at very small field, which is also observed for y = 0.56). Analogously to the Ni case, the sample for which different results are obtained has a composition very near to the critical SOPT-FOPT point for this series. The imposition of a mean field model can explain the failure of Banerjee's criterion for this y = 0.47 composition.

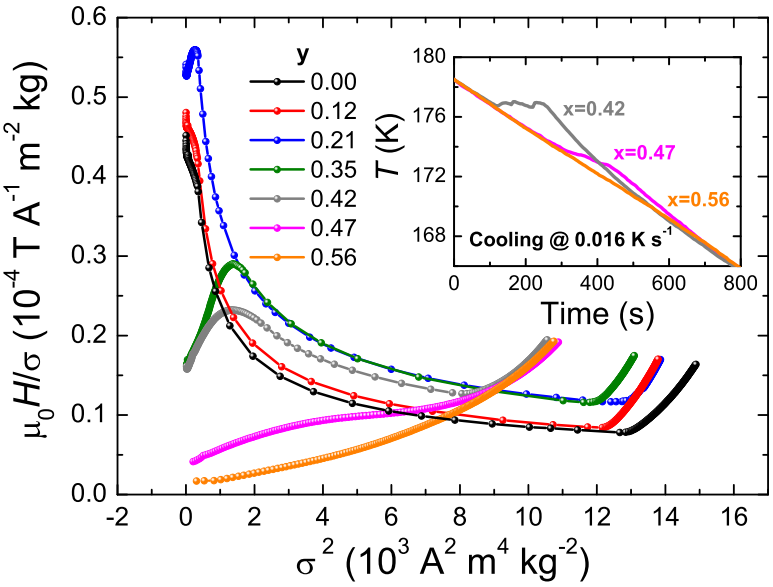

Figure 6.23: Arrott plots for the Cr-doped La(Fe,Si)$_{13}$ series at selected temperatures close to the transition temperature for each composition. Inset: Temperature scan while cooling for the higher Cr-doped samples.

Another way to extract information about the order of the transition is to observe the time dependence of the temperature of the material close to the transition. For FOPT, a plateau region is attained (the sample temperature remains constant during the transition) while, for SOPT, a

gradual evolution of the sample temperature can be found. The inset of Fig. 6.23 shows the temperature evolution for the samples closer to the critical FOPT-SOPT composition while they are submitted to a constant cooling rate of 0.0016 K s^{-1}. A plateau is observed for both y = 0.42 and 0.47 samples (though it is smoother for the latter, as it is closer to the critical point), indicating FOPT. On the other hand, for y = 0.56 sample, a continuous evolution is observed (a slight slope change can be observed at the transition temperature), indicating SOPT. These results are in agreement with those obtained from the MC field dependence analysis, confirming the accuracy of the method (but differ from those of the Banerjee's criterion).

6.3 Conclusions

In this chapter, previously described analysis methods were used to characterize the influence of Ni and Cr doping on the thermomagnetic phase transition characteristics and magnetocaloric properties of $La(Fe,Si)_{13}$ compounds, surpassing the accuracy of conventionally used Banerjee's criterion. Optimization of FOPT $La(Fe,Si)_{13}$-based MC materials is achieved:

- For both series, suction casting process is shown as a powerfull synthesis route which allows a drastic reduction of the annealing time, accompanied by an extension of the solubility limit of the dopants. Microstructural characterization reveals a large phase fraction of the desired $NaZn_{13}$-type structure after thermal annealings, though Ni and Cr incorporation led to the appearance of impurity phases beyond the solid-solubility limits of the dopants (found around 0.3 and 0.5 for Ni and Cr doping, repectively).
- A reduction of the hysteresis without a signicative change of magnetization or transition temperature is achieved for small amounts of Ni doping. This feature is found to be ascribed to

the FOPT-behavior transformation into SOPT with increasing Ni concentration. Using the field dependence analyses of Δs_T, the order of the phase transition was determined for each composition, finding a critical SOPT-FOPT composition for x = 0.19. This corresponds to a 2.4-fold extension compared to the values previously reported for similar alloys.

- Δs_T and ΔT_S values are rettained for low Cr concentration (y $<$ 0.3), despite a significant reduction of the magnetization with increasing Cr concentration (in contrast with the previous Ni case). Using the field dependence analyses, a non-monotonic evolution of the order of phase transition is corroborated : for Cr content samples below y $\approx$ 0.3, the FOPT character increases, while above it continuously decreases to a SOPT character. The critical SOPT-FOPT composition was determined for y = 0.53, corresponding to a 2.1-fold extension compared to the values previously reported for similar alloys.

7 General conclusions

The objective of this thesis was to perform a thorough study of the relation between thermomagnetic phase transitions and the MC response of materials. This involves a combination of materials development, physical simulation of the underlying processes and analysis of the experimental techniques involved in the characterization of materials.

The conclusions of the three main parts that constitute the thesis are:

1. Analysis of experimental techniques

- The demagnetizing field does not significantly affect Δs_T, however, it must be taken into account for a correct interpretation of the field dependence exponent n, as the results can be strongly affected for temperatures up to T_C. Failing to do so can lead to erroneous determination of critical exponents or to misleading interpretations in the analysis of the phase transitions.

- It has been noticed that some samples exhibit anomalously large value of the exponent that controls the field dependence of the magnetic entropy change. This effect can be explained by a distribution of Cutie temperatures, modeled as a Gaussian distribution, caused by compositional inhomogeneities.

- It is experimentally impossible to reach 0 K during the measurement of the field and temperature dependent specific heat. The truncation

of the experimental data in the low temperature range causes relevant deviations of the calculated MC response when compared to an ideally measured sample that could reach extremely low temperatures. It was found that, independently of the order of the phase transition, there exists an initial temperature for which the approximated MC curves are the same as those when the integration is performed down to zero kelvin (being the same for both Δs_T and ΔT_S). It was shown that Δs_T curves starting from a finite initial temperature different from 0 K, are deviated in a temperature independent way, while for ΔT_S curves the differences are temperature dependent, which in first approximation follows a T/c_H dependence. The analysis and corresponding method to determine this optimal initial temperature there was performed for both single phase and multiphasic materials.

- The sample's previous history causes underestimations of directly measured ΔT_S values in the FOPT transition region, with a shift of its peak transition unless the proper measurement protocol is used. These discrepancies are shown to be highly dependent on the hysteretic temperature span with respect to the selection of temperature increment during measurements.

2. Characterization of phase transitions using MC effect

- A procedure was proposed for determining the Curie temperature from MC data. It was checked using numerical calculations and experimental measurements on a Fe-based amorphous alloy. The main advantages of the proposed method are: it is neither an iterative nor a fitting procedure, no assumptions on the critical exponents describing the transition are required and results are field independent.

- MC field dependence analyses were shown as a precise technique to determine the critical exponents of the transition providing

an excellent agreement with those determined using K-F method. Moreover, it was shown that the MC method allows to obtain the critical exponents of biphasic materials, a case for which K-F method is not applicable.

- MC field dependence analyses were extended to FOPT and SOPT materials, providing an useful criterion to determine the order of the phase transition and the critical SOPT-FOPT composition. The analysis has been validated using the B-R model, finding an excellent agreement with experimental results. Two criteria are shown:
  - For FOPT MC materials, exponent n shows an overshoot above 2 at temperatures close to the transition temperature. For SOPT MC materials, the overshoot is not observed and the exponent n monotonously increases from $n(T_C)$ up to 2.
  - The exponent n at the transition temperature was found to be below 0.4 for FOPT while, for SOPT, it is above 0.4. For the critical SOPT-FOPT point its value is exactly 0.4.

3. Development of SOPT and FOPT MC materials

- A series of Gd-GdZn composites have been successfully synthesized in a single step. They exhibited a similar table-like Δs_T behavior for compositions around 25 – 50 at.% Zn content. This characteristic leads to the enhanced RCP values for the composites as compared to the pure materials, 11 % and 45 % with respect to Gd and GdZn materials, respectively. It was shown that Δs_T of Gd-GdZn composites can be modeled by considering non-interacting phases. The developed methods to calculate the MC effect from truncated calorimetric data was succesfully applied for the Gd-GdZn series.
- The MC response of a multilayer Gd/Ti system was analyzed and compared to that of a Gd bulk sample. It was shown that the field dependence Gd/Ti multilayers is enhanced through nanostructuring

(though at expenses of a decrease of the response) as higher values of the field dependence exponent n in the vicinity of the transition temperature are obtained. It was shown that this fact can be ascribed to a Curie temperature distribution due to small variations in the layer thickness related to finite size scaling, as confirmed by numerical simulations.

- Two Ni- and Cr-doped $La(Fe,Si)_{13}$ ($LaFe_{11.6-x}Ni_xSi_{1.4}$ and $LaFe_{11.6-y}Cr_ySi_{1.4}$ compositions, respectively) series were synthesized by suction casting, which is shown as a powerfull synthesis route allowing a drastic reduction of the annealing time accompanied by an extension of the solubility range of the dopant. With respect to the MC properties and nature of phase transitions:

  - For the Ni-doped series, thermal hysteresis was reduced by small dopant additions, with very slight modification of the transition temperature and magnetization, though with a significant reduction of the MC response. Using the proposed analyses, these features were found to be ascribed to a FOPT transformation into SOPT with increasing doping concentration, determining the critical SOPT-FOPT composition for a Ni content $x = 0.19$.
  - In the case of Cr-doped series, although the magnetization and transition temperatures are significantly modified, the MC response was kept constant up to considerable Cr contents ($y \approx 0.3$). Applying the proposed analysis, this counter-intuitive behavior is ascribed to an increase of the FOPT-character for low Cr concentrations. The critical SOPT-FOPT composition was determined to correspond to a Cr content of $y = 0.53$. This behavior is supported by the thermal and magnetic hysteresis evolution with increasing Cr concentration.
  - For both series, it was shown that the proposed MC analyses surpass the accuracy of conventionally used Banerjee's criterion for determining the order of magnetic phase transitions.

Publication list

The following list includes the publications directly related to the work contained in this thesis:

1. **L M Moreno-Ramírez**, J J Ipus, V Franco, J S Blázquez, A Conde. Analysis of magnetocaloric effect of ball milled amorphous alloys: Demagnetizing factor and Curie temperature distribution. *J. Alloys Compd.*, 622:606-609, 2015.

2. **L M Moreno-Ramírez**, J S Blázquez, V Franco, A Conde, M Marsilius, V Budinsky, G Herzer. A new method for determining the Curie Temperature from magnetocaloric measurements. *IEEE Magn. Lett.*, 7:6102004, 2016.

3. **L M Moreno-Ramírez**, J S Blázquez, J Y Law, V Franco, A Conde. A Optimal temperature range for determining magnetocaloric magnitudes from heat capacity. *J. Phys. D. Appl. Phys.*, 49:495001, 2016.

4. M Sánchez-Pérez, **L M Moreno-Ramírez**, V Franco, A Conde, M Marsilius, G Herzer. Influence of nanocrystallization on the magnetocaloric properties of Ni-based amorphous alloys: Determination of critical exponents in multiphase systems. *J. Alloys Compd.*, 686:717-722, 2016.

5. J Y Law, **L M Moreno-Ramírez**, J S Blázquez, V Franco, A Conde. Gd+GdZn biphasic magnetic composites synthesized in a single preparation step: Increasing refrigerant capacity without decreasing magnetic entropy change. *J. Alloys Compd.*, 675:244-247, 2016.

6. D Doblas, **L M Moreno-Ramírez**, V Franco, A Conde, A V Svalov, G V Kurlyandskaya. Nanostructuring as a procedure to control the field dependence of the magnetocaloric effect. *Mater. Des.*, 114:214-219, 2017.

7. **L M Moreno-Ramírez**, V Franco, M Pekala, A Conde. Influence of noise on the determination of Curie temperature from magnetocaloric analysis. *IEEE Trans. Magn.*, 53:2502004, 2017.

8. **L M Moreno-Ramírez**, C Romero-Muñiz, J Y Law, V Franco, A Conde, I A Radulov, F Maccari, K P Skokov, O Gutfleisch. The role of Ni in modifying the order of the phase transition of $La(Fe,Ni,Si)_{13}$. *Acta Mater.*, 160:137-146, 2018.

9. **L M Moreno-Ramírez**, V Franco, A Conde, H Neves Bez, Y Mudryk, V K Pecharsky. Influence of the starting temperature of calorimetric measurements on the accuracy of determined magnetocaloric effect. *J. Magn. Magn. Mater.*, 457:64-69, 2018.

10. J Y Law, V Franco, **L M Moreno-Ramírez**, A Conde, D Y Karpenkov, I A Radulov, K P Skokov, O Gutfleisch. A quantitative criterion for determining the order of magnetic phase transitions using the magnetocaloric effect. *Nat. Commun.*, 9:2680, 2018.

11. **L M Moreno-Ramírez**, V Franco, A Conde. Influence of low temperature truncated calorimetric data on the determination of the magnetocaloric effect of biphasic materials. *J. Magn. Magn. Mater.*, 479:236-239, 2019.

12. **L M Moreno-Ramírez**, A Delgado-Matarín, J Y Law, V Franco, A Conde, A K Giri. The thermal and magnetic history dependence of direct ΔT_{ad} measurements of $Ni_{49+x}Mn_{36-x}In_{15}$ Heusler compounds. *Submitted.*

13. **L M Moreno-Ramírez**, C Romero-Muñiz, J Y Law, V Franco, A Conde, I A Radulov, F Maccari, K P Skokov, O Gutfleisch. Tunable first order transition in $La(Fe, Cr, Si)_{13}$ compounds: retaining magnetocaloric response despite a magnetic moment reduction. *Submitted.*

Bibliography

[1] V K Pecharsky and K A Gschneidner. Magnetocaloric effect and magnetic refrigeration. *J. Magn. Magn. Mater.*, 200(1):44–56, 1999.

[2] A M Tishin and Y I Spichkin. *The Magnetocaloric Effect and its Applications*. Elsevier, 2003.

[3] E Brück. Developments in magnetocaloric refrigeration. *J. Phys. D. Appl. Phys.*, 38(23):R381, 2005.

[4] K A Gschneidner, V K Pecharsky, and A O Tsokol. Recent developments in magnetocaloric materials. *Reports Prog. Phys.*, 68(6):1479–1539, 2005.

[5] O Gutfleisch, M A Willard, E Brück, C H Chen, S G Sankar, and J P Liu. Magnetic Materials and Devices for the 21st Century: Stronger, Lighter, and More Energy Efficient. *Adv. Mater.*, 23(7):821–842, 2011.

[6] J Lyubina. Magnetocaloric materials for energy efficient cooling. *J. Phys. D. Appl. Phys.*, 50(5):53002, 2017.

[7] V Franco, J S Blázquez, J J Ipus, J Y Law, L M Moreno-Ramírez, and A Conde. Magnetocaloric effect: From materials research to refrigeration devices. *Prog. Mater. Sci.*, 93:112–232, 2018.

[8] P Weiss and A Piccard. Le phénomène magnétocalorique. *J. Phys. Theor. Appl.*, 7(1):103–109, 1917.

[9] E Warburg. Magnetische Untersuchungen. *Ann. Phys.*, 249(5):141–164, 1881.

[10] A Smith. Who discovered the magnetocaloric effect? *Eur. Phys. J. H*, 38(4):507–517, 2013.

[11] P Weiss. Le phénomène magnéto-calorique. *J. Phys. Radium*, 2(6):161–182, 1921.

[12] C Kittel. *Introduction to Solid State Physics*. John Wiley & Sons, 6th edition, 1986.

[13] G V Brown. Magnetic heat pumping near room temperature. *J. Appl. Phys.*, 47(8):3673–3680, 1976.

[14] C Zimm, A Jastrab, A Sternberg, V Pecharsky, K Gschneidner, M Osborne, and I Anderson. Description and Performance of a Near-Room Temperature Magnetic Refrigerator. In *Adv. Cryog. Eng.*, pages 1759–1766. Springer US, 1998.

[15] E Brück. Chapter Four Magnetocaloric Refrigeration at Ambient Temperature. In K H J Buschow, editor, *Handbook of Magnetic Materials*, volume 17, pages 235–291. Elsevier, 2007.

[16] A Kitanovski, U Plaznik, U Tomc, and A Poredoš. Present and future caloric refrigeration and heat-pump technologies. *Int. J. Refrig.*, 57:288–298, 2015.

[17] A Kitanovski, J Tušek, U Tomc, U Plaznik, M Ožbolt, and A Poredoš. *Magnetocaloric Energy Conversion: From Theory to Applications*. Springer, 2015.

[18] J Romero Gómez, R Ferreiro Garcia, A De Miguel Catoira, and M Romero Gómez. Magnetocaloric effect: A review of the thermodynamic cycles in magnetic refrigeration. *Renew. Sustain. Energy Rev.*, 17:74–82, 2013.

[19] W A Steyert. Stirling cycle rotating magnetic refrigerators and heat engines for use near room temperature. *J. Appl. Phys.*, 49(3):1216–1226, 1978.

[20] V Franco, J S Blázquez, B Ingale, and A Conde. The Magnetocaloric Effect and Magnetic Refrigeration Near Room Temperature: Materials and Models. *Annu. Rev. Mater. Res.*, 42(1):305–342, 2012.

[21] U.S.E.I. Administration. Annual Energy Outlook, 2017.

[22] D C Wang, Y H Li, D Li, Y Z Xia, and J P Zhang. A review on adsorption refrigeration technology and adsorption deterioration in physical adsorption systems. *Renew. Sustain. Energy Rev.*, 14(1):344–353, 2010.

[23] Www.basf.com/en/company/news and-media/news-releases/2015/01/p 15-100.html. 2015.

[24] A M Tishin, Y I Spichkin, V I Zverev, and P W Egolf. A review and new perspectives for the magnetocaloric effect: New materials and local heating and cooling inside the human body. *Int. J. Refrig.*, 68:177–186, 2016.

[25] J Feng, R Geutjens, N V Thang, J Li, X Guo, A Kéri, S Basak, G Galbács, G Biskos, H Nirschl, H W Zandbergen, E Brück, and A Schmidt-Ott. Magnetic Phase Transition in Spark-Produced Ternary LaFeSi Nanoalloys. *ACS Appl. Mater. Interfaces*, 10(7):6073–6078, 2018.

[26] M Barbic, S J Dodd, H D Morris, N Dilley, B Marcheschi, A Huston, T D Harris, and A P Koretsky. Magnetocaloric materials as switchable high contrast ratio MRI labels. *Magn. Reson. Med.*, 81(4):2238–2246, 2019.

[27] S M Harstad, P Zhao, N Soin, A A El-Gendy, S Gupta, V K Pecharsky, J Luo, and R L Hadimani. Gd_5Si_4-PVDF nanocomposite films and their potential for triboelectric energy harvesting applications. *AIP Adv.*, 9(3):35116, 2019.

[28] S Ahmim, M Almanza, A Pasko, F Mazaleyrat, and M LoBue. Thermal energy harvesting system based on magnetocaloric materials. *Eur. Phys. J. Appl. Phys.*, 85(1):10902, 2019.

[29] V K Pecharsky and K A Gschneidner. Magnetocaloric effect from indirect measurements: Magnetization and heat capacity. *J. Appl. Phys.*, 86(1):565–575, 1999.

[30] M E Wood and W H Potter. General analysis of magnetic refrigeration and its optimization using a new concept: maximization of refrigerant capacity. *Cryogenics*, 25(12):667–683, 1985.

[31] F Guillou, H Yibole, G Porcari, L Zhang, N H van Dijk, and E Brück. Magnetocaloric effect, cyclability and coefficient of refrigerant performance in the MnFe(P, Si, B) system. *J. Appl. Phys.*, 116(6):63903, 2014.

[32] W F Giauque and D P MacDougall. Attainment of Temperatures Below 1 ° Absolute by Demagnetization of $Gd_2(SO_4)_3 \cdot 8H_2O$. *Phys. Rev.*, 43(9):7768, 1933.

[33] M Evangelisti and E K Brechin. Recipes for enhanced molecular cooling. *Dalt. Trans.*, 39(20):4672–4676, 2010.

[34] S K Langley, N F Chilton, B Moubaraki, T Hooper, E K Brechin, M Evangelisti, and K S Murray. Molecular coolers: The case for $[Cu_5^{II}Gd_4^{III}]$. *Chem. Sci.*, 2(6):1166–1169, 2011.

[35] G Jaeger. The Ehrenfest Classification of Phase Transitions: Introduction and Evolution. *Arch. Hist. Exact Sci.*, 53(1):51–81, 1998.

[36] A Smaili and R Chahine. Composite materials for Ericsson-like magnetic refrigeration cycle. *J. Appl. Phys.*, 81(2):824–829, 1997.

[37] R Caballero-Flores, V Franco, A Conde, K E Knipling, and M A Willard. Optimization of the refrigerant capacity in multiphase magnetocaloric materials. *Appl. Phys. Lett.*, 98(10):102505, 2011.

[38] O Roubeau, E Natividad, M Evangelisti, G Lorusso, and E Palacios. A magnetocaloric composite based on molecular coolers and carbon nanotubes with enhanced thermal conductivity. *Mater. Horiz.*, 4(3):464–476, 2017.

[39] P Poddar, S Srinath, J Gass, B L V Prasad, and H Srikanth. Magnetic Transition and Large Magnetocaloric Effect Associated with Surface Spin Disorder in Co and $Co_{core}Ag_{shell}$ Nanoparticles. *J. Phys. Chem. C*, 111(38):14060–14066, 2007.

[40] R Skomski, Ch. Binek, S Michalski, T Mukherjee, A Enders, and D J Sellmyer. Entropy localization in magnetic compounds and thin-film nanostructures. *J. Appl. Phys.*, 107(9):09A922, 2010.

[41] R Caballero-Flores, V Franco, A Conde, L F Kiss, L Peter, and I Bakonyi. Magnetic Multilayers as a Way to Increase the Magnetic Field Responsiveness of Magnetocaloric Materials. *J. Nanosci. Nanotechnol.*, 12(9):7432–7436, 2012.

[42] V K Pecharsky and K A Gschneidner Jr. Giant Magnetocaloric Effect in $Gd_5(Si_2Ge_2)$. *Phys. Rev. Lett.*, 78(23):4494–4497, 1997.

[43] M P Annaorazov, S A Nikitin, A L Tyurin, K A Asatryan, and A Kh. Dovletov. Anomalously high entropy change in FeRh alloy. *J. Appl. Phys.*, 79(3):1689–1695, 1996.

[44] A Fujita, S Fujieda, Y Hasegawa, and K Fukamichi. Itinerant-electron metamagnetic transition and large magnetocaloric effects in $La(Fe_x,Si_{1-x})_{13}$ compounds and their hydrides. *Phys. Rev. B*, 67(10):104416, 2003.

[45] B G Shen, J R Sun, F X Hu, H W Zhang, and Z H Cheng. Recent Progress in Exploring Magnetocaloric Materials. *Adv. Mater.*, 21(45):4545–4564, 2009.

[46] J Lyubina, O Gutfleisch, M D Kuz'min, and M Richter. $La(Fe,Si)_{13}$-based magnetic refrigerants obtained by novel processing routes. *J. Magn. Magn. Mater.*, 320(18):2252–2258, 2008.

[47] J Liu, J D Moore, K P Skokov, M Krautz, K Löwe, A Barcza, M Katter, and O Gutfleisch. Exploring $La(Fe,Si)_{13}$-based magnetic refrigerants towards application. *Scr. Mater.*, 67(6):584–589, 2012.

[48] L Pareti, M Solzi, F Albertini, and A Paoluzi. Giant entropy change at the co-occurrence of structural and magnetic transitions in the NiMnGa Heusler alloy. *Eur. Phys. J. B*, 32:303–307, 2003.

[49] T Krenke, E Duman, M Acet, E F Wassermann, X Moya, L Mañosa, and A Planes. Inverse magnetocaloric effect in ferromagnetic Ni–Mn–Sn alloys. *Nat. Mater.*, 4:450, 2005.

[50] A Planes, Ll. Mañosa, X Moya, T Krenke, M Acet, and E F Wassermann. Magnetocaloric effect in Heusler shape-memory alloys. *J. Magn. Magn. Mater.*, 310(2, Part 3):2767–2769, 2007.

[51] T Gottschall, K P Skokov, B Frincu, and O Gutfleisch. Large reversible magnetocaloric effect in Ni-Mn-In-Co. *Appl. Phys. Lett.*, 106(2):21901, 2015.

[52] Z Gercsi, K Hono, and K G Sandeman. Designed metamagnetism in $CoMnGe_{1-x}P_x$. *Phys. Rev. B*, 83(17):174403, 2011.

[53] T Samanta, I Dubenko, A Quetz, S Stadler, and N Ali. Giant magnetocaloric effects near room temperature in $Mn_{1-x}Cu_xCoGe$. *Appl. Phys. Lett.*, 101(24):242405, 2012.

[54] C L Zhang, H F Shi, E J Ye, Y G Nie, Z D Han, B Qian, and D H Wang. Magnetostructural transition and magnetocaloric effect in MnNiSi-Fe_2Ge system. *Appl. Phys. Lett.*, 107(21):212403, 2015.

[55] T Samanta, D L Lepkowski, A U Saleheen, A Shankar, J Prestigiacomo, I Dubenko, A Quetz, I W H Oswald, G T McCandless, J Y Chan, P W Adams, D P Young, N Ali, and S Stadler. Hydrostatic pressure-induced modifications of structural transitions lead to large enhancements of magnetocaloric effects in MnNiSi-based systems. *Phys. Rev. B*, 91(2):20401, 2015.

[56] O Tegus, E Brück, K H J Buschow, and F R de Boer. Transition-metal-based magnetic refrigerants for room-temperature applications. *Nature*, 415:150, 2002.

[57] E Brück, O Tegus, D T Cam Thanh, Nguyen T Trung, and K H J Buschow. A review on Mn based materials for magnetic refrigeration: Structure and properties. *Int. J. Refrig.*, 31(5):763–770, 2008.

[58] M Fries, L Pfeuffer, E Bruder, T Gottschall, S Ener, L V B Diop, T Gröb, K P Skokov, and O Gutfleisch. Microstructural and magnetic properties of Mn-Fe-P-Si (Fe_2P-type) magnetocaloric compounds. *Acta Mater.*, 132:222–229, 2017.

[59] J Liu, T Gottschall, K P Skokov, J D Moore, and O Gutfleisch. Giant magnetocaloric effect driven by structural transitions. *Nat. Mater.*, 11:620, 2012.

[60] A Aliev, A Batdalov, S Bosko, V Buchelnikov, I Dikshtein, V Khovailo, V Koledov, R Levitin, V Shavrov, and T Takagi. Magnetocaloric effect and magnetization in a Ni-Mn-Ga Heusler

alloy in the vicinity of magnetostructural transition. *J. Magn. Magn. Mater.*, 272-276:2040–2042, 2004.

[61] E Brück, M Ilyn, A M Tishin, and O Tegus. Magnetocaloric effects in $MnFeP_{1-x}As_x$-based compounds. *J. Magn. Magn. Mater.*, 290-291:8–13, 2005.

[62] A Chirkova, K P Skokov, L Schultz, N V Baranov, O Gutfleisch, and T G Woodcock. Giant adiabatic temperature change in FeRh alloys evidenced by direct measurements under cyclic conditions. *Acta Mater.*, 106:15–21, 2016.

[63] X Tan, P Chai, C M Thompson, and M Shatruk. Magnetocaloric Effect in $AlFe_2B_2$: Toward Magnetic Refrigerants from Earth-Abundant Elements. *J. Am. Chem. Soc.*, 135(25):9553–9557, 2013.

[64] H Wada and Y Tanabe. Giant magnetocaloric effect of $MnAs_{1-x}Sb_x$. *Appl. Phys. Lett.*, 79(20):3302–3304, 2001.

[65] V Provenzano, A J Shapiro, and R D Shull. Reduction of hysteresis losses in the magnetic refrigerant $Gd_5Ge_2Si_2$ by the addition of iron. *Nature*, 429(6994):853–857, 2004.

[66] J Shen, B Gao, H W Zhang, F X Hu, Y X Li, J R Sun, and B G Shen. Reduction of hysteresis loss and large magnetic entropy change in the $NaZn_{13}$-type LaPrFeSiC interstitial compounds. *Appl. Phys. Lett.*, 91(14):142504, 2007.

[67] K Morrison, J D Moore, K G Sandeman, A D Caplin, and L F Cohen. Capturing first- and second-order behavior in magnetocaloric $CoMnSi_{0.92}Ge_{0.08}$. *Phys. Rev. B*, 79(13):134408, 2009.

[68] K G Sandeman. Magnetocaloric materials: The search for new systems. *Scr. Mater.*, 67(6):566–571, 2012.

[69] M Bratko, E Lovell, A D Caplin, V Basso, A Barcza, M Katter, and L F Cohen. Determining the first-order character of $La(Fe,Mn,Si)_{13}$. *Phys. Rev. B*, 95(6):64411, 2017.

[70] M F J Boeije, M Maschek, X F Miao, N V Thang, N H van Dijk, and E Brück. Mixed magnetism in magnetocaloric materials with first-order and second-order magnetoelastic transitions. *J. Phys. D. Appl. Phys.*, 50(17):174002, 2017.

[71] V Franco, J Y Law, A Conde, V Brabander, D Y Karpenkov, I Radulov, K Skokov, and O Gutfleisch. Predicting the tricritical point composition of a series of LaFeSi magnetocaloric alloys via universal scaling. *J. Phys. D. Appl. Phys.*, 50(41):414004, 2017.

[72] H Yamada. Metamagnetic transition and susceptibility maximum in an itinerant-electron system. *Phys. Rev. B*, 47(17):11211–11219, 1993.

[73] A Fujita, Y Akamatsu, and K Fukamichi. Itinerant electron metamagnetic transition in $La(Fe_xSi_{1-x})_{13}$ intermetallic compounds. *J. Appl. Phys.*, 85(8):4756–4758, 1999.

[74] A Smith, C R H Bahl, R Bjørk, K Engelbrecht, K K Nielsen, and N Pryds. Materials Challenges for High Performance Magnetocaloric Refrigeration Devices. *Adv. Energy Mater.*, 2(11):1288–1318, 2012.

[75] B Kaeswurm, V Franco, K P Skokov, and O Gutfleisch. Assessment of the magnetocaloric effect in La,Pr(Fe,Si) under cycling. *J. Magn. Magn. Mater.*, 406:259–265, 2016.

[76] Y Wang, H Zhang, E Liu, X Zhong, K Tao, M Wu, C Xing, Y Xiao, J Liu, and Y Long. Outstanding Comprehensive Performance of $La(Fe, Si)_{13}H_y$/In Composite with Durable Service Life for Magnetic Refrigeration. *Adv. Electron. Mater.*, 4(5):1700636, 2018.

[77] K Javed, S Gupta, V K Pecharsky, and R L Hadimani. Stability of magnetocaloric $La(Fe_xCo_ySi_{1-x-y})13$ in water and air. *AIP Adv.*, 9(3):35239, 2019.

[78] E Lovell, A M Pereira, A D Caplin, J Lyubina, and L F Cohen. Dynamics of the First-Order Metamagnetic Transition in Magnetocaloric $La(Fe,Si)_{13}$: Reducing Hysteresis. *Adv. Energy Mater.*, 5(6):1401639, 2015.

[79] J D Moore, K Morrison, K G Sandeman, M Katter, and L F Cohen. Reducing extrinsic hysteresis in first-order $La(Fe,Co,Si)_{13}$ magnetocaloric systems. *Appl. Phys. Lett.*, 95(25):252504, 2009.

[80] K P Skokov, D Yu. Karpenkov, M D Kuz'min, I A Radulov, T Gottschall, B Kaeswurm, M Fries, and O Gutfleisch. Heat exchangers made of polymer-bonded $La(Fe,Si)_{13}$. *J. Appl. Phys.*, 115(17):17A941, 2014.

[81] H Zhang, Y Sun, E Niu, F Hu, J Sun, and B Shen. Enhanced mechanical properties and large magnetocaloric effects in bonded $La(Fe, Si)_{13}$-based magnetic refrigeration materials. *Appl. Phys. Lett.*, 104(6):62407, 2014.

[82] H Zhang, Y Sun, Y Li, Y Wu, Y Long, J Shen, F Hu, J Sun, and B Shen. Mechanical properties and magnetocaloric effects in $La(Fe, Si)_{13}$ hydrides bonded with different epoxy resins. *J. Appl. Phys.*, 117(6):63902, 2015.

[83] R B Griffiths. Ferromagnets and Simple Fluids near the Critical Point: Some Thermodynamic Inequalities. *J. Chem. Phys.*, 43(6):1958–1968, 1965.

[84] H E Stanley. Scaling, universality, and renormalization: Three pillars of modern critical phenomena. *Rev. Mod. Phys.*, 71(2):S358–S366, 1999.

[85] A Arrott and J E Noakes. Approximate Equation of State For Nickel Near its Critical Temperature. *Phys. Rev. Lett.*, 19(14):786–789, 1967.

[86] H Hiroyoshi, A Hoshi, and Y Nakagawa. Arrott-Noakes plots near the Curie temperature of Fe_3Pt: Ordered and disordered alloys in high magnetic fields. *J. Appl. Phys.*, 53(3):2453–2455, 1982.

[87] V Franco, A Conde, and L F Kiss. Magnetocaloric response of FeCrB amorphous alloys: Predicting the magnetic entropy change from the Arrott–Noakes equation of state. *J. Appl. Phys.*, 104(3):33903, 2008.

[88] L Zhang, H Han, M Ge, H Du, C Jin, W Wei, J Fan, C Zhang, L Pi, and Y Zhang. Critical phenomenon of the near room temperature skyrmion material FeGe. *Sci. Rep.*, 6:22397, 2016.

[89] L J Ding, Y Zhong, S W Fan, and L Y Zhu. The magnetocaloric effect with critical behavior of a periodic Anderson-like organic polymer. *Phys. Chem. Chem. Phys.*, 18(1):510–518, 2016.

[90] V Franco, J S Blázquez, and A Conde. Field dependence of the magnetocaloric effect in materials with a second order phase transition: A master curve for the magnetic entropy change. *Appl. Phys. Lett.*, 89(22):222512, 2006.

[91] V Franco, J S Blázquez, J M Romero-Enrique, and A Conde. A universal curve for the magnetocaloric effect: an analysis based on scaling relations. *J. Phys. Condens. Matter*, 20(28):285207, 2008.

[92] V Franco and A Conde. Scaling laws for the magnetocaloric effect in second order phase transitions: From physics to applications for the characterization of materials. *Int. J. Refrig.*, 33(3):465–473, 2010.

[93] V Franco, A Conde, V K Pecharsky, and K A Gschneidner. Field dependence of the magnetocaloric effect in Gd and $(Er_{1-x}Dy_x)Al_2$: Does a universal curve exist? *EPL*, 79(4):47009, 2007.

[94] C M Bonilla, J Herrero-Albillos, F Bartolomé, L M García, M Parra-Borderías, and V Franco. Universal behavior for magnetic entropy change in magnetocaloric materials: An analysis on the nature of phase transitions. *Phys. Rev. B*, 81(22):224424, 2010.

[95] Ü Akıncı, Y Yüksel, and E Vatansever. Magnetocaloric properties of the spin-S ($S \geq 1$) Ising model on a honeycomb lattice. *Phys. Lett. A*, 382(45):3238–3243, 2018.

[96] S S Samatham and V Ganesan. Critical behavior, universal magnetocaloric, and magnetoresistance scaling of MnSi. *Phys. Rev. B*, 95(11):115118, 2017.

[97] Y Zhang, X Xu, Y Yang, L Hou, Z Ren, X Li, and G Wilde. Study of the magnetic phase transitions and magnetocaloric effect in Dy_2Cu_2In compound. *J. Alloys Compd.*, 667:130–133, 2016.

[98] C P Bean and D S Rodbell. Magnetic Disorder as a First-Order Phase Transformation. *Phys. Rev.*, 126(1):104–115, 1962.

[99] O Nashima, T Suzuki, K Kamishima, T Goto, and H Ido. Magnetic phase transition of $MnAs_{1-x}Sb_x$. *Phys. B Condens. Matter*, 237-238:159–161, 1997.

[100] P J von Ranke, N A de Oliveira, and S Gama. Understanding the influence of the first-order magnetic phase transition on the magnetocaloric effect: application to $Gd_5(Si_xGe_{1-x})_4$. *J. Magn. Magn. Mater.*, 277(1):78–83, 2004.

[101] M Oumezzine, J S Amaral, F J Mompean, M García-Hernández, and M Oumezzine. Structural, magnetic, magneto-transport properties and Bean–Rodbell model simulation of disorder effects in Cr3+ substituted $La_{0.67}Ba_{0.33}MnO_3$ nanocrystalline synthesized by modified Pechini method. *RSC Adv.*, 6(38):32193–32201, 2016.

[102] H N Bez, K K Nielsen, P Norby, A Smith, and C R H Bahl. Magneto-elastic coupling in La(Fe, Mn, Si)$_{13}H_y$ within the Bean-Rodbell model. *AIP Adv.*, 6(5):56217, 2016.

[103] K Deepak and R V Ramanujan. Near room temperature giant magnetocaloric effect in $(MnNiSi)_{1-x}(Fe_2Ge)_x$ alloys. *J. Alloys Compd.*, 743:494–505, 2018.

[104] B K Banerjee. On a generalised approach to first and second order magnetic transitions. *Phys. Lett.*, 12(1):16–17, 1964.

[105] S Bustingorry, F Pomiro, G Aurelio, and J Curiale. Second-order magnetic critical points at finite magnetic fields: Revisiting Arrott plots. *Phys. Rev. B*, 93(22):224429, 2016.

[106] K Morrison, A Dupas, Y Mudryk, V K Pecharsky, K A Gschneidner, A D Caplin, and L F Cohen. Identifying the critical point of the weakly first-order itinerant magnet $DyCo_2$ with complementary magnetization and calorimetric measurements. *Phys. Rev. B*, 87(13):134421, 2013.

[107] L M Moreno-Ramírez, C Romero-Muñiz, J Y Law, V Franco, A Conde, I A Radulov, F Maccari, K P Skokov, and O Gutfleisch. The role of Ni in modifying the order of the phase transition of $La(Fe,Ni,Si)_{13}$. *Acta Mater.*, 160:137–146, 2018.

[108] L Tocado, E Palacios, and R Burriel. Entropy determinations and magnetocaloric parameters in systems with first-order transitions: Study of MnAs. *J. Appl. Phys.*, 105(9):93918, 2009.

[109] A Carvalho, G Magnus, A A Coelho, P J von Ranke, and C S Alves. The isothermal variation of the entropy (ΔS_T) may be miscalculated from magnetization isotherms in some cases: MnAs and $Gd_5Ge_2Si_2$ compounds as examples. *J. Alloys Compd.*, 509(8):3452–3456, 2011.

[110] L Caron, Z Q Ou, T T Nguyen, D T Cam Thanh, O Tegus, and E Brück. On the determination of the magnetic entropy change in materials with first-order transitions. *J. Magn. Magn. Mater.*, 321(21):3559–3566, 2009.

[111] Quantum Design. Heat capacity option user's manual (Physical Property Measurement System).

[112] J C Lashley, M F Hundley, A Migliori, J L Sarrao, P G Pagliuso, T W Darling, M Jaime, J C Cooley, W L Hults, L Morales, D J Thoma, J L Smith, J Boerio-Goates, B F Woodfield, G R Stewart, R A Fisher, and N E Phillips. Critical examination of heat capacity measurements made on a Quantum Design physical property measurement system. *Cryogenics*, 43(6):369–378, 2003.

[113] H Suzuki, A Inaba, and C Meingast. Accurate heat capacity data at phase transitions from relaxation calorimetry. *Cryogenics*, 50(10):693–699, 2010.

[114] J M D Coey. *Magnetism and Magnetic Materials.* Cambridge University Press, 2010.

[115] C R H Bahl and K K Nielsen. The effect of demagnetization on the magnetocaloric properties of gadolinium. *J. Appl. Phys.*, 105(1):13916, 2009.

[116] R Caballero-Flores, V Franco, A Conde, and L F Kiss. Influence of the demagnetizing field on the determination of the magnetocaloric effect from magnetization curves. *J. Appl. Phys.*, 105(7):07A919, 2009.

[117] H Neves Bez, H Yibole, A Pathak, Y Mudryk, and V K Pecharsky. Best practices in evaluation of the magnetocaloric effect from bulk magnetization measurements. *J. Magn. Magn. Mater.*, 458:301–309, 2018.

[118] J M Borrego, C F Conde, A Conde, S Roth, H Grahl, A Ostwald, and J Eckert. Glass-forming ability and crystallization behavior of $Co_{62-x}Fe_xNb_6Zr_2B_{30}$ (x=0,16) amorphous alloys with large supercooled liquid region. *J. Appl. Phys.*, 92(11):6607–6611, 2002.

[119] I S Jeong and R M Walser. Magnetization distribution in nearly isotropic, ultra-soft magnetic CoB amorphous thin films. *IEEE Trans. Magn.*, 25(5):3366–3368, 1989.

[120] L M Moreno-Ramírez, J J Ipus, V Franco, J S Blázquez, and A Conde. Analysis of magnetocaloric effect of ball milled amorphous alloys: Demagnetizing factor and Curie temperature distribution. *J. Alloys Compd.*, 622, 2015.

[121] C Suryanarayana. Mechanical alloying and milling. *Prog. Mater. Sci.*, 46(1):1–184, 2001.

[122] L M Moreno, J S Blázquez, J J Ipus, and A Conde. Amorphization and evolution of magnetic properties during mechanical alloying of $Co_{62}Nb_6Zr_2B_{30}$: Dependence on starting boron microstructure. *J. Alloys Compd.*, 585:485–490, 2014.

[123] L M Moreno, J S Blázquez, J J Ipus, J M Borrego, V Franco, and A Conde. Magnetocaloric effect of $Co_{62}Nb_6Zr_2B_{30}$ amorphous alloys obtained by mechanical alloying or rapid quenching. *J. Appl. Phys.*, 115(17):17A302, 2014.

[124] V Franco, J S Blázquez, M Millán, J M Borrego, C F Conde, and A Conde. The magnetocaloric effect in soft magnetic amorphous alloys. *J. Appl. Phys.*, 101(9):09C503, 2007.

[125] C Romero-Muñiz, J J Ipus, J S Blázquez, V Franco, and A Conde. Influence of the demagnetizing factor on the magnetocaloric effect: Critical scaling and numerical simulations. *Appl. Phys. Lett.*, 104(25):252405, 2014.

[126] N G Bebenin, R I Zainullina, V V Ustinov, and Y M Mukovskii. Effect of inhomogeneity on magnetic, magnetocaloric, and magnetotransport properties of $La_{0.6}Pr_{0.1}Ca_{0.3}MnO_3$ single crystal. *J. Magn. Magn. Mater.*, 324(6):1112–1116, 2012.

[127] D M Liu, Z L Zhang, S L Zhou, Q Z Huang, X J Deng, M Yue, C X Liu, J X Zhang, and J W Lynn. A pathway to optimize the properties of magnetocaloric $Mn_{2-x}Fe_xP_{1-y}Ge_y$ for magnetic refrigeration. *J. Alloys Compd.*, 666:108–117, 2016.

[128] J S Amaral, P B Tavares, M S Reis, J P Araújo, T M Mendonça, V S Amaral, and J M Vieira. The effect of chemical distribution on the magnetocaloric effect: A case study in second-order phase transition manganites. *J. Non. Cryst. Solids*, 354(47):5301–5303, 2008.

[129] P Álvarez, P Gorria, V Franco, J Sánchez-Marcos, M J Pérez, J L Sánchez-Llamazares, I Puente-Orench, and J A Blanco. Nanocrystalline Nd_2Fe_{17} synthesized by high-energy ball milling: crystal structure, microstructure and magnetic properties. *J. Phys. Condens. Matter*, 22(21):216005, 2010.

[130] J S Blázquez, L M Moreno-Ramírez, J J Ipus, L F Kiss, D Kaptás, T Kemény, V Franco, and A Conde. Effect of α-Fe impurities on the field dependence of magnetocaloric response in $LaFe_{11.5}Si_{1.5}$. *J. Alloys Compd.*, 646:101–105, 2015.

[131] J S Blázquez, J J Ipus, L M Moreno-Ramírez, J M Álvarez-Gómez, D Sánchez-Jiménez, S Lozano-Pérez, V Franco, and A Conde. Ball milling as a way to produce magnetic and magnetocaloric materials: a review. *J. Mater. Sci.*, 52(20), 2017.

[132] H P J Wijn. *Landolt-Börnstein Neue serie: Magnetische Eigenschaften von Metallen*. Springer-Verlag, Berlin, 1991.

[133] M. W. Zemansky. *Heat and Thermodynamics*. McGraw-Hill, New York, 5 th ed. edition, 1968.

[134] L M Moreno-Ramírez, J S Blázquez, J Y Law, V Franco, and A Conde. Optimal temperature range for determining magnetocaloric magnitudes from heat capacity. *J. Phys. D. Appl. Phys.*, 49(49):495001, 2016.

[135] L M Moreno-Ramírez, V Franco, A Conde, H Neves Bez, Y Mudryk, and V K Pecharsky. Influence of the starting temperature of calorimetric measurements on the accuracy of determined magnetocaloric effect. *J. Magn. Magn. Mater.*, 457:64–69, 2018.

[136] L M Moreno-Ramírez, V Franco, and A Conde. Influence of low temperature truncated calorimetric data on the determination of the magnetocaloric effect of biphasic materials. *J. Magn. Magn. Mater.*, 479:236–239, 2019.

[137] H B Callen. *Thermodynamics and a introduction to termostatics*. John Wiley and Sons, New York, 2nd edition, 1985.

[138] V K Pecharsky, J O Moorman, and K A Gschneidner. A 3–350 K fast automatic small sample calorimeter. *Rev. Sci. Instrum.*, 68(11):4196–4207, 1997.

[139] A G Gamzatov, A M Aliev, A Ghotbi Varzaneh, P Kameli, I Abdolhosseini Sarsari, and S C Yu. Inverse-direct magnetocaloric effect crossover in $Ni_{47}Mn_{40}Sn_{12.5}Cu_{0.5}$ Heusler alloy in cyclic magnetic fields. *Appl. Phys. Lett.*, 113(17):172406, 2018.

[140] L M Moreno-Ramírez, A Delgado-Matarín, J Y Law, V Franco, and A Conde. The thermal and magnetic history dependence of

direct ΔT_{ad} measurements of $Ni_{49+x}Mn_{36-x}In_{15}$ Heusler compounds. *Submitted*, 2019.

[141] L Zhou, A Mehta, A Giri, K Cho, and Y Sohn. Martensitic transformation and mechanical properties of $Ni_{49+x}Mn_{36-x}In15$ (x=0, 0.5, 1.0, 1.5 and 2.0) alloys. *Mater. Sci. Eng. A*, 646:57–65, 2015.

[142] L M Moreno-Ramírez, J S Blázquez, V Franco, A Conde, M Marsilius, V Budinsky, and G Herzer. Magnetocaloric response of amorphous and nanocrystalline Cr-containing Vitroperm-type alloys. *J. Magn. Magn. Mater.*, 409:56–61, 2016.

[143] L M Moreno-Ramírez, V Franco, M Pękała, and A Conde. Influence of Noise on the Determination of Curie Temperature From Magnetocaloric Analysis. *IEEE Trans. Magn.*, 53(11):2502004, 2017.

[144] M. Sánchez-Pérez, L.M. Moreno-Ramírez, V. Franco, A. Conde, M. Marsilius, and G. Herzer. Influence of nanocrystallization on the magnetocaloric properties of Ni-based amorphous alloys: Determination of critical exponents in multiphase systems. *J. Alloys Compd.*, 686:717–722, 2016.

[145] J Y Law, V Franco, L M Moreno-Ramírez, A Conde, D Y Karpenkov, I Radulov, K P Skokov, and O Gutfleisch. A quantitative criterion for determining the order of magnetic phase transitions using the magnetocaloric effect. *Nat. Commun.*, 9(1):2680, 2018.

[146] K. Huang. *Statistical Mechanics*. John Wiley & Sons, 2nd edn edition, 1987.

[147] V Franco and A Conde. Magnetic refrigerants with continuous phase transitions: Amorphous and nanostructured materials. *Scr. Mater.*, 67(6):594–599, 2012.

[148] L Zhou, Y Tang, Y Chen, H Guo, W Pang, and X Zhao. Table-like magnetocaloric effect and large refrigerant capacity of composite magnetic refrigerants based on $LaFe_{11.6}Si_{1.4}H_y$ alloys. *J. Rare Earths*, 36(6):613–618, 2018.

[149] P Gorria, J L Sánchez-Llamazares, P Álvarez, M J Pérez, J Sánchez-Marcos, and J Blanco. Relative cooling power enhancement in magneto-caloric nanostructured Pr_2Fe_{17}. *J. Phys. D. Appl. Phys.*, 41(19):192003, 2008.

[150] J Y Law, L M Moreno-Ramírez, J S Blázquez, V Franco, and A Conde. Gd+GdZn biphasic magnetic composites synthesized in a single preparation step: Increasing refrigerant capacity without decreasing magnetic entropy change. *J. Alloys Compd.*, 675:244–247, 2016.

[151] R Bjørk, C R H Bahl, A Smith, and N Pryds. Optimization and improvement of Halbach cylinder design. *J. Appl. Phys.*, 104(1):13910, 2008.

[152] Casey W Miller, Dustin D Belyea, and Brian J Kirby. Magnetocaloric effect in nanoscale thin films and heterostructures. *J. Vac. Sci. Technol. A*, 32(4):40802, 2014.

[153] N M Dempsey, T G Woodcock, H Sepehri-Amin, Y Zhang, H Kennedy, D Givord, K Hono, and O Gutfleisch. High-coercivity Nd–Fe–B thick films without heavy rare earth additions. *Acta Mater.*, 61(13):4920–4927, 2013.

[154] O Akdogan, H Sepehri-Amin, N M Dempsey, T Ohkubo, K Hono, O Gutfleisch, T Schrefl, and D Givord. Preparation, Characterization, and Modeling of Ultrahigh Coercivity Sm–Co Thin Films. *Adv. Electron. Mater.*, 1(5):1500009, 2015.

[155] M Fiebig, T Lottermoser, D Meier, and M Trassin. The evolution of multiferroics. *Nat. Rev. Mater.*, 1:16046, 2016.

[156] D Doblas, L M Moreno-Ramírez, V Franco, A. Conde, A V Svalov, and G V Kurlyandskaya. Nanostructuring as a procedure to control the field dependence of the magnetocaloric effect. *Mater. Des.*, 114:214–219, 2017.

[157] A V Svalov, V O Vas'kovskiy, J M Barandiarán, K G Balymov, A N Sorokin, I Orue, A Larrañaga, N N Schegoleva, and G V Kurlyandskaya. Structure and Magnetic Properties of Gd/Ti Nanoscale Multilayers. In *Trends Magn.*, volume 168 of *Solid State Phenomena*, pages 281–284. Trans Tech Publications, 2011.

[158] M Farle, K Baberschke, U Stetter, A Aspelmeier, and F Gerhardter. Thickness-dependent Curie temperature of Gd(0001)/W(110) and its dependence on the growth conditions. *Phys. Rev. B*, 47(17):11571–11574, 1993.

[159] R E Camley. Surface spin reorientation in thin Gd films on Fe in an applied magnetic field. *Phys. Rev. B*, 35(7):3608–3611, 1987.

[160] X Chen, Y Chen, and Y Tang. The effect of different temperature annealing on phase relation of $LaFe_{11.5}Si_{1.5}$ and the magnetocaloric effects of $La_{0.8}Ce_{0.2}Fe_{11.5-x}Co_xSi_{1.5}$ alloys. *J. Magn. Magn. Mater.*, 323(24):3177–3183, 2011.

[161] P Gębara, J Marcin, and I Škorvánek. Effect of Partial Substitution of La by Ce on the Nature of Phase Transition in Magnetocaloric $La_{1-x}Ce_xFe_{11.2}Co_{0.7}Si_{1.1}$ Alloys. *J. Electron. Mater.*, 46(11):6518–6522, 2017.

[162] P Gębara and J Kovac. The influence of partial substitution of La by Dy on structure and thermomagnetic properties of the $LaFe_{11.0}Co_{0.7}Si_{1.3}$ alloy. *J. Magn. Magn. Mater.*, 454:298–303, 2018.

[163] R Bjørk, C R H Bahl, and M Katter. Magnetocaloric properties of $LaFe_{13-x-y}Co_xSi_y$ and commercial grade Gd. *J. Magn. Magn. Mater.*, 322(24):3882–3888, 2010.

[164] K Löwe, J Liu, K P Skokov, J D Moore, H Sepehri-Amin, K Hono, M Katter, and O Gutfleisch. The effect of the thermal decomposition reaction on the mechanical and magnetocaloric properties of $La(Fe,Si,Co)_{13}$. *Acta Mater.*, 60(10):4268–4276, 2012.

[165] S Sun, R Ye, and Y Long. Influence of the substitution of Ni for Fe on the microstructure evolution and magnetic phase transition in $La(Fe_{1-x}Ni_x)_{11.5}Si_{1.5}$ compounds. *Mater. Sci. Eng. B*, 178(1):60–64, 2013.

[166] M Krautz, K P Skokov, T Gottschall, C S Teixeira, A Waske, J Liu, L Schultz, and O Gutfleisch. Systematic investigation of Mn substituted $La(Fe,Si)_{13}$ alloys and their hydrides for room-temperature magnetocaloric application. *J. Alloys Compd.*, 598:27–32, 2014.

[167] X Chen, Y Chen, Y Tang, and D Xiao. The system study of 1:13 phase formation, the magnetic transition adjustment, and magnetocaloric property in $La(Fe,Co)_{13-x}Si_x$ alloys. *J. Magn. Magn. Mater.*, 368:155–168, 2014.

[168] P Gębara, P Pawlik, and M Hasiak. Alteration of negative lattice expansion of the $La(Fe,Si)_{13}$-type phase in $LaFe_{11.14-x}Co_{0.66}Ni_xSi_{1.2}$ alloys. *J. Magn. Magn. Mater.*, 422:61–65, 2017.

[169] Zsolt Gercsi. Magnetic coupling in transition-metal–doped $LaSiFe_{11.5}TM_{0.5}$(TM=Cr, Mn, Co and Ni). *EPL*, 110(4):47006, 2015.

[170] M Katter, V Zellmann, G W Reppel, and K Uestuener. Magnetocaloric Properties of $La(Fe,Co,Si)_{13}$ Bulk Material Prepared by Powder Metallurgy. *IEEE Trans. Magn.*, 44(11):3044–3047, 2008.

[171] S T Zong and Y Long. The influence of Cr and Ni on the character of magnetic phase transition in $LaFe_{11.52-x}M_xSi_{1.48}$ alloys. *AIP Adv.*, 8(4):48101, 2017.

[172] S Fujieda, A Fujita, and K Fukamichi. Large magnetocaloric effect in $La(Fe_xSi_{1-x})_{13}$ itinerant-electron metamagnetic compounds. *Appl. Phys. Lett.*, 81(7):1276–1278, 2002.

[173] O Gutfleisch, A Yan, and K.-H. Müller. Large magnetocaloric effect in melt-spun $LaFe_{13-x}Si_x$. *J. Appl. Phys.*, 97(10):10M305, 2005.

[174] J Liu, M Krautz, K P Skokov, T G Woodcock, and O Gutfleisch. Systematic study of the microstructure, entropy change and adiabatic temperature change in optimized La-Fe-Si alloys. *Acta Mater.*, 59(9):3602–3611, 2011.

[175] Brian H Toby. R factors in Rietveld analysis: How good is good enough? *Powder Diffr.*, 21(1):67–70, 2006.

[176] L M Moreno-Ramírez, C Romero-Muñiz, J Y Law, V Franco, A Conde, I A Radulov, F Maccari, K P Skokov, and O Gutfleisch. Tunable first order transition in $La(Fe,Cr,Si)_{13}$ compounds: retaining magnetocaloric response despite a magnetic moment reduction. *Submitted*, 2019.